THESIS FOR THE DEGREE OF DOCTOR OF PHILOSOPHY

Quantum acoustics with propagating phonons

Maria K. Ekström

Quantum Technology
Department of Microtechnology and Nanoscience (MC2)
Chalmers University of Technology
Göteborg, Sweden 2020

Quantum acoustics with propagating phonons

Maria K. Ekström

ISBN 978-91-7905-330-7

Doktorsavhandlingar vid Chalmers tekniska högskola
Ny serie nr 4797
ISSN 0346-718X

Quantum Technology
Department of Microtechnology and Nanoscience (MC2)
Chalmers University of Technology
SE-412 96 Göteborg, Sweden
Telephone: +46 (0)31-772 1000

Front cover, middle: Artistic illustration of an artificial atom emitting sound waves (not to scale). From the right, an artificial atom generates sound waves consisting of ripples on the surface of the substrate. The sound, known as surface acoustic waves (SAWs) are picked up by a "microphone" composed of interdigital transducer situated to the left. The sound consists of individual quantum particles, phonons; the weakest whisper physically possible. Credit: Philip Krantz, Krantz NanoArt
Front cover, corners: Scanning electron microscope images of part of two types of "microphones"; one IDT (interdigital transducer) emitting SAWs in two directions (top left corner) and one FEUDT (floating electrode unidirectional transducer) focusing SAWs in one direction (lower left corner) towards the artificial atom (lower right corner).

Printed by Chalmers digital print
Göteborg, Sweden 2020

Quantum acoustics with propagating phonons

MARIA K. EKSTRÖM

Quantum Technology
Department of Microtechnology and Nanoscience (MC2)
Chalmers University of Technology

Abstract

Surface acoustic waves (SAWs) are mechanical vibrations that propagate on the surface of solids while dissipating little power, consequently enabling them to propagate freely over long distances. The speed and wavelength of SAWs are reduced five orders of magnitude compared to when light is used as a carrier at gigahertz frequencies. The unique properties of SAWs combined with the possibility to let them interact with artificial atoms, discovered and shown for the very first time in the appended Paper I of this thesis, open up for exploration of new regimes of quantum physics. The appended Paper II is a book chapter providing an overview of many of the new areas of research, as well as going into depth of the method and significance of the results of the appended Paper I.

The essential interaction between artificial atoms and SAWs was further investigated by using Autler-Townes splitting to achieve fast control of the interactions. The appended Paper IV, shows a transmitted field extinction of 80 %, and provides proof of concept for a SAW router in the quantum regime. In addition, due to the artificial atom's highly frequency dependent coupling to SAWs, electromagnetically induced transparency (EIT) could be observed in the appended Paper V. Furthermore, the EIT region was distinguished from the Autler-Townes splitting region by a threshold in the applied power. The results produce parallel findings to quantum optics, but are perhaps best described as part of a different field, quantum acoustics.

Among the many possible areas of research emerging as an outcome of this work, a variety of potential quantum experiments would benefit greatly from a higher conversion efficiency between electric signals and SAWs. Due to this, focus was put on improving this conversion efficiency by studying superconducting unidirectional transducers (UDTs), making use of advances in classical SAW devices. The appended Paper III shows that 99.4 % of the acoustic power can be focused in a desired direction and that the conversion between electric signals and SAWs is greatly improved by using UDTs, thereby eliminating the largest source of loss of standard symmetric inter-digital transducers. There is, however, a trade-off between conversion efficiency and bandwidth. This finding allows tailoring of quantum experiments based on SAWs that may pave the way towards further investigating quantum sound.

Keywords: Surface acoustic wave, interdigital transducer, unidirectional transducer, quantum acoustics, superconducting circuits, artificial atom, qubit, phonon, phonon router, Electromagnetically Induced Transparency

List of appended papers

This thesis is a continuation of my licentiate thesis:

Towards measuring quantum sound
Maria K. Ekström, Licentiate thesis, Chalmers University of Technology, 2016

It is based on the work contained in the following papers:

I **Propagating phonons coupled to an artificial atom**
Martin V. Gustafsson, Thomas Aref, Anton Frisk Kockum, **Maria K. Ekström**, Göran Johansson and Per Delsing
Science **346**, 207 (2014)

II **Quantum Acoustics with Surface Acoustic Waves**
Thomas Aref, Per Delsing, **Maria K. Ekström**, Anton Frisk Kockum, Martin V. Gustafsson, Göran Johansson, Peter Leek, Einar Magnusson and Riccardo Manenti
In: *Superconducting Devices in Quantum Optics*,
edited by H. R. Hadfield and G. Johansson
(Springer International Publishing, Cham, 2016) pp. 217-244

III **Surface acoustic wave unidirectional transducer for quantum applications**
Maria K. Ekström, Thomas Aref, Johan Runeson, Johan Björck, Isac Boström and Per Delsing
Appl. Phys. Lett. **110**, 073105 (2017)

IV **Towards phonon routing: controlling propagating acoustic waves in the quantum regime**
Maria K. Ekström, Thomas Aref, Andreas Josefsson Ask, Gustav Andersson, Baladitya Suri, Haruki Sanada, Göran Johansson and Per Delsing
New J. Phys. **21**, 123013 (2019)

V **Electromagnetically induced transparency with a propagating mechanical mode**
Gustav Andersson, **Maria K. Ekström** and Per Delsing
(Accepted for publication in *Phys. Rev. Lett.*, arXiv:1912.00777)

Papers outside the scope of this thesis:

1. **Cavity-free vacuum-Rabi splitting in circuit quantum acoustodynamics**
Andreas Ask, **Maria K. Ekström**, Per Delsing, and Göran Johansson
Phys. Rev. A **99**, 013840 (2019)

Contents

Nomenclature

List of abbreviations

BAW	Bulk acoustic wave
COM	Coupling of modes, theory used to simulate the response of a FEUDT
CPB	Cooper Pair Box
CPW	Coplanar waveguide
DART	Distributed acoustic reflective transducer
EIT	Electromagnetically induced transparency
FEUDT	Floating electrode unidirectional transducer
FEUDT_i	Sample i, which is a delay line with two FEUDTs in either a Towards or an Away configuration.
IDT	Interdigital transducer
IDT_i	Sample i, which is a delay line with two IDTs
IVC	Inner vacuum chamber
LASER	Light Amplification by Stimulated Emission of Radiation
LC resonator	A resonator consisting of a capacitor and an inductor
MOSFET	Metal-oxide-semiconductor field-effect transistor
P-matrix	Three port scattering matrix, relating the voltage and current in the electric port and the incoming and outgoing waves in the two acoustic ports 1 and 2. In this thesis port 1 is defined to face into the delay line.
QDT	An IDT as a part of the qubit
QED	Quantum electrodynamics
qubit	Quantum-bit
S-matrix	Multi port complex scattering matrix, here we use three ports where the incoming and outgoing waves are related for the electric port 3 and the two acoustic ports 1 and 2. In this thesis port 1 is defined to face into the delay line.
SAW	Surface acoustic wave
SQUID	Superconducting Quantum Interference Device
TL	Transmission line

UDT	Unidirectional transducer

List of symbols

$1/Y_0$	Characteristic impedance
$1/Y_L$	Characteristic load impedance
α	Anharmonicity
α	COM transduction parameter per unit length used in Chapter 3.5.2
Δ	Superconducting gap
δ	Detuning from the wavenumber at center frequency
δ_{nm}	Kronecker delta
$\dot{\Phi}_n$	Time derivative of the flux at node n
ϵ_0	Permittivity in vacuum
ϵ_∞	Effective dielectric permittivity
γ_{bs}	Loss due to beam steering
γ_{diff}	Loss due to diffraction
γ_{tot}	Total estimated propagation loss (γ_{prop}) and loss due to conversion in the wrong direction (γ_{D})
γ_{ue}	Loss that cannot be explained by directivity (γ_{D}) nor propagation loss (γ_{prop})
γ_{vis}	Loss due to viscous damping
Γ_{ac}	Acoustic coupling of the qubit to SAWs
γ_{air}	Attenuation due to air loading
γ_{att}	Attenuation coefficient
γ_{D}	Loss due to conversion into the wrong acoustic port (directive loss)
Γ_{el}	Electrical coupling between the qubit and the electric gate
γ_{prop}	Estimated loss during propagation in a delay line, includes loss due to diffraction (γ_{diff}), beam steering (γ_{bs}) and viscous damping (γ_{vis})
Γ_{tot}	Total coupling of the qubit, includes both Γ_{el} and Γ_{ac}
Γ_ϕ	Pure dephasing
Γ_{ij}	Relaxation rate from the state i to state j
γ_{ij}	Decoherence rate from the state i to state j
κ	COM reflection parameter per unit length
λ	Wavelength
λ_0	Wavelength at the center frequency of a transducer set by the length of one unit cell

$\mathcal{F}[\rho_f](k)$	Fourier transform of the surface charge density when a voltage is applied to one electrode and all other electrodes are grounded
$\mathcal{L}$	Lagrangian describing the difference between kinetic and potential energy of a system
μ_0	Constant approximation of $E(\omega)$
ω	Angular frequency
Ω_p	Rabi frequency of the incoming probe field
ϕ	Phase difference between the wave functions in the superconductors separated by a weak link in Chapter 2
ϕ	Surface potential, where + denotes propagation to the right and − denotes propagation to the left
Φ_0	Superconducting magnetic flux quantum
Φ_{ext}	External magnetic flux applied through the SQUID loop
Φ_n	Flux at node n
Ψ	The Ginzburg-Landau complex order parameter describing the state of the quantum system
ρ	Density operator
A	An arbitrary operator
$A(\omega)$	Superposition of the response from multiple electrodes
$B(x)$	Slowly varying amplitude of left propagating waves
$b(x)$	Wave amplitude for left propagating waves
$B[\mu s]$	Time delay causing a loss of -3 dB due to beam steering
$B_a(\omega)$	Acoustic susceptance in the circuit model for an IDT
$B_{aq}(\omega)$	Acoustic susceptance of a qubit transducer
C	Total capacitance of a qubit
c	Speed of light in vacuum
$C(x)$	Slowly varying amplitude of right propagating waves
$c(x)$	Wave amplitude for right propagating waves
c_g	Unitless factor accounting for the geometry of the electrodes in a transducer
C_J	Capacitance of a Josephson junction
C_T	Capacitance of a transducer
C_l	COM capacitance per unit length
e	Elementary charge
$E(\omega)$	Response of each individual electrode in an interdigitated transducer

E_C	Charging energy of a transmon (qubit if it can be considered a two-level system)
E_C	Charging energy required to move an electron of a Cooper pair
E_J	Josephson energy a transmon (qubit if it can be considered a two-level system)
E_L	Inductive energy
E_L	Inductive energy
f_0	Center frequency of an interdigitated transducer
f_{QDT}	Acoustic resonance frequency of a qubit set by the length of the unit cell of its transducer
f_{10}	Electric fundamental resonance frequency of a transmon (qubit if it can be considered a two-level system)
$G_a(\omega)$	Acoustic conductance in the circuit model for an IDT
G_{a0}	Acoustic conductance at center frequency in the circuit model for an IDT
$G_{aq}(\omega)$	Acoustic conductance of a qubit transducer
H	The Hamiltonian representing the total energy of a system
h	Plank's constant
h_1	COM constant determined from boundary conditions
h_2	COM constant determined from boundary conditions
I	Current in an interdigitated transducer
I_C	Critical current, the maximum value of the supercurrent that can flow through the junction without resistance
I_n	Current at node n
k	Wavenumber
K^2	Electromechanical coupling coefficient
k_0	Wavenumber at center frequency of a transducer
k_B	Boltzmann's constant
K_1	COM parameter determined from boundary conditions
K_2	COM parameter determined from boundary conditions
L	Inductance in Chapter 2
L	Propagation distance, separation between two interdigitated transducers in a delay line
$L + N_p\lambda$	Propagation distance between the centers of two transducers in a delay line with length L
L_J	Nonlinear inductance of a SQUID

N_{in}	Number of phonons converted per second from electrical power by a transducer
N_p	Number of unit cells of an interdigitated transducer
n_t	Transit number
P_{gate}	Electric power sent to qubit via gate line
P_{in}	Incoming power
Q_n	Charge at node n
r	Reflection response of a delay line including multiple transits
R_N	Normal resistance of the two Josephson Junctions (weak barriers) in the SQUID
s	Imaginary eigenvalues (per unit length) of COM differential equation
S_{41}	Loss during the acoustic reflection
S_{43}	Loss during the conversion from electric signals to SAWs
S_{q11}	Scattering element for acoustic reflection of a qubit
S_{q12}	Scattering element for acoustic transmission of a qubit
S_{q31}	Acoustic scattering element for emission from an electrically excited qubit
t	Transmission through a delay line including multiple transits
V	Applied voltage
v_0	SAW speed on a metal free surface
v_m	SAW speed when the surface is covered by a metal sheet
V_n	Voltage at node n
W	Electrode overlap defining the SAW beam width
x_{RC}	Effective center of reflection for one unit cell in a transducer
x_{TC}	Effective center of transduction for one unit cell in a transducer
x_n	Position of electrode n
Y_{IDT}	Total admittance of an IDT in the circuit model
Y_{Q}	Total admittance of a qubit in the combined semi-classical and circuit model
Z_0	Characteristic impedance

Chapter 1

Introduction

Every day sound is used as a communication tool. People can hear your voice because the pressure in your lungs vibrates your vocal cords, and this creates sound. Sound propagates in air as vibrations of pressure and density, quantities that oscillate in both time and space. The science of sound is called acoustics and sound propagates as acoustic waves through medium such as gas, liquid or solid.

Although the word acoustic is derived from the Greek word *akouein* with the meaning "to hear" [1], humans can only hear acoustic waves that have frequencies in the range between 20 Hz and 20 kHz. This is a very small part of the acoustic spectrum, which also includes ultrasound (sound at frequencies above human hearing) and infrasound (sound at frequencies below human hearing). In this thesis we focus on a small part of the ultrasound spectrum; acoustics at gigahertz frequencies and we use acoustics to communicate in the quantum regime by combining two fields of science; acoustics and quantum optics. The combined fields might be better described as a different field, quantum acoustics, where we study how acoustic waves interact with artificial atoms and in many ways mimic quantum optics by the usage of superconducting circuits and where we combine quantum theory with acoustic theory.

1.1 Acoustics - a very brief historic background

Acoustics has been studied for several millennia. Already in ancient Greece, in 6th century BC, acoustics was studied with the incentive to understand music. Allegedly, Aristotle described sound as compression and rarefactions of air in the 4th century BC, and in Rome, around 20 BC, acoustics was used to build theaters with good acoustic properties [1]. Since the scientific revolution started in the 16th century, the understanding of acoustics, its mathematical description and possible applications have advanced rapidly. One of the most famous acoustic inventions is Bell's *electric speech machine* (the telephone) from the 19th century, which formed the 20th century's society.

Another discovery of the 19th century, which is of great importance for this thesis, is Rayleigh's prediction and description of the first type of surface acoustic wave (SAW) [2, 3]. An acoustic wave that travels near the surface of an elastic solid, named Rayleigh wave. This type of wave can be observed at large scales in for instance earthquakes, where they cause a lot of destruction because they can be both large and propagate far due to their low propagation loss. Rayleigh waves can also be observed at small scales where they are used for, for instance, SAW-filters and sensors [2, 3]. However, the practical use

of SAWs relied on later discoveries such as the piezoelectric effect and the interdigital transducer.

The piezoelectric effect was discovered by Jacques and Pierre Curie in the early 20th century [1]. They found that applying an electric field over plates of certain natural crystals, such as quartz, changed the thickness of the crystal. Today, quartz crystals are widely used for regulating oscillator frequencies [3].

From the discovery of the piezoelectric effect, the first transducer emerged, which was used to generate acoustic waves in the sea in the ultrasound frequency range [3]. The driving force was to use these transducers for sound navigation and ranging (sonar) in submarines to detect mines during and after World War I [1]. Sonar is still used for military applications, but also to study the ocean and marine life, and a similar type of ultrasonic imaging is used for medicine diagnostics, for instance, to observe features in organs or to monitor real-time movements of heart valves.

During the 20th century several sub-disciplines to acoustics developed such as underwater acoustics and bioacoustics (including medical imaging), both mentioned above. Advances were also made within arts (music, communication and psychology), earth science (seismic waves and sound in the atmosphere), engineering (architecture, electrical, chemical and mechanical acoustics such as shock, vibration and noise) and fundamental (physics) acoustics.

Although the field of acoustics, its applications and several sub-disciplines continued evolving rapidly during the 20th century, it was not until the late part of that century that SAWs could be generated and detected efficiently. It was a key starting point when the interdigital transducer (IDT) was introduced by White and Voltmer in 1965 [4]. After this, many different designs followed and since they can be incorporated in electric circuits, they are used in a diversity of applications [3]. The possibility to design an IDT originates from the advances in radio frequency and microwave engineering, which developed during the wireless and electronics technology revolution driven by the invention of the MOSFET (metal-oxide-semiconductor field-effect transistor) using semiconductor technology. The MOSFET was the first transistor that could be made compact, miniaturized and mass-produced and it is the basis of modern electronics [5]. It enabled for scaling down computers from taking up an entire room to exist on small IC chip and is part of the digital communication technology. The scalability of the MOSFET lead microwave engineering to nanoelectronics. These advances in engineering are used in various fields such as acoustics, quantum optics and quantum acoustics, and provide the essence of the fabrication techniques used to build the devices in this thesis (see Chapter 4).

1.2 Quantum optics - a very brief historic background

In the field of quantum optics [6], physical properties are studied by letting light (i.e. electromagnetic waves) interact with matter in the quantum regime. This means that their physical properties need to be described by quantum mechanics. In contrast to classical mechanics where entities exist in a specific place at a specific time, entities in

quantum mechanics may exist in several places with different probabilities; they have a certain probability of being at a certain point and other probabilities of being at other points. In addition, many quantities are restricted to discrete values (quantization) and behave as both particles and waves where the accuracy of predicting a value of a quantity is limited by the uncertainty principle. By approximating quantum mechanics, many theories in classical physics can be derived.

Light has been studied since ancient times [7], for instance by using mirrors and lenses, and during the 17th and 18th century light was discussed to be of either particle or wave nature in classical physics. A famous experiment that was thought to prove the wave nature of light is the double-slit experiment by Young performed in the beginning of the 19th century. However, this experiment actually demonstrates the principle of wave-particle duality. Wave-particle duality means that light is neither only a particle nor only a wave, but have certain properties of both. In Young's experiment, a coherent light source is aimed towards a plate with two parallel slits and the light passing the slits is observed on a screen behind it. The light passing the two slits interfere and produces bright and dark regions on the screen, which is due to the wave nature of light and would not appear if light would simply be particles. On the other hand, light is absorbed at the screen at discrete points, featuring the particle nature of light, and the density of the interference pattern represents the number of particles hitting that point on the screen.

Later experiments show that if one detects what slit the particle passes through, the interference pattern is not formed. This is an example of the concept of wave-particle duality. It states that all quantum objects (including electrons and particles with larger mass) exhibit both wave and particle nature, but depending on how it is measured it shows either wave or particle character.

The discussion about light as particles or waves continued into the beginning of the 20th century. Max Planck studied patterns of black body radiation and described that the energy was radiated and absorbed in discrete energy packages ("quanta"). Albert Einstein further developed this idea with the photoelectric effect, in which certain materials eject electrons when illuminated with light of particular wavelengths. In this way light could be described as a particle (later known as a photon), with a discrete amount of energy that depends on the frequency of the wave nature of the light. Niels Bohr showed that their description of quantization of light corresponded to his theory of quantized energy levels of atoms, which Einstein expanded on to explain the absorption and emission of energy by atoms [7].

In this framework a physical property, such as the electromagnetic field or the properties of an atom, can be quantized and then they can only take certain discrete values. For instance, an electron in an atom can only exist at certain energy levels. When the atom interacts with light, it can get excited, *i.e.* an electron in the atom moves from one energy level to a higher one. After a while, the electron relaxes back to the lower energy level and the atom emits a single quantum, later known as a photon in the case of light and a phonon in the case of sound.

During the years 1924-1926, central parts of the theory of quantum mechanics were established. De Broglie postulated that all matter has wave properties and Heisenberg,

Schrödinger and Dirac developed the theoretical foundations of quantum mechanics that is still used today [7]. During this time, quantum optics also started concerning the quantum nature of light in addition to the more commonly studied light interacting with matter. These two branches within quantum optics differ concerning what is described as quantized. Previously light interacting with matter was solely described semi-classically, where the light field was considered classical and the matter was quantized. To describe quantization of light, or more generally electromagnetic fields, quantum electrodynamics (QED) is required, which was developed during this time.

Electromagnetic fields also include light that we cannot see, for instance radio frequency waves and microwaves. The advances in radio frequency and microwave engineering have benefited several other research fields, as mentioned in the previous chapter, and it has also enabled for combining different types of systems. Microwaves can be generated using semiconductor electronics and when this is done to study quantized electromagnetic fields in electronic circuits; it is called circuit-QED [8, 9]. Circuit-QED is of special interest for this thesis, where we use superconducting circuits to study quantum physics using acoustic waves.

At the end of the 1960s, it was possible to let atoms interact with electromagnetic fields confined in resonators and put atoms close to mirrors [7], and thus changing the interaction strength dramatically [10–12]. This was later referred to as cavity quantum electrodynamics (cavity QED) [13–15], in which atoms (or other quantum systems such as photons and ions) can be confined in optical and microwave cavities [16] and let them interact with single modes of a confined electromagnetic field. This interaction has reversible transition dynamics (Jaynes-Cummings model [17]) where the atom can exchange excitations with the field coherently until the coherence is lost. Using cavity-QED, strong coupling between the atom and the field could be achieved in both the optical [18, 19] and the microwave domain [20].

Many advances in the optical domain has been performed using a LASER (Light Amplification by Stimulated Emission of Radiation). The LASER is a classical device, introduced and demonstrated around the 1960s [21], which emits coherent light. This allows for a diversity of quantum experiments such as studying self-induced transparency, resonant interactions and the dynamics of single atoms interacting with both propagating light and light in cavities [7]. LASERs are also used for laser cooling [22, 23], control of individual quantum systems, buildup of interference at the single photon level, harmonic generation and parametric down-conversion [24, 25]. In addition to the many uses in quantum optics, LASERs are used in applications such as lithography (used as part of the device fabrication, see Chapter 4), laser pointers, fiber-optics, laser surgery and much more.

The advances in quantum optics combined with information processing, are basic concepts for quantum cryptography and quantum computation. Instead of classical bits (0 or 1), a quantum computer is based on quantum mechanical two-level systems (qubits). A qubit can be built by using a quantum system such that only two energy levels are used and the other energy levels can be disregarded. Unlike classical bits, each qubit can exist in coherent superpositions of 0 and 1. By making arbitrary operations on a single qubit (single qubit gates) or by coupling two different qubits (two qubit gates) controllably,

universal quantum computing can be made. Such computations are performed using unitary transformations acting on all states of superposition simultaneously. This enables for a high degree of parallelism that can increase the computational speed exponentially.

The possibility to transfer a quantum superposition to another type of quantum system was shown for a trapped ion, where the quantum superposition of its electronic states was transferred to a quantum superposition of vibrational modes of the trap [26]. If another ion shares these vibrational modes, the superposition can be transferred to it [27] and hence the quantum superposition can be transferred from one ion to another. However, the quantum state changes when it is measured directly. An example of this can be found in the double slit experiment, where the interference pattern is lacking due to the photon detection at each slit. In 2012, Serge Haroche and David Wineland were awarded The Nobel Prize in Physics for enabling measurements and manipulation of single ions [28, 29] and photon states [28, 30, 31] without destroying these quantum systems.

As part of this type of research, there is also quantum entanglement, quantum teleportation and quantum encryption. A quantum mechanical system is entangled if the quantum state of each particle or group of particles in the system cannot be described independently of the states of the other constituents in the system. Quantum entanglement can occur over large distances and is used for quantum teleportation. In quantum teleportation, quantum information such as the state of an atom or photon can be transmitted from one location to another, which have shared quantum entanglement. The information can be shared if coherence is not lost. A practical use of quantum teleportation is secure communication with quantum encryption, in which it is impossible to detect the quantum information without changing the quantum system.

In addition to the applications, the increased control in isolating, manipulating and measuring individual quantum systems has given more possibilities to studying fundamental quantum physics phenomena. In parallel with the many possibilities with natural atoms, ions and photons there are also other systems that are used for studying quantum electrodynamics and using them for applications such as quantum computation. These are systems such as quantum dots [32], nitrogen-vacancy centers in diamond [33], rare-earth ions in crystals [34] and the most important ones for this thesis, superconducting circuits (see Chapter 2).

In superconducting circuits, the non-linearity is obtained using superconducting artificial atoms that come in various forms with different specifications. For instance, there is the Cooper-pair box [35, 36], the transmon [37], the flux qubit [38, 39] and the phase qubit [40] among the many types of superconducting artificial atoms. Since superconducting circuits can be designed and fabricated with lithography processes to suit a certain experiment, they make it possible to study some unique physical phenomena and also combine them with different types of quantum systems such as acoustic waves used in this thesis and described in the following section.

1.3 Quantum acoustics

In quantum acoustics, the interaction between matter and sound (or acoustic waves) is studied in the quantum regime. In contrast to classical acoustics and similar to quantum optics, physical properties in quantum acoustics require a quantum mechanical description. A quantum of sound is the minimum amount of mechanical vibration involved in an interaction and it is called a phonon, which is an analogue to the photon in quantum optics.

Typical mechanical systems in the quantum regime consist of micro-scale mechanical beams and drums that are cooled down to such low temperatures that the thermal excitations of the mechanical vibrations are frozen out [41–44]. Mechanically oscillating systems can interact with electromagnetic waves in both the optical [45, 46] and the microwave domain [46–48], and are studied in the field of optomechanics. The coupling between these mechanical systems and electromagnetic waves is linear, but they can be designed to interact with superconducting artificial atoms [42] and in this way it has been possible create non-classical states [43]. It has also been shown that the same superconducting artificial atom can be coupled to both an electromagnetic microwave cavity and a micromechanical resonator [44].

In addition to coupling to superconducting artificial atoms, the versatility of mechanical oscillators enables for interaction with different types of quantum systems, such as nitrogen-vacancy defect centers in diamond [49–51] and quantum-dots [52]. Moreover, mechanical oscillators are quantized in vibrational states and motional entanglement has been shown between the vibrational states of two trapped ions separated by 0.24 mm [53], of two diamonds spatially separated by 15 mm at room temperature [54], between two massive micromechanical oscillators separated 600 μm [55] and between a macroscopic mechanical oscillator and a propagating electric signal [56]. The possibility to entangle a quantum state has also been demonstrated in a system using two nanomechanical oscillators on two different chips separated by 20 cm [57].

By scaling these types of systems, it might be possible to transfer quantum information over large distances in quantum networks, which in turn could be integrated with optomechanical devices to transfer quantum information between the optical and the microwave domain and be part of a future quantum internet [57,58]. Using the possibility to transfer quantum information between different types of systems, the benefits from each system can be harvested while opting the drawbacks. Combining different quantum systems requires the coupling between them to be sufficiently strong to not lose coherence. An example where such strong coupling has been achieved is in optomechanical crystals, which are artificially made cavity structures for both optical photons and phonons [59].

The systems mentioned above are bound to the eigenmodes of certain structures, but there are also propagating mechanical vibrations that can be used in the field of quantum acoustics. For instance, SAWs, which propagate on the surface of solids with low dissipation. Such waves are widely used in classical applications (see Section 1.1), but they have also proven to be useful for cell manipulation [60, 61] and rapid mixing of very small amounts of fluids in life science [62, 63], as liquid [64] and gas sensors [65] as

well as for studying fundamental quantum effects with possibilities for future quantum applications. An overview of the present state of research using SAWs is presented in Ref. [66], which maps interdisciplinary research using a range of devices from nano- up to macroscopic scale.

Classical SAWs have been proposed to transport quantum information by being carriers of quantum particles in the form of electrons and holes in semiconductors [67], by manipulating and carry different types of excitations [68–70] and for charge carrier modulation in graphene [71, 72]. In semiconductor systems, SAWs have been used for absorption in double quantum dots [73] and phonon assisted tunneling [74]. Furthermore, SAWs in semiconductor systems have been used to transport single electrons on demand several times between two quantum dots separated by 3-4 μm [75, 76], to transport coherent spins though quantum dots [77] and to transport spin information between two quantum dots separated by 4 μm [78]. SAWs have also been used to carry single electrons to regions with holes to form excitations that decay into streams of single photons [79]. These types of systems provide possibilities to manipulate quantum information in flight due to the slow speed of the SAWs, transport information over large distances due to the low dissipation and transfer information between different types of quantum systems (e.g. electrons and photons).

In contrast to systems where classical SAWs are used to carry quantum particles, the quantum nature of propagating SAWs can be studied using much lower powers and by letting them interact with superconducting artificial atoms. That is the quantum mechanical system described and demonstrated in this thesis, with the ultimate goal of measuring and controlling quantum sound.

The interaction between SAWs and superconducting artificial atoms was experimentally shown for the first time in the appended Paper I in 2014. This work shows that propagating SAWs can interact in the quantum regime using superconducting circuits.

Later experiments demonstrated that such artificial atoms can also be placed inside SAW resonators [80–85] (initial work [86, 87] covered in the appended Paper II), and this confine the acoustic modes similar to the previously mentioned mechanical systems. There are also resonators where bulk acoustic waves (BAWs) are used instead of SAWs. In the BAW system, the artificial atom was placed on sapphire, a commonly used substrate in quantum optics, with only a thin layer of piezoelectric material under parts of the artificial atom [88]. With clever engineering, it should be possible to implement a similar solution in both SAW resonator and propagating SAW systems. Nonetheless, advances in quantum control, for instance superposition of states, have been showed using both a SAW resonator [84] and a BAW resonator [88]. SAW resonators have also been demonstrated to interact with spins in nitrogen-vacancy defect centers [89], and SAWs can be combined with optomechanical resonators to drive coherent oscillations [90, 91].

The advances in quantum acoustics and quantum optics have opened up new possibilities in a joint SAW and quantum research field. An advantage using SAWs and BAWs is that well-established methods from quantum optics can be used together with the unique properties of acoustic waves. SAWs' five order of magnitude slower speed than light makes their wavelength at microwave frequencies comparable to the wavelengths of

optical light. This combined with the fact that many of the piezoelectric materials used for SAWs are also used in optics, raises the potential to connect microwave circuit QED with optical wavelength systems using SAW [92]. Building such hybrid systems to utilize the benefits and avoid the drawbacks present in different quantum research fields is of great interest [93, 94] and a universal theoretical platform has been developed to link a wide range of artificial atoms [95].

There are many possibilities with artificial atoms, and they can even reach regimes that are not possible with natural atoms. An example of this is the superconducting artificial atom in the appended Paper I, which is twenty times larger than the wavelength of the field it interacts with and could easily have been made larger. Such as system cannot be treated as a point-like source, unlike known cases of both artificial and natural atoms interacting with light. The large artificial atom couples to SAWs in many points separated wavelengths apart and has a frequency-dependent coupling due to interference effects caused by the many coupling points [96] (summarized in the appended Paper II). The work in the appended Paper I and in Ref. [96] has led to both theoretical predictions [97, 98] and experimental demonstrations of giant atoms [99], which are hard to demonstrate in other types of architectures.

There are also experiments where the slow speed of the propagating SAWs can be beneficial, for instance in in-flight manipulation of propagating carriers of quantum information. A first demonstration of time control of the scattering properties SAWs interacting with an artificial atom can be found in the appended Paper IV where the artificial atom is used as a router of propagating SAWs. In this experiment, a strong electromagnetic drive was used to change the energy levels of the artificial atom such that its interaction with the propagating SAWs was manipulated. For a weaker drive, the same device could be used to demonstrate Electromagnetically Induced Transparency in the acoustic field and distinguish it from Autler-Townes splitting by finding the threshold between these two regimes, which is shown in the appended Paper V.

Although there are many physical phenomena that are easier to study with superconducting artificial atoms than with natural atoms, there are also experiments that are more difficult to perform. One example is the detection of single propagating photons or phonons. In quantum optics, radiation can be characterized by the correlation of emitted photons in time using single photon detectors [100, 101]. These do not exist commercially for microwave photons since microwaves have several orders of magnitude lower energy. Instead, the temporal correlation is made from measurements of the amplitude of the field [102–106]. To conduct a similar experiment with propagating SAW phonons, a more efficient conversion between electric microwave signals and SAWs would be beneficial.

The improvement of this conversion has been studied extensively in classical SAW devices ever since the generation and detection of them was possible with the interdigital transducer (IDT) [107] on piezoelectric materials. Different types of materials, origins of losses and transducer types have been studied and characterized [2, 3, 108–110]. The transducers are engineered in several ways to suit various application; among those are the unidirectional transducers (UDTs) [3, 111]. UDTs have lower losses than IDTs because they can focus the SAWs in one direction rather than emitting them symmetrically in both directions, as happens in IDTs. Both UDTs and other types of transducers have

been investigated for gigahertz frequencies [112], following the increasing frequencies used for telecommunications, and some experiments have utilized higher harmonics [113]. Although, it has been shown that the loss of the transducers reduces dramatically when they are superconducting [114], most of the studies with SAWs have been done at room temperature. Superconducting UDTs and IDTs are studied and compared in the appended Paper III and [115] to improve the conversion efficiency between electric microwave signals and SAWs in the quantum regime.

By increasing the electric/SAW conversion, the coupling between the artificial atom and SAWs is also increased. For such systems, the artificial atom no longer acts as an antenna emitting SAWs, which one would expect, but as its own cavity [116]. In such a system, an excitation can be emitted and absorbed several times before it leaves the artificial atom. This further shows an interesting regime that can be reached in the field of quantum acoustics, where both experimental and theoretical efforts strive to investigate fundamental quantum phenomena as well as possible quantum applications using acoustic and hybrid systems. The combined efforts in a diversity of fields have already made several advances and the work described in this thesis is part of this effort.

1.4 Outline of the thesis

This chapter has aimed to give a very brief overview of acoustics and quantum optics, and describe some of the advances made in quantum acoustics. The introduction will be followed by two theory chapters; Chapter 2 about quantum optics focusing on superconductivity, quantization of electric circuits and artificial atoms and Chapter 3 about acoustics focusing on surface acoustic waves, their generation and detection using superconducting circuits and their interaction with superconducting artificial atoms.

The fabrication and measurement of the devices used in the appended papers, is covered in Chapter 4 and the results are introduced in Chapter 5. This is followed by a summary and discussion of the thesis and the appended papers together with future possibilities for experiments with propagating SAW phonons in Chapter 6.

Chapter 2

Superconductivity

Certain metals become superconducting when cooled down below certain temperatures [117]. In the superconducting state the electrical resistance is zero, permitting a current to flow without dissipation, and magnetic fields are expelled from the interior of the material. This is known as the Meissner effect.

In a superconductor the electrons near the Fermi surface are paired into Cooper pairs [118], generally due to weak attractive interaction mediated by the vibrating lattice. The Cooper pairs have bosonic properties, instead of fermionic as single electrons have, and form a condensate. In BCS theory, superconductivity is a macroscopic effect of this condensation. Breaking up a pair into single electrons costs energy and changes the energy of the entire condensate. The result is an energy gap between the ground state and the lowest excited state of the superconductor. At zero temperature all electrons in the superconductor are paired, but at finite temperature some electrons are not paired.

2.1 Superconducting circuit quantization

Superconductors can be used in electric circuits for quantum experiments. These circuits contain a huge number of atoms, but at low enough temperatures their low energy performance can exhibit quantum behavior. A quantum mechanical system is described by the time dependent Schrödinger equation

$$H|\Psi(t)\rangle = i\hbar\frac{\partial}{\partial t}|\Psi(t)\rangle, \tag{2.1}$$

where H is the Hamiltonian representing the total energy of the system, $|\Psi(t)\rangle$ is the state vector of the quantum system at time t and $\hbar = h/2\pi$, h being Planck's constant.

A property of the quantum mechanical system, for instance momentum or position, is represented by an operator A. By applying the operator to the state vector of the system, the property represented by the operator can be obtained. In the Schrödinger picture operators are time-independent while the state vectors $|\Psi(t)\rangle$ are time-dependent and obey the Schrödinger equation in Eq. (2.1). However, the time evolution of a quantum system can be described in both the Schrödinger picture and the Heisenberg picture [119]. In the Heisenberg picture the operators are instead time-dependent and obey the Heisenberg equation

$$i\hbar\partial_t A(t) = [A, H] = AH - HA, \tag{2.2}$$

while the state vectors $|\Psi\rangle$ are time-independent. Both these pictures equivalently describes the time evolution of pure states.

If the system is a statistical ensemble of states $|\Psi_i\rangle$ with a probability w_i for the system to be in that state, we can introduce a density operator $\rho = \sum_i w_i |\Psi_i\rangle\langle\Psi_i|$ to describe the system. The time evolution of ρ is given by the Liouville-von Neumann equation

$$i\hbar\partial_t\rho = [H, \rho]\,, \tag{2.3}$$

which is equivalent to Eq. (2.1) for a pure state [119]. Given ρ, the expectation value of system operators and their time evolution can be calculated from $\langle A\rangle = Tr(A\rho)$ and $\partial_t\langle A\rangle = Tr(A\partial_t\rho)$, respectively. Eq. (2.1), (2.2) and (2.3) are valid for closed systems, and can be used as good approximations for systems where the influence of the surroundings are negligible.

In order to understand the dynamics of the system, in either of these pictures, the Hamiltonian should be determined. A systematic way is to go from a classical description of an electric circuit to quantum description by quantizing the circuit using the lumped element approximation. We will start by describing the approximation steps, then quantize a classical linear LC resonant circuit and finally describe nonlinear elements necessary for building superconducting artificial atoms, using the same steps in the approximation.

The first step in this approximation is to choose generalized coordinates. Generalized coordinates are an independent set of variables that can be obtained by identifying the nodes of the circuit and assigning a coordinate to each node. Since we are mostly interested in describing circuits containing nonlinear elements, it turns out that choosing flux nodes

$$\Phi_n(t) = \int_{-\infty}^{t} V_n(t')dt' \tag{2.4}$$

as generalized coordinates is convenient. Here V_n is the voltage at node n, which also is the branch voltage across the element if it is connected to ground.

The second step is to write down the Lagrangian $\mathcal{L}$, which is equal to the difference between the kinetic energy and the potential energy of the circuit. Using the node fluxes as generalized coordinates the Hamiltonian becomes

$$H = \sum_n \frac{\partial\mathcal{L}}{\partial\dot{\Phi}_n}\dot{\Phi}_n - \mathcal{L}, \tag{2.5}$$

where $\dot{\Phi}_n$ is the time derivative of the flux at node n and $\frac{\partial\mathcal{L}}{\partial\dot{\Phi}_n}$ are the generalized momenta equal to the node charges Q_n. The node charges

$$Q_n(t) = \int_{-\infty}^{t} I_n(t')dt', \tag{2.6}$$

with I_n being the current going into node n.

The third step is the step where we go from the classical to a quantum mechanical description. In this step the generalized coordinates and momenta are promoted to operators which obey the canonical commutation relation

$$\left[\Phi_n, \frac{\partial\mathcal{L}}{\partial\dot{\Phi}_n}\right] = i\hbar\delta_{nm}. \tag{2.7}$$

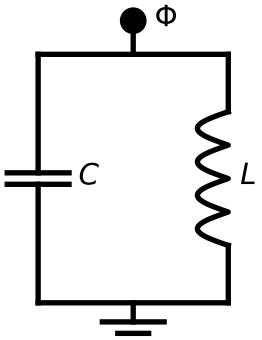

Figure 2.1: Circuit diagram of an LC resonator, with a capacitance C and an inductor L. The flux node is marked with Φ.

Here δ_{nm} is the Kronecker delta.Using this recipe, we can quantize any electrical circuit.

2.1.1 LC resonator

The LC resonator consists of a capacitor and an inductor and its circuit diagram is shown in Figure 2.1. The capacitor has two conductors separated by an insulator and it stores energy in the electric field between the two conductors when a voltage is applied. The energy of a capacitor

$$E_C = \frac{CV^2}{2} = \frac{C\dot{\Phi}^2}{2}, \tag{2.8}$$

where $\Phi = \Phi_1 - \Phi_2$.

The inductor is a coil storing energy in the magnetic field while a current flows through it. The voltage drop over an inductor $V = L\dot{I}$, where $\dot{I}$ is the time derivative of the current and the energy of an inductor is

$$E_L = \frac{LI^2}{2} = \frac{L}{2}\left(\int \frac{V(t)dt}{L}\right)^2 = \frac{\Phi^2}{2L}. \tag{2.9}$$

In the Lagrangian, terms with $\dot{\Phi}$ represents kinetic energy and terms with Φ represents potential energy. Since the Lagrangian is the difference between the kinetic and potential energy, the Lagrangian for the capacitor and the inductor become

$$\mathcal{L}_C = \frac{C\dot{\Phi}^2}{2} \tag{2.10}$$

$$\mathcal{L}_L = -\frac{\Phi^2}{2L}. \tag{2.11}$$

In the LC resonator the energy oscillates between electric energy in the capacitor and magnetic energy in the inductor and hence the Lagrangian for the LC resonator is

$$\mathcal{L}_{LC} = \frac{C\dot{\Phi}^2}{2} - \frac{\Phi^2}{2L}. \tag{2.12}$$

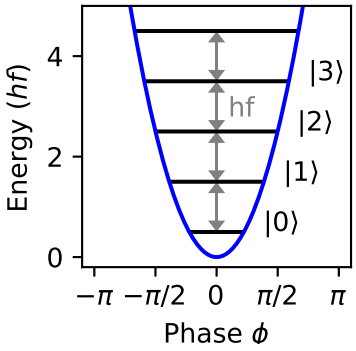

Figure 2.2: The energy spectrum of a quatum harmonic oscillator is discrete and the shape of the potential is quadratic (blue line). The energy levels (black lines) are equidistantly separated with hf (gray arrows).

From the Lagrangian and using Eq. (2.5), we derive the Hamiltonian

$$H_{LC} = C\dot{\Phi}^2 - \left(\frac{C\dot{\Phi}^2}{2} - \frac{\Phi^2}{2L}\right) = \frac{C\dot{\Phi}^2}{2} + \frac{\Phi^2}{2L} = \frac{CV^2}{2} + \frac{LI^2}{2}. \tag{2.13}$$

This Hamiltonian is analogous to a mechanical harmonic oscillator. If we replace L with the mass m, I with the velocity $v = \dot{x}$, $1/C$ with the spring constant k for a mass-spring system and CV with the position x, we get the Hamiltonian $H = m\dot{x}^2/2 + kx^2/2$. This Hamiltonian describes the total energy of a classical mass-spring system where the resonant frequency $f = 2\pi\sqrt{k/m}$. For the LC resonator the resonant frequency is $f = 2\pi/\sqrt{LC}$.

The Hamiltonian for the LC resonator in Eq. (2.13) is so far classical. By promoting the charge and flux coordinates to quantum operators obeying the commutation relation in Eq. (2.7), the LC resonator can be described quantum mechanically. The charge can be measured as the number of Cooper pairs at the node $n = -Q/2e$ (marked with Φ in Figure 2.1) and the phase difference across the inductor can be defined as $\phi = 2\pi\Phi/\Phi_0$, where $\Phi_0 = h/2e$ is the superconducting magnetic flux quantum. Then the quantum mechanical Hamiltonian for the LC resonator becomes

$$H_{LC} = 4E_C n^2 + \frac{E_L}{2}\phi^2. \tag{2.14}$$

Here $E_C = e^2/2C$ is the charging energy required to move an electron of a Cooper pair to the node in Figure 2.1 and $E_L = (\Phi_0/2\pi)^2/L$ is the inductive energy. This Hamiltonian is a quantum harmonic oscillator and is identical to the one for a particle in a one-dimensional quadratic potential. The second term describing the potential energy is quadratic and it produces the shape of the potential in Figure 2.2. The discrete energy levels in Figure 2.2 are equidistantly spaced and corresponds to the eigenenergies for an infinite number of eigenstates $|k\rangle$, $k = 0, 1, 2...$, as the solution to the Schrödinger Eq. (2.1) for H_{LC}. The spacing between the energy levels is hf, where $f = \sqrt{8E_L E_C}/h = 2\pi/\sqrt{LC}$ is the resonant frequency of the quantum harmonic oscillator [120].

Since the energy levels are equidistantly spaced in the quantum harmonic oscillator, it is difficult to address certain energy levels separately. For instance a signal applied to drive the quantum harmonic oscillator from its ground state $|0\rangle$ to the first excited

state $|1\rangle$ may also excite higher energy levels and then we do not know in which state the quantum harmonic oscillator is. In order to drive transitions without exciting higher energy levels, the spacing of the energy levels should be non-equidistant so that the transitions can be addressed individually. To design such a system, we need to introduce nonlinearity to the system to create a quantum anharmonic oscillator. A common way to do this is by replacing the inductor with a Josephson junction.

2.1.2 Josephson junctions

A Josephson junction has two superconductors interrupted by a weak link, for instance a thin barrier of insulating material or normal metal or a section where the superconductivity is weakened. In 1962, Josephson predicted that Cooper pairs can tunnel through this weak link, resulting in a supercurrent

$$I_S(t) = I_C \sin \phi(t) \tag{2.15}$$

even at zero voltage across the junction [121]. The critical current $I_C = \pi\Delta/(2eR_N)$ is the maximum value of the supercurrent that can flow through the junction without resistance. It is limited by the choice of the normal resistance R_N of the two SQUID barriers. Δ is the BCS superconducting energy gap and it is 200 ueV for thin film aluminum, which has a critical temperature of ∼1.3 K. If the current exceeds I_C, quasiparticles can tunnel and the junction becomes resistive. ϕ is the phase difference between the wave functions of the superconductors separated by the weak link and e is the elementary charge.

For a voltage across the junction, the phase difference evolves in time according to

$$\frac{d\phi(t)}{dt} = \frac{2e}{\hbar}V(t) = \frac{2\pi}{\Phi_0}V(t), \tag{2.16}$$

where Φ_0 is the magnetic flux quantum [121]. Using Eq. (2.15) to express $d\phi/dt$ Eq. (2.16) can be rewritten to

$$V(t) = \frac{\Phi_0}{2\pi}\frac{1}{I_C \cos\phi(t)}\frac{dI_S(t)}{dt}. \tag{2.17}$$

Comparing this to the classical expression for an inductor ($V = LdI/dt$), the Josephson junction can be modeled as a nonlinear inductor

$$L_J(t) = \frac{\Phi_0}{2\pi}\frac{1}{I_C \cos\phi(t)}. \tag{2.18}$$

Further, if Eq. (2.16) and Eq. (2.4) are compared, the phase difference across the junction can be expressed in terms of flux:

$$\phi = 2\pi\Phi/\Phi_0. \tag{2.19}$$

Thus, the Josephson junction can be covered by the Lagrangian description. The energy

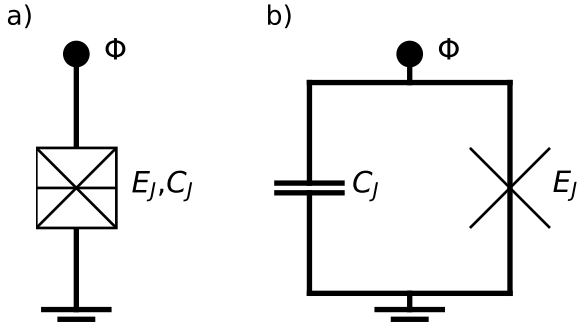

Figure 2.3: The circuit diagrams in a) and b) are equivalent and describe the same Josephson junction. The circuit consist of a capacitance C_J and a Josephson energy E_J and the flux node is marked with Φ.

of the Josephson junction

$$E_J = \int_{-\infty}^{t} P(t')dt' = \int_{-\infty}^{t} I(t')V(t')dt' = \int_{-\infty}^{t} I_c \sin\phi \frac{\Phi_0}{2\pi}\frac{d\phi}{dt'}dt' = \frac{I_C\Phi_0}{2\pi}\int_0^{\phi} sin\phi' d\phi' = \\ = \frac{I_C\Phi_0}{2\pi}(1-\cos\phi) = E_{J,\max}(1-\cos\phi), \tag{2.20}$$

where $E_{J,\max}$ is the Josephson energy of the junction. Since we are using flux nodes as generalized coordinates, E_J corresponds to a potential term in the Lagrangian.

So far, the description has been of an ideal Josephson junction. However, a real Josephson junction has capacitive properties as well and can be modeled as a nonlinear inductance in parallel with a capacitance C_J (see Figure 2.3). Using the Lagrangian for a capacitor in Eq. (2.10) and the energy for the nonlinear inductor in Eq. (2.20), the Lagrangian for the Josephson junction is

$$\mathcal{L}_J = \frac{C_J\dot{\Phi}^2}{2} - E_{J,\max}(1-\cos\phi). \tag{2.21}$$

The second term describing the nonlinear inductor is a cosine function instead of the quadratic function as in Eq. (2.11) for a classical inductor. Circuits with classical inductors and capacitors can only produce harmonic LC-oscillators, whereas circuits with Josephson junctions can be used to build anharmonic oscillators such as artificial atoms. The key element for building these anharmonic level structures is the nonlinearity provided by the cosine function.

2.1.3 Superconducting Quantum Interference Devices

If one or more Josephson junctions are placed in a superconducting loop, it will be possible apply an external magnetic field to thread a flux Φ_{ext} through the loop to change the Josephson energy. This type of circuit element is called a Superconducting Quantum Interference Device (SQUID) and is often used in superconducting artificial atoms because of its tunability. The type of SQUID used in this thesis has two Josephson junctions, see Figure 2.4, and is the so-called DC SQUID.

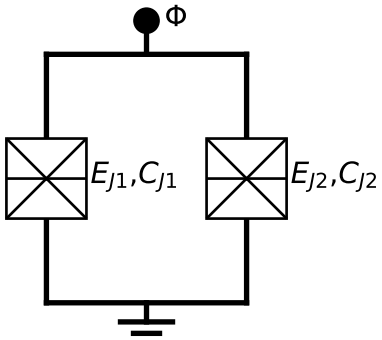

Figure 2.4: Circuit diagram of a DC SQUID: a superconducting loop interrupted by two Josephson junctions. Each Josephson junction has a capacitance C_{Ji} and Josephson energy E_{Ji}, for $i = 1, 2$. The flux node is marked with Φ.

The SQUID is described by the Schrödinger equation (Eq. (2.1)), where the state vector Ψ is the complex order parameter introduced in Ginzburg-Landau theory such that the local density of the superconducting electrons is described by $|\Psi^2|$. The order parameter must be single valued, which for a SQUID leads to fluxoid quantization [117]. This means that when completing the loop the phase of the condensate can only change with multiples of 2π and the flux is quantized in multiples of Φ_0. For the DC SQUID this results in

$$\Phi_{\text{ext}} + \Phi_{\text{ind}} + \Phi_1 - \Phi_2 = n\Phi_0, \tag{2.22}$$

using Eq. (2.19), the phase difference across the two junctions $2\pi\Phi_1/\phi_0$ and $2\pi\Phi_1/\phi_0$, the external magnetic flux through the loop Φ_{ext} and the flux induced by a circulating current Φ_{ind} in the loop inductance. Note that the flux across the two junctions have different signs due to the circulating current in the two branches of the loop. For a small loop Φ_{ind} can be neglected. The integer n is set by the number of flux quanta in the loop, which depends on the external magnetic flux according to

$$n - \frac{1}{2} < \frac{\Phi_{\text{ext}}}{\Phi_0} < n + \frac{1}{2}. \tag{2.23}$$

Introducing a new flux variable $\Phi = \frac{1}{2}(\Phi_1 + \Phi_2)$, Eq. (2.22) can be rewritten to

$$\Phi_1 = \Phi - \tfrac{1}{2}(\Phi_{\text{ext}} - n\Phi_0) \tag{2.24}$$

$$\Phi_2 = \Phi + \tfrac{1}{2}(\Phi_{\text{ext}} - n\Phi_0). \tag{2.25}$$

Assuming a symmetric SQUID, the two Josephson junctions have the same capacitance and the same Josephson energy ($C_{J1} = C_{J2} = C_J$ and $E_{J1} = E_{J2} = E_J$). Then the Lagrangian becomes

$$\begin{aligned}\mathcal{L}_{\text{SQUID}} &= \frac{C_J\left(\dot{\Phi}_1^2 + \dot{\Phi}_2^2\right)}{2} + E_{J,max}\left(\cos\frac{2\pi\Phi_1}{\Phi_0} + \cos\frac{2\pi\Phi_2}{\Phi_0}\right) = \\ &= C_J\dot{\Phi}^2 + 2E_{J,\max}\left|\cos\frac{\pi\Phi_{\text{ext}}}{\Phi_0}\right|\cos\frac{2\pi\Phi}{\Phi_0}\end{aligned} \tag{2.26}$$

using Eq. (2.24) and (2.25) and dropping the constant terms since they do not affect the dynamics of the SQUID. If this Lagrangian is compared to the Lagrangian in Eq. (2.21),

the symmetric DC SQUID behaves like a single Josephson junction with a capacitance of $2C_J$ and a tunable Josephson energy

$$E_J(\Phi_{\text{ext}}) = 2E_{J,\max}\left|\cos\frac{\pi\Phi_{\text{ext}}}{\Phi_0}\right|. \tag{2.27}$$

As seen in Eq. (2.18), the Josephson junction acts as a nonlinear inductor. Similarly, the SQUID acts as a nonlinear inductor with

$$L_J(\Phi_{\text{ext}}) = \frac{\hbar}{2eI_C|\cos(\pi\Phi_{\text{ext}}/\Phi_0)|}, \tag{2.28}$$

which can be tuned using an external magnetic flux. The tunability is important in many applications, such as for superconducting artificial atoms used in this thesis work.

2.2 Superconducting artificial atoms

Artificial atoms can be made in superconducting circuits as small circuits designed to have an atom-like energy structure. They can exhibit quantum behavior if the temperature is low enough and they can be made to interact with electric microwave signals on chip. This version of quantum optics is known as cavity QED if the interaction is with superconducting cavities [8, 13], or waveguide QED in the interaction is in open transmission lines [122–125].

A superconducting artificial atom is based on a nonlinear element, such as a Josephson junction or a SQUID, together with traditional linear circuit elements, such as a capacitance. The nonlinear element causes the energy levels of the artificial atom to be separated non-equidistantly, essentially perturbing the equal spacing of the energy levels for a simple harmonic oscillator. (Compare the quantum harmonic oscillator in Figure 2.2 to the quantum anharmonic oscillator in Figure 2.5.) The transitions between these energy states define the frequencies at which the artificial atom can absorb and re-emit electromagnetic or acoustic energy (see Chapter 3.6), *i.e.* get excited by or emit photons or phonons. If a SQUID is used as the nonlinear element, these transition frequencies can be tuned *in situ* using an external magnetic flux. If the transition between the two lowest energy levels can be addressed separately from higher energy levels, the artificial atom can be used as a quantum-bit (qubit) to store and process quantum information.

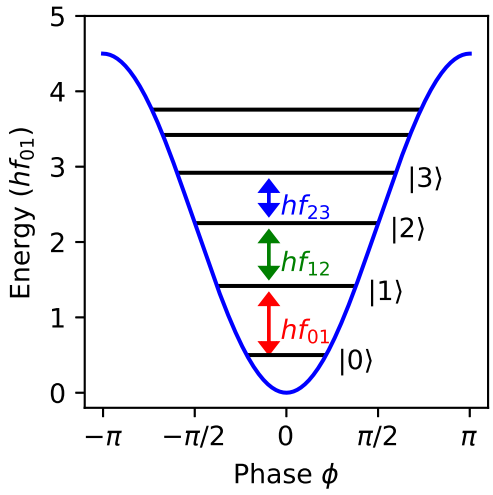

Figure 2.5: The energy spectrum of a quantum anharmonic oscillator is discrete and the shape of the potential is a cosine function (blue line). Due to this potential the energy levels (black lines) are non-equidistantly separated such that the transition frequencies are different. Depending on if the anharmonicity is negative or positive, the separation between the energy levels either decreases such that $hf_{01} > hf_{12} > hf_{23} > ...$ as in the figure or increases such that $hf_{01} < hf_{12} < hf_{23} < ...$ (not shown in the figure).

2.2.1 The Cooper Pair Box

There are several ways to design superconducting artificial atoms. In this thesis we have used the transmon [37], which is a variant of the Cooper Pair Box (CPB) [126, 127]. The circuit diagram of a CPB can be seen in 2.6 where a small superconducting island (at the node Φ) is coupled to a superconducting reservoir via a Josephson junction. In Figure 2.6 the Josephson junction is exchanged with a SQUID to produce a tunable Josephson energy $E_J(\Phi_{\text{ext}})$ (see Eq. (2.27)). The Josephson junctions allows Cooper pairs to tunnel onto and off the island from the reservoir and charge the island. These charges can be induced by a voltage source via a gate capacitance C_g.

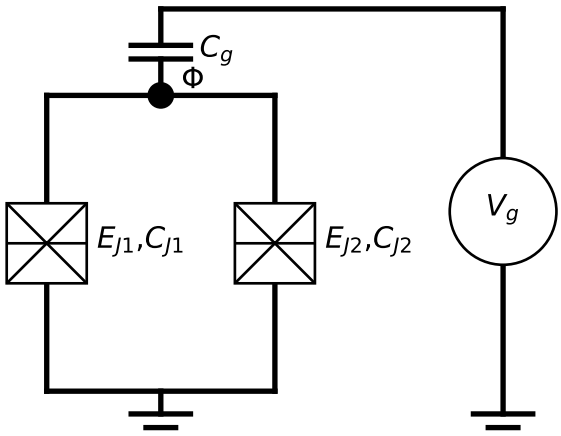

Figure 2.6: Circuit diagram of a Cooper Pair Box (CPB). The number of Cooper pairs on the superconducting island (node Φ) can be adjusted using a voltage source V_g, capacitively coupled via C_g to the island. Here the island is coupled to ground via a SQUID, which enables tuning of the Josephson energy by changing the external magnetic flux through the SQUID loop.

The Lagrangian for the circuit in Figure 2.6 can be found using Eq. (2.4), (2.10) and (2.26) (for the SQUID, if one Josephson is used use Eq. (2.21) instead). The Lagrangian

$$\mathcal{L}_{\text{CPB}} = \frac{C_g}{2}\left(\dot{\Phi} - V_g\right)^2 + \mathcal{L}_{\text{SQUID}} = \frac{C_g}{2}\left(\dot{\Phi} - V_g\right)^2 + \frac{C_J}{2}\dot{\Phi}^2 + E_J(\Phi_{\text{ext}})\cos\frac{2\pi\Phi}{\Phi_0} \quad (2.29)$$

where $C_J = 2C$ is the collective capacitance of both Josephson junctions in the SQUID and Φ is the flux at the island node. Inserting $\mathcal{L}_{\text{CPB}}$ in Eq. (2.5), the Hamiltonian becomes

$$H_{\text{CPB}} = \frac{C_g + C_J}{2}\dot{\Phi}^2 - \frac{C_g V_g^2}{2} - E_J(\Phi_{\text{ext}}) \cos \frac{2\pi\Phi}{\Phi_0}, \tag{2.30}$$

which can be rewritten to

$$H_{\text{CPB}} = \frac{(Q + C_g V_g)^2}{2(C_g + C_J)} - E_J(\Phi_{\text{ext}}) \cos \phi, \tag{2.31}$$

where constant term $(C_g V_g^2/2)$ is neglected since it does not depend on Q and the node charge

$$Q = \frac{\partial \mathcal{L}_{\text{CPB}}}{\partial \dot{\Phi}} = (C_g + C_J)\dot{\Phi} - C_g V_g. \tag{2.32}$$

The island charge is measured in number of Cooper pairs on the island $n = -Q/2e$ and the number of Cooper pairs induced by the voltage source is given by $n_g = C_g V_g/2e$. Defining the charging energy $E_C = e^2/2C_\Sigma$ for $C_\Sigma = C_g + C_J$ as the total capacitance, the Hamiltonian is

$$H_{\text{CPB}} = 4E_C(n - n_g)^2 - E_J(\Phi_{\text{ext}}) \cos \phi. \tag{2.33}$$

In the same way as the third step in Section 2.1, we promote Φ and Q to operators, obeying the canonical commutation relation in Eq. (2.7). This implies $[n, \phi] = i$ and using Baker-Hausdorf lemma, [119] it can be rewritten as $[e^{i\phi}, n] = e^{i\phi}$. Then $e^{\pm i\phi}|n\rangle = |n \pm 1\rangle$, where $|n\rangle$ is the charge eigenbasis of the Cooper pair operator n and counts the number of Cooper pairs. The Hamiltonian can then be projected onto the charge eigenbasis using $\cos \phi = (e^{i\phi} + e^{-i\phi})/2$,

$$H_{\text{CPB}} = \sum_n \left(4E_C(n - n_g)^2 |n\rangle\langle n| - \frac{E_J(\Phi_{\text{ext}})}{2}(|n-1\rangle\langle n| + |n+1\rangle\langle n|) \right). \tag{2.34}$$

From H_{CPB} the energy level structure of the CPB can be divided in two different regimes; the charge regime when $E_J \lesssim E_C$ and the phase regime when $E_J \gg E_C$. In the charge regime, the energy spectrum is highly dependent on n_g. Although V_g can be applied such that $n_g = 0.5$ separating the two lowest energy levels well from higher energy levels and the CPB can be used as a qubit, n_g can change when unwanted charges are induced by noise from the environment. This changes the energy spectrum. In this way, the CPB is sensitive to charge noise. In order to decrease the effect of charges from the environment, E_J/E_C is increased and the dependence of n_g decreases. This is the phase regime and operating the CPB in this regime, it is known as a transmon.

2.2.2 The transmon

A transmon is operated in the phase regime where $E_J \gg E_C$ and the energy levels are much less affected by n_g. A common way to reduce E_C is to add a capacitance C_s shunting the SQUID (see Figure 2.7). For increased E_J/E_C the energy level structure becomes less anharmonic. Anharmonicity is needed in order to address certain transitions between energy levels separately, which is necessary in order to use the transmon as a qubit.

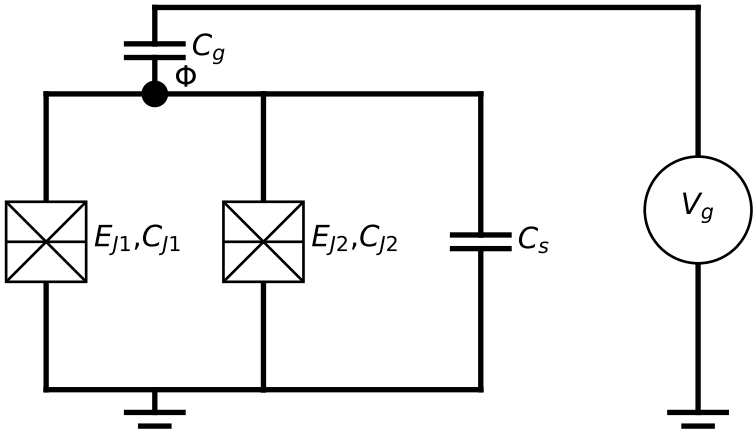

Figure 2.7: Circuit diagram of a Transmon: a Cooper pair box with an additional shunt capacitance (C_s) such that it is less sensitive to charge noise. The superconducting island (node Φ) is coupled to ground via a capacitively shunted SQUID, which enables tuning of the Josephson energy by changing the external magnetic flux through the SQUID loop.

Since E_C is decreased more charge states need to be accounted for and the charge eigenbasis is no longer sufficient. Using $n = -i\partial/\partial\phi$ we can express n in the phase eigenbasis instead. Then the Hamiltonian in Eq. (2.33) becomes

$$H_{\mathrm{T}} = 4E_C \left(-i\frac{\partial}{\partial\phi} - n_g\right)^2 - E_J(\Phi_{\mathrm{ext}})\cos\phi, \tag{2.35}$$

which is used in $H_{\mathrm{T}}\Psi_m(\phi) = E_m\Psi_m(\phi)$ where $\Psi_m(\phi)$ are eigenstates expressed in the phase basis and E_m are the energy levels.

In Section 2.1 we saw that contributions from capacitors can be viewed as kinetic energy and contributions from inductors can be viewed as potential energy. Using the same argument, E_C can be viewed as kinetic energy and E_J as potential energy. Since $E_C \ll E_J$ the potential energy dominates and $\cos\phi$ can be approximated with its Taylor expansion around zero, $\cos\phi \approx 1 - \phi^2/2 + \Phi^4/24 - ....$ The leading term in the Taylor expansion is a quadratic term and, without the other terms, this will produce the harmonic oscillator described in Section 2.1.1. Therefore, we can treat this as a perturbation from the exact harmonic solution and then the energy levels of the transmon can be approximated with

$$E_m \approx -E_J + \sqrt{8E_JE_C}\left(m + \frac{1}{2}\right) - \frac{E_C}{12}\left(6m^2 + 6m + 3\right). \tag{2.36}$$

for $m = \{0, 1, 2, ...\}$ [37]. From this, we can get the anharmonicity

$$\alpha = (E_2 - E_1) - (E_1 - E_0) = E_2 + E_0 - 2E_1 = -E_C. \tag{2.37}$$

which is small compared to the energy transitions

$$hf_{m+1,m} = E_{m+1} - E_m = \sqrt{8E_J E_C} - E_C(m+1) \tag{2.38}$$

since $E_C \ll E_J$. Although the anharmonicity of the transmon is limited, it is sufficiently large to use the transmon as a qubit. Thus, the transmon is and has been frequently used in superconducting circuits to study various quantum phenomena as well as systems towards realizing a quantum computer [9, 120, 128, 129].

The transmon and the Cooper pair box are just two of many types of superconducting structures used for quantum experiments. An advantage using superconducting circuits is the possibility to design and fabricate them with lithography processes to suit certain experiments. In this way it possible to pinpoint unique physical phenomena to study and also to combine different types of quantum systems, for instance coupling superconducting qubits to mechanical systems to study quantum acoustics [9] which is the focus of this thesis.

2.3 Interaction between an atom and a propagating field

As described in Section 2.2 superconducting artificial atoms can be designed to interact with electric microwave signals, either with certain modes in a cavity or with a propagating field in an open transmission line (TL). In this thesis we focus on propagating fields and this section describes interaction between a propagating field and an artificial atom, following the derivation in Ref. [130] and [131], with the aim to obtain the reflection and transmission coefficients. These coefficients will be obtained for an atom considered as a two-level system in a propagating electromagnetic field in the Section 2.3.3 and for a three-level system interacting with two electromagnetic fields in the Section 2.4.

Electromagnetic waves propagate in a TL or a waveguide. For on-chip superconducting circuits the TL is commonly a coplanar waveguide (CPW) [132] consisting of a center conductor in between two ground planes.

The TL is typically longer than the wavelength of the field, and consequently it cannot be described by a single lumped element as previous circuit elements. In order to use the lumped element approximation in Section 2.1, the TL is divided into small parts with length Δx such that the field in each part is approximately constant (see Figure 2.8).

For a transmission line with inductance L_0 and capacitance C_0 per unit length, the Lagrangian can be written as

$$\mathcal{L}_{\mathrm{TL}} = \sum_n \left(\frac{\Delta x C_0 \dot{\Phi}_n^2}{2} - \frac{(\Phi_{n+1} - \Phi_n)^2}{2\Delta x L_0} \right) = \sum_n \left(\frac{Q_n^2}{2\Delta x C_0} - \frac{(\Phi_{n+1} - \Phi_n)^2}{2\Delta x L_0} \right) \tag{2.39}$$

using the conjugate momenta (node charge) $Q_n = \Delta x C_0 \dot{\Phi}_n$ and the coordinates (flux nodes) Φ_n.

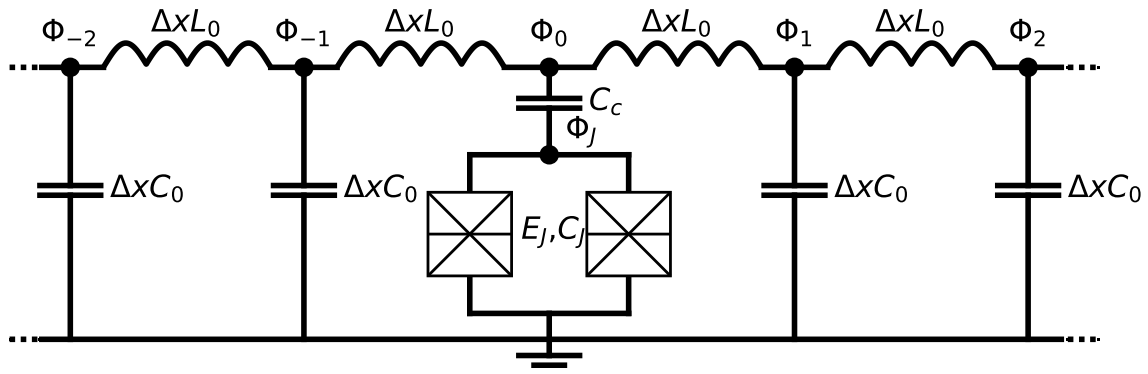

Figure 2.8: Circuit diagram of a transmon in an open transmission line. The shunt capacitance is included in C_J and the transmon couples to the transmission line via the coupling capacitance C_c.

If we let the propagating field in the TL interact with the transmon described in Section 2.2.2, we can assign node indices $n < 0$ to the TL on the left of the transmon and $n > 0$ to the TL on the right side of the transmon (see Figure 2.8). The transmon has node index J and is coupled to the TL at node index $n = 0$ through the capacitance C_c and Josephson energy E_J. Thus, using Eq. (2.39) and (2.29) with $Q_0 = C_c\left(\dot{\Phi}_0 - \dot{\Phi}_J\right)$, $Q_J = (C_c + C_J)\,\dot{\Phi}_J - C_c\dot{\Phi}_J$, the Lagrangian for the system

$$\mathcal{L} = \sum_{n<0}\left(\frac{Q_n^2}{2\Delta x C_0} - \frac{(\Phi_{n+1}-\Phi_n)^2}{2\Delta x L_0}\right) + \sum_{n>0}\left(\frac{Q_n^2}{2\Delta x C_0} - \frac{(\Phi_{n-1}-\Phi_n)^2}{2\Delta x L_0}\right) + \\ + \frac{(Q_0+Q_J)^2}{2C_J} + \frac{Q_0^2}{2C_c} + E_J(\Phi_{\text{ext}})\cos\frac{2e\Phi_J}{\hbar} \tag{2.40}$$

where the conjugate momenta Q_n to the flux nodes Φ_n fulfill the canonical commutation relations $[\Phi_n, Q_m] = i\hbar\delta_{nm}$ and $[\Phi_n, \Phi_m] = [Q_n, Q_m] = 0$. From the Lagrangian we obtain the Hamiltonian

$$H = \sum_{n\neq 0}\frac{Q_n^2}{2\Delta x C_0} + \sum_{-\infty}^{\infty}\frac{(\Phi_{n+1}-\Phi_n)^2}{2\Delta x L_0} + \frac{(Q_0+Q_J)^2}{2C_J} + \frac{Q_0^2}{2C_c} - E_J\cos\frac{2e\Phi_J}{\hbar}, \tag{2.41}$$

describing the combined system where the transmon interacts with an open TL.

The time evolution of the Q_n and Φ_n operators can be expressed by the Heisenberg's equation of motion for operators in Eq. (2.2) [130,131]. Using the canonical commutation relations above, we obtain

$$\partial_t\Phi_n = \frac{Q_n}{\Delta x C_0} \quad \text{for } n \neq 0, \tag{2.42a}$$

$$\partial_t\Phi_0 = \frac{Q_0+Q_J}{C_J} + \frac{Q_0}{C_c}, \tag{2.42b}$$

$$\partial_t\Phi_J = \frac{Q_0+Q_J}{C_J} \tag{2.42c}$$

$$\partial_t Q_n = \frac{\Phi_{n-1}-2\Phi_n+\Phi_{n+1}}{\Delta x L_0} \tag{2.42d}$$

$$\partial_t Q_0 = \frac{\Phi_{-1}-2\Phi_0+\Phi_1}{\Delta x L_0} \tag{2.42e}$$

$$\partial_t Q_J = -E_J\frac{2e}{\hbar}\sin\frac{2e\Phi_J}{C_J}. \tag{2.42f}$$

2.3.1 The continuum limit

In the continuum limit $\Delta x \to dx$ and we choose the coordinate x such that the transmon is located at $x = 0$. Then $\Phi_n(t)$ becomes a flux field $\Phi(t, x)$ and $Q_n(t)/\Delta x$ becomes a charge density field $Q(t, x)$ for $x \neq 0$. $\Phi(t, x)$ and $Q(t, x)$ are canonical field operators and satisfy the equal-time commutation relation $[\Phi(t, x), Q(t, x')] = i\hbar\delta(x - x')$.

Away from the transmon ($x \neq 0$), the continuum equations of motion corresponding to Eq. (2.42a) and (2.42d) can be obtained by letting $\Delta x \to 0^-$ for $n < 0$ and $\Delta x \to 0^+$ for $n > 0$. Then

$$\partial_t \Phi(t, x) = \frac{Q(t, x)}{C_0} \qquad \text{and} \qquad \partial_t Q(t, x) = \frac{\partial_x^2 \Phi(t, x)}{L_0}, \tag{2.43}$$

which can be combined into the massless Klein-Gordon equation in one spatial dimension [130, 131]. Assuming plane waves, the solutions for right- ($\rightarrow$) and left-propagating ($\leftarrow$) parts of the field away from $x = 0$ can be written as

$$\Phi^{\rightleftarrows}(t, x) = \sqrt{\frac{\hbar Z_0}{4\pi}} \int_0^\infty \frac{d\omega}{\sqrt{\omega}} \left(a_\omega^{\rightleftarrows} e^{-i(\omega t \mp k_\omega x)} + (a_\omega^{\rightleftarrows})^\dagger e^{i(\omega t \mp k_\omega x)} \right) \tag{2.44a}$$

$$Q^{\rightleftarrows}(t, x) = i\sqrt{\frac{\hbar Z_0}{4\pi}} \int_0^\infty d\omega \sqrt{\omega} \left(a_\omega^{\rightleftarrows} e^{-i(\omega t \mp k_\omega x)} - (a_\omega^{\rightleftarrows})^\dagger e^{i(\omega t \mp k_\omega x)} \right), \tag{2.44b}$$

where $a_\omega^{\rightleftarrows}$ and $(a_\omega^{\rightleftarrows})^\dagger$ are the bosonic creation and annihilation operators for right- and left-moving plane waves with frequency ω.

These operators obey the canonical commutation relations $[a_\omega^{\rightarrow}, (a_{\omega'}^{\rightarrow})^\dagger] = [a_\omega^{\leftarrow}, (a_{\omega'}^{\leftarrow})^\dagger] = \delta(\omega - \omega')$ and $[a_\omega^{\leftarrow}, (a_{\omega'}^{\rightarrow})^\dagger] = [a_\omega^{\leftarrow}, a_{\omega'}^{\leftarrow}] = 0$ [130, 131]. The wavenumber k_ω is expressed in terms of frequency and the dispersion relation follows $\omega = v_0 k_\omega$, where $v_0 = 1/\sqrt{L_0 C_0}$ is the speed of the propagating fields in the TL. $Z_0 = \sqrt{L_0/C_0}$ is the characteristic impedance of the TL.

At $x = 0$ the flux field is continuous, and consequently $\Phi_0 = \Phi(t, 0)$ (not to be confused with the flux quantum). However, the node at $n = 0$ has a finite capacitance C_c, implying that the spatial derivative of the flux field does not have to be continuous at $x = 0$ [131]. In the continuum limit at $x = 0$ Eq. (2.42e) becomes

$$\partial_t Q_0 = -\frac{\partial_x \Phi(t, 0^+) + \partial_x \Phi(t, 0^-)}{L_0} = \frac{\partial_t (\Phi^{\leftarrow}(t, 0^+) - \Phi^{\rightarrow}(t, 0^+) + \Phi^{\rightarrow}(t, 0^-) - \Phi^{\leftarrow}(t, 0^-))}{Z_0}, \tag{2.45}$$

using the relation $\partial_x \Phi^{\rightleftarrows}(x, t) = \mp v_0^{-1} \partial_t \Phi^{\rightleftarrows}(x, t)$ for $x < 0$ and $\partial_x \Phi^{\rightleftarrows}(x, t) = \pm v_0^{-1} \partial_t \Phi^{\rightleftarrows}(x, t)$ for $x > 0$ from Eq. (2.44). $\Phi(t, 0^-)$ is the total flux field equal to the sum of incoming $\Phi^{\rightarrow}(t, 0^-)$ and outgoing flux field $\Phi^{\leftarrow}(t, 0^-)$ for $\Delta x \to 0^-$. Similarly $\Phi(t, 0^+)$ is the total flux field equal to the sum of incoming $\Phi^{\leftarrow}(t, 0^+)$ and outgoing flux field $\Phi^{\rightarrow}(t, 0^+)$ for $\Delta x \to 0^+$. $\Phi_0 = \Phi(t, 0) = \Phi(t, 0^-) = \Phi(t, 0^+)$, since the flux field is continuous at $x = 0$. Thus, Eq (2.45) can be rewritten to

$$\partial_t Q_0 = \frac{\partial_t \Phi^{\text{in}}(t, 0) - \partial_t \Phi^{\text{out}}(t, 0)}{Z_0}, \tag{2.46}$$

where $\Phi^{\text{in}}(t,0)$ and $\Phi^{\text{out}}(t,0)$ are the incoming and outgoing fields from both sides at $x=0$.

Now the equations of motion in the continuum limit can be expressed by Eq. 2.42b, 2.42c, 2.42f, 2.43 and 2.45 and the Hamiltonian can be written as

$$H = \int \frac{Q(t,x)^2}{2C_0}dx + \frac{1}{2L_0}\int \left(\frac{\partial\Phi(t,x)}{\partial x}\right)^2 dx + \frac{(Q_0+Q_J)^2}{2C_J} + \frac{Q_0^2}{2C_c} - E_J\cos\frac{2e\Phi_J}{\hbar}. \quad (2.47)$$

In this way the TL is modeled as a bath of harmonic oscillators, with an interaction point to the transmon at $x=0$. This is an example of an open quantum system, where the interaction between the system (the transmon) and the surroundings (the TL) is not negligible. The surrounding environment is often called a bath and usually contains many degrees of freedom, which are impossible to describe exactly. The total density operator $\rho_{\text{tot}}(t)$ for the combined system and bath satisfies the Liouville-von Neumann equation in Eq. 2.3 in the Schrödinger picture [133]. However, for these open quantum systems the total density operator cannot be described simply. Instead, the time evolution of the system can be described with a reduced density operator $\rho_{\text{sys}}(t) = \text{Tr}_{\text{bath}}(\rho_{\text{tot}}(t))$.

The reduced density operator effectively evolves according to a master equation, where the interaction with the bath is included but the bath degrees of freedom are traced out. In some cases, such as for the transmon in the open TL, the interaction with the environment is of great interest [130]. Then the master equation is used together with input-output equations [133].

In the following paragraphs, some steps and necessary approximations will be presented briefly. The derivations to find the master equation and the input-output equations can be found in Ref. [133] and Ref [134]. These are used to find the reflection and transmission coefficients, first, for a two-level system interacting with one field, and second, for a three-level system interacting with two fields.

2.3.2 Time evolution of an atom interacting with a transmission line

In order to find the quantum optical master equation, the Hamiltonian describing the total system is required to be on a form that can be divided into three parts; H_{sys} describing the transmon, H_{int} describing the interaction between the transmon and the TL and H_{bath} describing the TL. This is, however, not straightforward for the total Hamiltonian in Eq. 2.47 since it contains terms with Q_0. Either, approximations need to be made to go from the total Hamiltonian in Eq. (2.47) to a Hamiltonian on the required form as is done in Ref. [131] or the equations of motion need to be approximated such that they can be recognized as the quantum Langevin equations as is done in Ref. [130].

In a similar way as in Ref. [130], the time integral is taken over Eq. (2.46) such that $Z_0Q_0 = \Phi^{\text{in}}(t,0) - \Phi^{\text{out}}(t,0)$. From this, using Q_0 from Eq. (2.42b), an expression for the outgoing flux field is obtained

$$\Phi^{\text{out}}(t,0) = \Phi^{\text{in}}(t,0) + \frac{Z_0C_c}{C_c+C_J}Q_J - Z_0\frac{C_cC_J}{C_c+C_J}\partial_t(\Phi^{in}(t,0) + \Phi^{\text{out}}(t,0)). \quad (2.48)$$

The last term in this expression can be neglected if the frequencies of Φ^{in} and the transmon dynamics (Q_J) are much lower than $(C_c + C_J)/Z_0 C_c C_J$ [130]. Thus, the final equations of motion are given by Eq. (2.42f) and

$$\partial_t \Phi_J = \frac{Q_J + 2C_c \partial_t \Phi^{\text{in}} + Z_0 C_c^2 \partial_t Q_J}{C_c + C_J}. \tag{2.49}$$

These equations of motion can be written on the form of the quantum Langevin equations, since both Φ_J and Q_J fulfill equation (3.1.11) in section 3.2 in Ref. [133] using $X = -Q_J$. Furthermore, the approximated Eq. (2.48) corresponds to the input-output relation [130]. From these identifications, it can be assumed that a Hamiltonian for the field, the system and the interaction can be found as separate Hamiltonians.

Using either way of approximating the total system (as in Ref. [131] or Ref. [130]) such that it can be described by a Hamiltonian on the form $H_{\text{tot}} = H_{\text{sys}} + H_{\text{int}} + H_{\text{bath}}$, Eq. 2.3 in the Schrödinger picture can be transformed into the interaction picture where arbitrary operators are given by

$$A^{\text{int}}(t) = e^{\frac{i}{\hbar}(H_{\text{sys}} + H_{\text{bath}})t} A e^{-\frac{i}{\hbar}(H_{\text{sys}} + H_{\text{bath}})t} \tag{2.50}$$

and the time evolution is governed by the interaction Hamiltonian. From here on, an operator in the interaction picture will be marked with superscript "int".

By writing the density operator in the interaction picture and tracing out the bath, an equation for $\rho_{\text{sys}}(t)$ can be found using the following assumptions:

- The system and the bath are uncorrelated at time $t = 0$.
- The interaction is weak, such that $H_{\text{int}} \ll H_{\text{sys}}, H_{\text{bath}}$.
- The bath is large compared to the system, meaning that the state of the bath does not change significantly by the interaction.

By just using these assumptions, the time evolution of the system density operator in the interaction picture depends on its state at all earlier times. To remove this dependence and turn it into a differential equation, we further assume that it is sufficient to know $\rho_{\text{sys}}^{\text{int}}(t_0)$ at one point in time t_0 to obtain $\rho_{\text{sys}}^{\text{int}}(t)$ for all $t > t_0$. This is known as the Markov approximation and it is motivated by assuming that the interaction Hamiltonian can be rewritten as a product of system and bath operators; $H_{\text{int}} = A_{\text{sys}} \otimes A_{\text{bath}}$. Then each term in the equation for $\rho_{\text{sys}}^{\text{int}}(t)$ will contain a function of the form $f(t - t') = \text{Tr}_{\text{bath}}(A_{\text{bath}}(t) A_{\text{bath}}(t') \rho_{\text{bath}})$ [134]. If $\rho_{\text{sys}}^{\text{int}}(t)$ is approximately constant during the decay time of the this function, the Markov approximation is valid. This can be interpreted as a bath without memory of interactions with the system, and if the system changes the bath this change will have decayed before it can affect the system at a later time.

Using these approximations, the differential equation

$$\partial_t \rho_{\text{sys}}^{\text{int}}(t) = -\frac{1}{\hbar^2} \int_0^\infty \text{Tr}_{\text{bath}} \left(\left[H_{\text{int}}^{\text{int}}(t), \left[H_{\text{int}}^{\text{int}}(t - t'), \rho_{\text{sys}}^{\text{int}}(t) \otimes \rho_{\text{bath}} \right] \right] \right) dt' \tag{2.51}$$

is obtained [133, 134], which is the Born-Markov master equation. From this, specific master equations can be derived by inserting appropriate forms of H_{sys} and H_{int}.

2.3.3 Interaction between a two-level atom and a propagating field

In order insert appropriate forms of H_{sys} and H_{int}, and continue following the derivation of the master equation describing the transmon interacting with an open TL in Ref. [130, 133], we want to consider the transmon as a two-level system interacting weakly with the bath (TL). This is possible if the incoming coherent signal propagating through the TL has an angular frequency ω_p close to ω_{10} and the anharmonicity is sufficiently large [130]. For a two-level system the system Hamiltonian

$$H_{\text{sys}} = -\frac{\hbar\omega_{10}}{2}\sigma_z \tag{2.52}$$

where $\hbar\omega_{10}$ is the energy difference between the two levels (*e.g.* the ground state and the first excited state of the transmon) with an angular transition frequency ω_{10}. The Pauli matrix $\sigma_z = |1\rangle\langle 1| - |0\rangle\langle 0|$.

The interaction Hamiltonian can be written as

$$H_{\text{int}} = i\int_0^\infty d\omega\kappa(\omega)\sqrt{\frac{\hbar\omega}{2}}\left(a_\omega^\dagger - a_\omega\right)X \tag{2.53}$$

where $\kappa(\omega)$ is the Fourier transform of a coupling coefficient $\kappa(x)$ [134]. The coupling coefficient is zero everywhere except a small range around $x = 0$ [134]. The operator X is a system operator coupling to the field, which is described by the Hamiltonian

$$H_{\text{bath}} = \hbar\int_0^\infty d\omega\omega a_\omega^\dagger a_\omega \tag{2.54}$$

with $[a_\omega, a_\omega^\dagger] = \delta(\omega - \omega')$ [134].

Since we want to examine scattering of a propagating field, we also include a coherent input field Φ_p in Φ^{in}. This field can be added by modifying H_{sys} in the master equation to $H_{\text{sys}} + \frac{\sqrt{2}C_c}{C_c+C_J}\Phi_p(t)X$ [130] and by assuming that the coherent voltage field impinges on the transmon with amplitude A_p and angular frequency ω_p.

The operator X can be expanded in eigenoperators of H_{sys}, such that $X = \sum_n(X_n^+ + X_n^-)$ with $[H_{\text{sys}}, X_n^\pm] = \pm\hbar\omega_n X_n^\pm$ [130]. In this eigenbasis, $X_n^\pm$ represents the raising and lowering operators for a transition with frequency ω_n. For a two-level system there is only one transition frequency ω_{10}, then $X = X^+ + X^-$ with $X^\pm = \pm i|X_{10}|\sigma^\pm$, $X_{10} = \langle 1|X|0\rangle$, $\sigma^+ = |1\rangle\langle 0|$, $\sigma^- = |0\rangle\langle 1|$ and $[H_{\text{sys}}, X^\pm] = \pm\hbar\omega_{10}X^\pm$. Thus, this can be inserted into Eq. (2.53) and using Eq. (2.50) the interaction Hamiltonian in the interaction picture can be written as

$$H_{\text{int}}^{\text{int}}(t) = i\int_0^\infty d\omega\kappa(\omega)\sqrt{\frac{\hbar\omega}{2}}\left(a_\omega e^{-i\omega t} - a_\omega^\dagger e^{i\omega t}\right)(X^+ e^{i\omega_{10}t} + X^- e^{-i\omega_{10}t}). \tag{2.55}$$

To obtain the final master equation in the Schrödinger picture and to find a solution to it for a coherent drive, the following steps are made and can be found in Ref. [130, 134]:

1. The expression for the interaction Hamiltonian in the interaction picture (Eq. (2.55)) is inserted into Eq. (2.51).

2. The commutators and integrals are evaluated using the cyclic property of the trace and the rotating wave approximation is used.

3. The equation is transformed back to the Schrödinger picture, by using the solution of Eq. (2.50) for A. Thus, the equation describes the time evolution of the system density operator ρ_{sys}.

4. A unitary transformation to a rotating frame with frequency ω_p and a rotating wave approximation is performed on the equation for the time evolution of the system density operator. Then the equation becomes independent of time and the equation can be solved in the steady state for $\partial_t \rho_{\text{sys}} = 0$.

5. The solution is then transformed back to the non-rotating frame.

This gives us the system density matrix element

$$\rho_{01} = \frac{A_p}{2} \frac{\sqrt{\hbar\omega_{10}\Gamma_{10}Z_0}(\partial\omega_p + i\gamma_{10})}{\hbar\omega_{10}Z_0(\gamma_{10}^2 + \partial\omega_p^2) + \gamma_{10}A_p^2} e^{i\omega_p t} \tag{2.56}$$

where Γ_{10} is the relaxation rate between the first excited state and the ground state and $\partial\omega_p = \omega_p - \omega_{10}$ is the detuning between the angular driving frequency and the angular resonance frequency of the qubit. The off diagonal elements in ρ are subjected to pure exponential decay, which for ρ_{10} is the dephasing rate

$$\gamma_{10} = \Gamma_\phi + \frac{\Gamma_{10}}{2} \tag{2.57}$$

where Γ_ϕ is the pure dephasing rate. The amplitude of the incoming field A_p relates to the number of incoming photons N_{in} through

$$N_{\text{in}} = \frac{A_p^2}{2Z_0\hbar\omega_{10}} \tag{2.58}$$

according to Ref. [130].

Reflection and transmission coefficients

To understand how the transmon scatters an incoming field, we will calculate the expected reflection and transmission coefficient. The coherent input field mentioned above can be assumed as a coherent voltage field that impinges on the transmon from the left only, i.e. $V^{\rightarrow}(t, 0^-) = A_p \sin\omega_p t$ and $V^{\leftarrow}(t, 0^+) = 0$. Then, by separating the terms in Eq. 2.48 into left and right propagating waves, the reflected field can be expressed as the expectation value of the voltage

$$V^{\leftarrow}(t, 0^-) = \partial_t \Phi^{\leftarrow}(t, 0^-) = \partial_t \Phi^{\leftarrow}(t, 0^+) + \frac{Z_0 C_c}{2(C_c + C_J)} \partial_t Q_J. \tag{2.59}$$

From identifying the equations of motion as the quantum Langevin equations, $-Q_J$ was identified as the operator X and the expectation value $\langle X\rangle = Tr(\rho X)$. The time derivative of the expectation value

$$\langle \partial_t X(t)\rangle = \langle \partial_t X^+(t)\rangle + \langle \partial_t X^-(t)\rangle = i\omega_{10}(\langle X^+(t)\rangle - \langle X^-(t)\rangle) = -\omega_{10}|X_{10}|\langle \sigma_x\rangle, \quad (2.60)$$

where X^+ and X^- obeys the Heisenberg equation in Eq. 2.2 and the Pauli matrix $\sigma_x = \sigma^+ + \sigma^- = |1\rangle\langle 0| + |0\rangle\langle 1|$. Inserting this into Eq. (2.59), we obtain

$$V^{\leftarrow}(t, 0^-) = \frac{Z_0 C_c}{2(C_c + C_J)}\omega_{10}|X_{10}|\langle \sigma_x\rangle = \frac{1}{2}\sqrt{\hbar\omega_{10}\Gamma_{10}Z_0}\langle \sigma_x\rangle \quad (2.61)$$

with $\Gamma_{10} = \frac{C_c^2}{\hbar(C_c+C_J)^2} Z_0\omega_{10}|X_{10}|^2$ as the 1-0 relaxation rate [130]. This relaxation rate was found in Ref. [130], by solving Eq. 2.51 for the diagonal elements in ρ_{sys} in the steady state (by setting $\partial_t\rho_{\text{sys}} = 0$).

The expectation value of $\langle \sigma_x\rangle = Tr(\rho_{\text{sys}}\sigma_x) = \rho_{01} + \rho_{10} = 2Re[\rho_{01}]$. Using ρ_{01} from Eq. (2.56), we obtain

$$V^{\leftarrow}(t, 0^-) = \frac{\hbar\omega_{10}A_p\Gamma_{10}Z_0}{2}\frac{\partial\omega_p\cos(\omega_p t) - \gamma_{10}\sin(\omega_p t)}{\hbar\omega_{10}\gamma_{10}^2 Z_0 + \hbar\omega_{10}\partial\omega_p^2 Z_0 + A_p^2\gamma_{10}} \quad (2.62)$$

and from this the reflection coefficient is calculated to

$$r = \frac{V^{\leftarrow}(t, 0^-)}{V^{\rightarrow}(t, 0^-)} = -r_0\frac{1 - i\frac{\partial\omega_p}{\gamma_{10}}}{1 + \left(\frac{\partial\omega_p}{\gamma_{10}}\right)^2 + \frac{\Omega_p^2}{\Gamma_{10}\gamma_{10}}}, \quad (2.63)$$

where $r_0 = \Gamma_{10}/2\gamma_{10}$ and Ω_p is the Rabi frequency of the incoming field (see equation (1-2) in Ref. [125]). The squared Rabi frequency $\Omega_p^2 = 2N_{\text{in}}\Gamma_{10}$ [135] with N_{in} from Eq. (2.58). The calculation in Eq. (2.63) is done by only treating the input and output fields in terms of $e^{-i\omega_p t}$ and disregarding $e^{i\omega_p t}$ [130]. This can be done since we are interested in the amplitude and phase of the fields. If we would do the opposite and treat the input and output fields in terms of $e^{i\omega_p t}$ and disregard $e^{-i\omega_p t}$, we would obtain the complex conjugate.

Similarly, the transmitted field can be evaluated using Eq. (2.48) for right propagating fields, such that

$$V^{\rightarrow}(t, 0^+) = \partial_t\Phi^{\rightarrow}(t, 0^+) = \partial_t\Phi^{\rightarrow}(t, 0^-) + \frac{Z_0 C_c}{2(C_c + C_J)}\partial_t Q_J \quad (2.64)$$

and from this, the transmission coefficient can be expressed as

$$t = \frac{V^{\rightarrow}(t, 0^+)}{V^{\rightarrow}(t, 0^-)} = 1 + \frac{\frac{Z_0 C_c}{2(C_c+C_J)}\partial_t Q_J}{V^{\rightarrow}(t, 0^-)} = 1 + r \quad (2.65)$$

using r from Eq. (2.63). From Eq. (2.63) and Eq. (2.65), the scattering of a field from an artificial atom can be described. However, here the atom has been approximated as a two-level system and the higher energy levels have been disregarded.

2.4 Interaction between a three-level atom and two fields

In this section, one more energy level will be included, such that the transmon can be viewed as a three-level system. This three-level system interacts with two electromagnetic fields instead of one as in the previous section. We start by following the derivation in Ref. [130] and continue by following Ref. [136] to distinguish the two different regimes where either electromagnetically induced transparency or Autler-Townes splitting occurs depending on the strength of the fields and the system parameters.

Similar to the Hamiltonian for the two-level system in Eq. (2.52), the Hamiltonian for a three-level system can be written as

$$H_{\text{sys}} = \sum_{n=0}^{2} E_n |n\rangle\langle n| \tag{2.66}$$

where

$$\hbar\omega_{10} = E_1 - E_0 \text{ and } \hbar\omega_{21} = E_2 - E_1 \tag{2.67}$$

for angular transition frequencies ω_{10} and ω_{21} of the 0-1 transition and the 1-2 transition, respectively.

This three-level atom interacts with two fields; one probe field $A_p \sin\omega_p t$ with angular frequency ω_p close to ω_{10} and amplitude A_p, and one control field $A_c \sin\omega_c t$ with angular frequency ω_c close to ω_{21} and amplitude A_c. The interaction Hamiltonian is given by Eq. (2.53), but now with

$$X = i|X_{10}|\Big(|1\rangle\langle 0| - |0\rangle\langle 1|\Big) + i|X_{21}|\Big(|2\rangle\langle 1| - |1\rangle\langle 2|\Big). \tag{2.68}$$

Consequently, Eq. (2.60) can be rewritten for a three-level system as

$$\langle \partial_t X(t)\rangle = -\omega_{10}|X_{10}|\Big\langle |1\rangle\langle 0| + |0\rangle\langle 1|\Big\rangle - \omega_{21}|X_{21}|\Big\langle |2\rangle\langle 1| + |1\rangle\langle 2|\Big\rangle \tag{2.69}$$

and used in Eq. (2.59) to obtain

$$V^{\leftarrow}(t, 0^-) = \frac{\sqrt{\hbar Z_0}}{2}\left(\sqrt{\omega_{10}\Gamma_{10}}\Big\langle |1\rangle\langle 0| + |0\rangle\langle 1|\Big\rangle + \sqrt{\omega_{21}\Gamma_{21}}\Big\langle |2\rangle\langle 1| + |1\rangle\langle 2|\Big\rangle\right). \tag{2.70}$$

Thus, $V^{\leftarrow}(t, 0^-)$ includes parts with frequencies around ω_p and parts with frequencies around ω_c. Since, we are interested in the reflected and transmitted properties of the probe field we can concentrate on those parts of $V^{\leftarrow}(t, 0^-)$. The reflected probe field

$$V_p^{\leftarrow}(t, 0^-) = \frac{\sqrt{\hbar\omega_{10} Z_0 \Gamma_{10}}}{2}\Big\langle |1\rangle\langle 0| + |0\rangle\langle 1|\Big\rangle. \tag{2.71}$$

Using the same steps as for the two-level system in one field, but with the unitary transformation matrix

$$U(t) = \begin{pmatrix} 1 & 0 & 0 \\ 0 & e^{-i\omega_p t} & 0 \\ 0 & 0 & e^{-i(\omega_p+\omega_c)t} \end{pmatrix}, \tag{2.72}$$

and assuming $A_c \gg A_p$, the system density matrix element

$$\rho_{10} = -\frac{iA_p e^{-i\omega_p t}}{\sqrt{\hbar\omega_{10} Z_0}} \frac{\sqrt{\Gamma_{10}}}{2(\gamma_{10} - i\partial\omega_p) + \frac{A_c^2/2}{\hbar\omega_{21} Z_0(\gamma_{20} - i(\partial\omega_p + \partial\omega_c))}} \tag{2.73}$$

with the detunings $\partial\omega_p = \omega_p - \omega_{10}$ and $\partial\omega_c = \omega_c - \omega_{21}$. Inserting this into Eq. (2.71) using $\left\langle |1\rangle\langle 0| + |0\rangle\langle 1| \right\rangle = 2Re(\rho_{10})$ and dividing with the incoming probe field, the reflection and transmission coefficient

$$r = -\frac{\Gamma_{10}}{2(\gamma_{10} - i\partial\omega_p) + \frac{\Omega_c^2/2}{\gamma_{20} - i(\partial\omega_p + \partial\omega_c)}} \tag{2.74}$$

$$t = 1 + r = 1 - \frac{\Gamma_{10}}{2(\gamma_{10} - i\partial\omega_p) + \frac{\Omega_c^2/2}{\gamma_{20} - i(\partial\omega_p + \partial\omega_c)}}. \tag{2.75}$$

Note that these have been obtained by only treating the input and output fields in terms of $e^{-i\omega_p t}$ and disregard $e^{i\omega_p t}$ as for the two-level atom in the previous section. Ω_p and Ω_c are the Rabi frequencies for the probe and the control field, respectively [136].

2.4.1 Distinguishing electromagnetically induced transparency and Autler-Townes splitting

The scattering parameters in Eq. (2.74) and (2.75) can be evaluated using certain assumptions resulting in two different important physical phenomena; electromagnetically induced transparency (EIT) and Autler-Townes splitting. Although both these phenomena can appear as transparency windows in measurements of transmission, their origin is different. The distinction was made clear in Ref. [136]. This will be shown in the following derivation of the different regions.

For a resonant control frequency ($\partial\omega_c = 0$), Eq. (2.74) can be rewritten as

$$r = -\frac{\Gamma_{10}}{2(\gamma_{10} - i\partial\omega_p) + \frac{\Omega_c^2/2}{\gamma_{20} - i\partial\omega_p}} = -\frac{2\Gamma_{10}(\gamma_{20} - i\partial\omega_p)}{(\gamma_{10} - i\partial\omega_p)(\gamma_{20} - i\partial\omega_p) + \frac{\Omega_c^2}{4}}. \tag{2.76}$$

The poles of the reflection coefficient in Eq. (2.76) can be obtained by solving the denominator equal to zero for $s = i\partial\omega_p$. We find the two poles

$$s_\pm = \frac{\gamma_{20} + \gamma_{10}}{2} \pm \frac{\sqrt{(\gamma_{10} - \gamma_{20})^2 - \Omega_c^2}}{2}. \tag{2.77}$$

If the two poles are different, the reflection coefficient can be expressed on the form

$$r = \frac{A_+}{s_+ - s} + \frac{A_-}{s_- - s}, \quad \text{where} \quad A_\pm = \Gamma_{10}\left(1 \pm \frac{\gamma_{20} - \gamma_{10}}{\sqrt{(\gamma_{10} - \gamma_{20})^2 - \Omega_c^2}}\right). \tag{2.78}$$

If $(\gamma_{10} - \gamma_{20})^2 > \Omega_c^2$, $s_\pm$ are real and the two terms in Eq. (2.78) can be rewritten as

$$r = \frac{\frac{A_+}{s_+}}{1 - i\frac{\partial\omega_p}{s_+}} + \frac{\frac{A_-}{s_-}}{1 - i\frac{\partial\omega_p}{s_-}}. \tag{2.79}$$

These terms are Lorentzians centered at ω_{10}, one wider (s_+) and one narrower (s_-). One Lorentzian is positive and the other is negative since $s_\pm > 0$ while A_+ and A_- have different signs depending on if $\gamma_{10} > \gamma_{20}$ ($A_+ < 0$ and $A_- > 0$) or if $\gamma_{10} < \gamma_{20}$ ($A_+ > 0$ and $A_- < 0$). These Lorentzians give rise to a transparency window centered around ω_{10} caused by **Electromagnetically Induced Transparency (EIT)** [136] and appear due to interference between two ways of transiting between the state $|0\rangle$ and $|1\rangle$ of the artificial atom. One way is directly from $|0\rangle$ to $|1\rangle$ and the other is from $|0\rangle$ to $|1\rangle$ to $|2\rangle$ to $|1\rangle$. This can be thought of as Young's double slit experiment mentioned in Chapter 1.2, where the light passing through the two slits give rise to an interference pattern with dark (transparent) and light regions due to the difference in propagation distance though the two slits.

The other regime can be found by assuming that $(\gamma_{10} - \gamma_{20})^2 < \Omega_c^2$, such that $s_\pm$ and $A_\pm$ are complex. For a strong control $\Omega_c^2 \gg (\gamma_{10} - \gamma_{20})^2$

$$s_\pm \approx \frac{\gamma_{20} + \gamma_{10}}{2} \pm \frac{i\Omega_c}{2} \quad \text{and} \quad A_\pm \approx -\Gamma_{10} \pm \frac{\Gamma_{10}(\gamma_{20} - \gamma_{10})}{i\Omega_c} \approx -\Gamma_{10}. \tag{2.80}$$

Then the two terms in Eq. (2.78) can be approximated as

$$r = \frac{\frac{2\Gamma_{10}}{\gamma_{10}+\gamma_{20}}}{1 - i\frac{\partial\omega_p - \Omega_c/2}{(\gamma_{10}+\gamma_{20})/2}} + \frac{\frac{2\Gamma_{10}}{\gamma_{10}+\gamma_{20}}}{1 - i\frac{\partial\omega_p + \Omega_c/2}{(\gamma_{10}+\gamma_{20})/2}} \tag{2.81}$$

and these are two Lorentzians with equal width shifted $\pm\Omega_c/2$ from ω_{10}. This separation from ω_{10} is caused by **Autler-Townes splitting** which is due to Rabi dressed energy levels. The transparency in transmission appears due to shifted resonance frequencies instead of the interference effect resulting in EIT.

Since the signature of both Autler-Townes splitting and EIT appear as a transparency window, they might be difficult to distinguish. The threshold between the regions appear when $(\gamma_{10} - \gamma_{20})^2 - \Omega_c^2 = 0$ [136]. Then $s_+ = s_- = (\gamma_{20} + \gamma_{10})/2$ and the reflection coefficient can be expressed on the form

$$r = \frac{\frac{-4\Gamma_{10}}{\gamma_{10}+\gamma_{20}}}{1 - i\frac{\partial\omega_p - \Omega_c/2}{(\gamma_{10}+\gamma_{20})/2}} + \frac{\Gamma_{10}(\gamma_{10} + \gamma_{20})}{\left(i\partial\omega_p - \frac{\gamma_{10}+\gamma_{20}}{2}\right)^2} \tag{2.82}$$

The first term is a Lorentzian with half width at half maximum $(\gamma_{20} + \gamma_{10}/2)$ and center at ω_{10} and the second term is a squared Lorentzian.

What was reported as EIT in Ref. [137, 138] was actually found to be Aulter-Townes splitting [136]. Observations of EIT has been reported in atomic three-level systems [139,140], and in circuit QED using a three dimensional cavity [141]. An analogue to EIT has been demonstrated in optomechanical devices [142, 143] and we have demonstrated EIT in a propagating SAW field using a superconducting artificial atom in the appended Paper V. In the appended Paper V we also show the threshold distinguishing EIT from Autler-Townes splitting.

The Autler-Townes splitting was first demonstrated for a single atom in a three-dimensional space using electromagnetic waves [144, 145]. However, the extinction did

not exceed 12 % due to the spatial mode mismatch between the incident and scattered field of the single atom. By confining the propagating fields in a one-dimensional open transmission line and using an artificial atom, an extinction of 90 % [103, 137] to 99.6 % [138] was achieved. This effect is demonstrated for a superconducting artificial atom interacting with a propagating SAW field in the appended Paper IV. Both the appended Paper IV and V are described more in detail in Chapter 5.

Chapter 3

Surface Acoustic Waves

Surface acoustic waves (SAWs) are mechanical vibrations elastically propagating along the surface of solids. They were first described by Lord Rayleigh in Ref. [146], and are important in many natural phenomena, such as earthquakes. In earthquakes, they can destroy large land areas because they dissipate very little power into the bulk, allowing them to propagate very long distances. Although the low dissipation of the SAWs was found interesting, it was not until 80 years after their discovery that SAWs could be artificially generated on a piezoelectric material when the interdigital transducer (IDT) was introduced by White and Voltmer [4]. After this, many different designs followed, for instance with advanced features to shape the SAW pulse response or direct the SAW beam. Since piezoelectric materials' polarization charges are coupled to their particle displacements, electric power can be converted into SAW power and vice versa. This allows a variety of interdigitated transducers to be incorporated as electric circuit elements, such as bandpass filters, resonators and delay lines. They are also very important in many commercial applications, for instance in TV and mobile technology.

Here, we will focus on the type of SAWs that can be described as pure Rayleigh waves. These waves are confined to the surface and decay exponentially into the bulk. This chapter aims to give a brief introduction to this type of SAWs, their motion and how they can be generated, which is explained in detail in [2,3,108]. A semi-classical approximation of a qubit coupled to surface acoustic waves will also be described, following the supplementary material in the appended Paper I and the appended Paper II. For a full quantum model, the reader is referred to Refs. [96,147] and the summarized version in the appended Paper II. Later in this chapter, a unidirectional transducer generating SAWs in a preferred direction is discussed together with a more extensive model to describe its more complicated response.

3.1 Basic properties

When a SAW propagates, the material near the surface moves elliptically together with a quasi-electrostatic wave. The elliptic motion is produced from compression in the propagation direction and shearing in the direction normal to the surface [2]. Since the compressional motion dominates, the electrostatics can be described by an electric potential at the surface that only extends about a wavelength into the bulk. At the surface this potential can be expressed as a plane wave

$$\phi(x,t) = |\phi| e^{j(\omega t - kx)} \tag{3.1}$$

for a SAW propagating along the x-axis at time t with an angular frequency $\omega = 2\pi f$. $|\phi|$ is the magnitude of the wave at the surface and $k = 2\pi/\lambda$ is the wave vector for a wavelength λ of the SAW [108]. The frequency and wavelength of the SAWs are related by $\lambda = fv_0$, for a speed v_0 of the SAW.

SAWs can propagate in any material and their speed is determined by the material properties. They can be generated on piezoelectric materials, which are usually anisotropic. For a given cut of an anisotropic crystal, there are only a few directions where the SAW will propagate without curving (known as beam steering) [2].

The cut and orientation also affect the piezoelectric properties of the substrate. The strength of the electromechanical coupling coefficient K^2 depends on how the strain and stress relate to the electric field, *i.e.* how the permittivity relates to the stiffness of the material, all of which can be orientation dependent. For SAWs, K^2 is approximated as the change of speed when the SAW propagates under a metallized surface

$$K^2 = 2\frac{\Delta v}{v} = 2\frac{v_0 - v_m}{v_0}, \tag{3.2}$$

where v_0 is the speed of the SAW on a metal free surface and v_m is the speed when the surface is covered by a metal sheet [3]. K^2 is listed for some piezoelectric materials in Table 1 in the appended Paper II. For example, the strong piezoelectric material lithium niobate, Y-cut with propagation in the Z-direction, has $v_0 = 3488$ m/s and $K^2 = 4.8$ % [3]. This is almost 70 times stronger than gallium arsenide, which has $K^2 = 0.07$ % on the (100) surface with a SAW traveling along the [011] at the speed of 2864 m/s [2]. The impact of different strengths of K^2 will be seen in the next section and its importance when using SAWs in quantum experiments will be discussed in Chapter 5.2.

Another important property for SAWs is the effective dielectric permittivity ϵ_∞ of both the material that the SAW propagates and the medium above. The permittivity relates the polarization charge to an applied electric field for any dielectric material and it is usually expressed in relation to the permittivity in vacuum ϵ_0. The effective dielectric permittivity is defined such that it expresses the capacitance per unit length between two electrodes on the surface of the piezoelectric material. For YZ lithium niobate the effective dielectric permittivity $\epsilon_\infty = 46\epsilon_0$, while it is $12\epsilon_0$ for gallium arsenide [2]. The effective dielectric permittivity is, in addition to the electromechanical coupling coefficient and SAW speed, listed for some piezoelectric crystals in Table 1 in the appended Paper II. All of these properties are important to consider when generating and detecting SAWs.

3.2 Generation and detection

To generate a SAW, the simplest configuration is a single electrode IDT consisting of long electrodes in a periodic structure seen in Figure 3.1. All electrodes have the same finger width a, which is usually equal to the separation between them. The periodic structure can be divided into unit cells with length λ_0, where each unit cell has one electrode connected to the top bus and one connected to the bottom usually grounded bus.

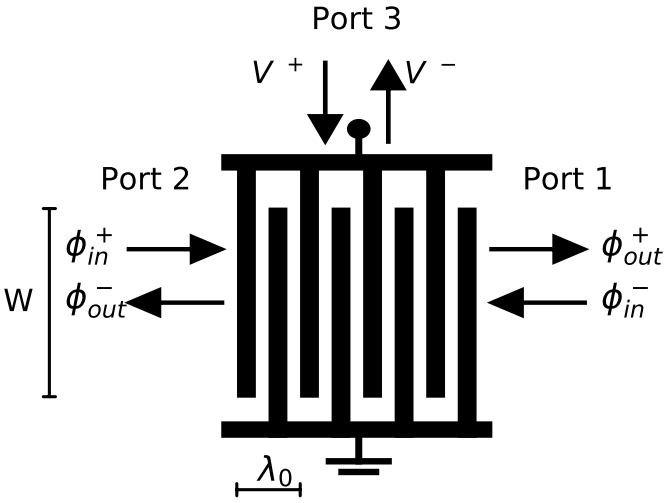

Figure 3.1: A single electrode IDT with four unit cells and an electrode overlap W. The unit cell has a length of λ_0, which defines the center frequency of the IDT. All electrodes are alternatively connected to the top live bus or the bottom grounded bus. Electric signals can be sent and detected via port 3, while port 1 and port 2 are acoustic ports.

When a voltage is applied over the IDT, an electric field is created between the electrodes connected to the top bus and the lower grounded bus. This creates strain in the underlying piezoelectric material, which generates SAWs in both directions from each unit cell. The propagating SAWs carry a total power

$$P_{\text{SAW}} = |\phi|^2 \frac{W}{\lambda} \frac{2\pi\epsilon_\infty v_0}{K^2} = |\phi|^2 Y_0, \tag{3.3}$$

where W is the beam width set by the electrode overlap (see Figure 3.1), $1/Y_0$ is the characteristic impedance from treating the IDT as a transmission line [2] and K^2 qualifies how much electric power can be converted to or from SAW power.

If the applied voltage V is on resonance with the center frequency of the IDT $f_0 = v/\lambda_0$, the contributions from all unit cells add in phase and a resonant SAW is emitted. The generated SAW carries a surface potential $\phi = VE(\omega)A(\omega)$, which is a product of the element factor $E(\omega)$ and the array factor $A(\omega)$.

The magnitude of ϕ carried by the SAW emitted by one unit cell, which in the case of a single electrode IDT is the response of the electrode connected to the top bus, is proportional to the applied voltage with a proportionality factor called the element factor. The element factor

$$E(\omega) = j\frac{K^2}{2\epsilon_\infty}\mathcal{F}\left[\rho_f\right](k), \tag{3.4}$$

describes the superposition of the response of a single electrode in the IDT. It relates to $\mathcal{F}\left[\rho_f\right](k)$, which is the Fourier transform of the surface charge density when a voltage is applied to one electrode and all other electrodes are grounded. Since $E(f)$ is varying slowly with frequency, it is usually approximated with a constant $0.84jK^2$ for single electrode IDTs [3].

The array factor is a superposition of multiple electrodes and describes the wave amplitude from the number of unit cells in the IDT, N_p. If we define the x-axis parallel with the bus bars in Figure 3.1, the electrodes connected to the top bus are centered around the coordinates $x_1, x_2, x_3 ... x_{N_p}$ and the wave amplitude due to electrode n has the form $e^{jk(x-x_n)}$. For a single electrode IDT, the coordinates x_n are evenly spaced

with $|x_{n+1} - x_n| = \lambda_0$ and by adding the amplitude contributions from each electrode connected to the top bus in the IDT, the array factor can be obtained as

$$\begin{aligned} A(\omega) = \sum_{n=1}^{N_p} e^{-jkn\lambda_0} = e^{-jk\lambda_0} \frac{1 - e^{-jkN_p\lambda_0}}{1 - e^{-jk\lambda_0}} = e^{-\frac{jk(N_p+1)\lambda_0}{2}} \frac{\sin\left(\frac{kN_p\lambda_0}{2}\right)}{\sin\left(\frac{k\lambda_0}{2}\right)} = \\ = e^{-j\pi(N_p+1)\frac{\omega}{\omega_0}} \frac{\sin\left(\pi N_p \frac{\omega}{\omega_0}\right)}{\sin\left(\pi \frac{\omega}{\omega_0}\right)} = -e^{-j\pi(N_p+1)\frac{\omega-\omega_0}{\omega_0}} \frac{\sin\left(\pi N_p \frac{\omega-\omega_0}{\omega_0}\right)}{\sin\left(\pi \frac{\omega-\omega_0}{\omega_0}\right)}. \end{aligned} \tag{3.5}$$

Here, geometric progression and Euler's formula has been used, and ω is the angular frequency of the applied voltage [3]. From the array factor, it is evident that the strength of the SAW response for a certain applied voltage increases with the number of unit cells.

In the same way as the IDT emits SAWs, it can also detect them. The incoming SAW generates a current in the IDT

$$I = -2\phi E(\omega) A(\omega) Y_0, \tag{3.6}$$

where $E(\omega)$ and $A(\omega)$ can be inserted from Eq. (3.4) and Eq. (3.5), respectively. The generated current creates a voltage and in this way the incoming SAW is converted to electric signal.

3.2.1 Three port scattering matrices

The conversion between electric signals and SAWs by the IDT, can be modeled as a complex scattering matrix with three ports; two acoustic ports (1 and 2 in Figure 3.1) and one electric port (3 in Figure 3.1)[†]. This scattering matrix relates the incoming and outgoing signals through

$$\begin{pmatrix} \phi_{out}^+ \\ \phi_{out}^- \\ V^- \end{pmatrix} = \begin{pmatrix} S_{11}S_{12}S_{13} \\ S_{21}S_{22}S_{23} \\ S_{31}S_{32}S_{33} \end{pmatrix} \begin{pmatrix} \phi_{in}^- \\ \phi_{in}^+ \\ V^+ \end{pmatrix}, \tag{3.7}$$

where the signs represent the direction of the wave. Traditionally, + is towards the right for acoustic waves and towards the IDT for electric waves. Assuming energy conservation and reciprocity the complex scattering elements can be simplified to $S_{31} = S_{13}$ and $S_{32} = S_{23}$. If the IDT is symmetric, as in the case for the single electrode IDT, this can be further simplified to $S_{31} = S_{32}$, $S_{21} = S_{12}$ and $S_{11} = S_{22}$.

A more convenient scattering matrix for IDTs is the P-matrix, where the voltage and current is related for the electric port. The P-matrix is defined as

$$\begin{pmatrix} \phi_{out}^- \\ \phi_{out}^- \\ I \end{pmatrix} = \begin{pmatrix} P_{11}P_{12}P_{13} \\ P_{21}P_{22}P_{23} \\ P_{31}P_{32}P_{33} \end{pmatrix} \begin{pmatrix} \phi_{in}^+ \\ \phi_{in}^- \\ V \end{pmatrix}, \tag{3.8}$$

[†]Note the different notation in the appended Paper 1, where port 1 is the electric port, 3 is the acoustic port facing the qubit and 2 is the other acoustic port.

where P_{13} corresponds to how much electric signal is converted into acoustic signal per unit voltage and P_{33} is the IDT admittance. Similarly to the S-matrix, the P-matrix elements can be related; $P_{21} = P_{12}$, $P_{31} = -2P_{13}$ and $P_{32} = -2P_{23}$.

The elements of the two scattering matrices are related through

$$S_{11} = P_{11} - \frac{P_{13}P_{31}}{Y_L + P_{33}}, \qquad S_{22} = P_{22} - \frac{P_{23}P_{32}}{Y_L + P_{33}}, \tag{3.9a}$$

$$S_{12} = P_{12} - \frac{P_{13}P_{32}}{Y_L + P_{33}}, \qquad S_{21} = P_{21} - \frac{P_{23}P_{31}}{Y_L + P_{33}}, \tag{3.9b}$$

$$S_{13} = \frac{2\sqrt{Y_L}P_{13}}{Y_L + P_{33}}, \qquad S_{31} = \frac{2\sqrt{Y_L}P_{31}}{Y_L + P_{33}}, \tag{3.9c}$$

$$S_{23} = \frac{2\sqrt{Y_L}P_{23}}{Y_L + P_{33}}, \qquad S_{32} = \frac{2\sqrt{Y_L}P_{32}}{Y_L + P_{33}}, \tag{3.9d}$$

$$S_{33} = \frac{Y_L - P_{33}}{Y_L + P_{33}}, \tag{3.9e}$$

where $1/Y_L$ is the characteristic load impedance of the electric transmission line, usually $50\,\Omega$ [3].

3.3 Double electrode interdigital transducers

The single electrode IDT introduced in Section 3.2 (Figure 3.1) has the most straightforward electrode configuration but it suffers from internal mechanical reflections. Internal mechanical reflections appear because each electrode (both electrodes connected to the top bus and to the bottom bus) reflects incoming SAWs weakly. In a single electrode IDT, the distance between each electrode is $\lambda_0/2$. SAWs reflected at electrode n will interfere constructively with SAWs reflected by electrode $n-1$, since it has propagated the distance between these electrode twice resulting in a phase shift of 2π. In this way, the contribution from each electrode add in phase at the center frequency producing internal mechanical reflections.

Another type of IDT with a simple electrode configuration, which does not suffer from internal mechanical reflections, is the double electrode IDT [148] in Figure 3.2a. Instead of two electrodes per unit cell, it has four: two connected to the upper live bus and two connected to the bottom grounded bus. Consequently, the distance between each electrode is $\lambda_0/4$ and SAWs reflected by electrode n travels a distance $\lambda_0/2$ further than SAWs reflected by electrode $n-1$. At center frequency, this results in a phase shift of π and destructive interference between the contributions from the electrodes. Thus, internal mechanical reflections can be neglected for double electrode IDTs close to center frequency at the cost of twice smaller lithography than the single electrode IDT. By ignoring internal mechanical reflections, the simplified response can be described by a basic SAW circuit model.

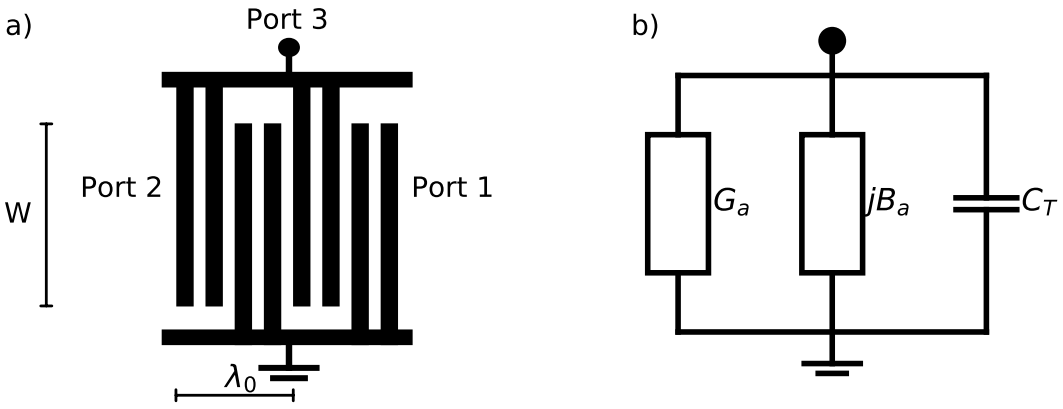

Figure 3.2: a) Double electrode IDT with electrode overlap W and unit cell length λ_0. Each unit cell has four electrodes, which makes it possible to ignore internal mechanical reflections (see text). b) The equivalent circuit of a double electrode IDT includes an acoustic conductance $G_a(\omega)$, an acoustic susceptance $B_a(\omega)$ and an electrode capacitance C_T.

3.3.1 Circuit model

The circuit model described here is a simple SAW circuit model, assuming no mechanical reflections and no loss, and it is valid for double electrode IDTs. It can also be used to approximate single electrode IDTs with few unit cells. For a more detailed description, the reader is referred to the appended Paper II and literature such as Refs. [2, 3, 107].

In the circuit model the IDT is approximated with an acoustic conductance $G_a(\omega)$, an acoustic susceptance $B_a(\omega)$ (Hilbert transform of $G_a(\omega)$) and a capacitance C_T (Figure 3.2b). The equivalent circuit has a total admittance $Y_{\mathrm{IDT}}(\omega) = G_a(\omega) + jB_a(\omega) + j\omega C_T$. These circuit elements can be calculated from the SAW theory in Section 3.2 as

$$G_a = 2|E(\omega)A(\omega)|^2 Y_0 \approx G_{a0}\left[\frac{\sin(X)}{X}\right]^2 \tag{3.10a}$$

$$B_a \approx G_{a0}\frac{\sin(2X) - 2X}{2X^2} \tag{3.10b}$$

$$C_T \approx \sqrt{2}N_p W \epsilon_\infty, \tag{3.10c}$$

where $X = \pi N_p(\omega - \omega_0)/\omega_0$ for a driving frequency ω close to ω_0. $A(\omega)$ is evaluated from Eq. (3.5) with x_t at the center of the two live electrodes and the slowly varying $E(\omega)$ is approximated with a constant $\mu_0 = c_g j K^2$ with $c_g = 0.62$ for double electrode IDTs [3]. From this the acoustic conductance at center frequency $G_{a0} = 4 \cdot c_g^2 2\pi f_0 \epsilon_\infty N_p^2 W K^2$.

Using this model, we can calculate the elements of the three-port scattering matrix

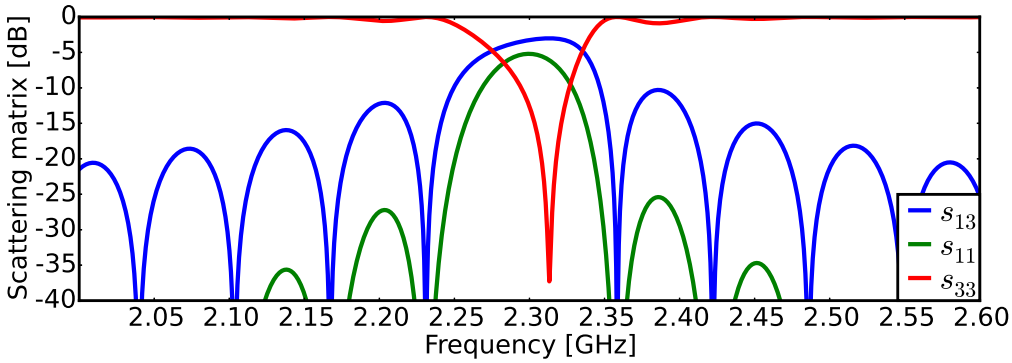

Figure 3.3: Three port scattering elements S_{13} (blue), S_{11} (green) and S_{33} (red), calculated from the circuit model for a double electrode IDT with 36 unit cells and 46 μm electrode overlap.

in Eq. (3.7) as

$$S_{11} = S_{22} = -\frac{G_a}{Y_{\mathrm{IDT}}(\omega) + Y_L} e^{-jN_p\lambda_0}, \tag{3.11a}$$

$$S_{13} = S_{23} = \frac{j\sqrt{2G_a Re(Y_L)}}{Y_{\mathrm{IDT}}(\omega) + Y_L} e^{-jN_p\lambda_0/2} \text{ and} \tag{3.11b}$$

$$S_{33} = \frac{Y_L - Y_{\mathrm{IDT}}(\omega)}{Y_L + Y_{\mathrm{IDT}}(\omega)} \tag{3.11c}$$

for a double electrode IDT with wavelength λ_0 at center frequency and hence a transducer length of $N_p\lambda_0$. The scattering parameters for a double electrode IDT with 36 number of unit cells and an electrode overlap of 46 μm is shown in Figure 3.3. The electric/SAW conversion (parameter S_{13}) is limited to a maximum of -3 dB, because IDTs have symmetric conversion into both acoustic ports. In a delay line geometry, this means that only 50 % of the power propagates in the right direction towards the other IDT. Due to reciprocity, the theoretical minimum insertion loss of a delay line with symmetric IDTs is -6 dB.

The electric reflection (parameter S_{33}) from any IDT is optimal when the IDT is impedance matched to outside electronics. The impedance matching is roughly met by designing the real part of $1/Y_{\mathrm{IDT}}$, *i.e.* G_{a0}, to be 50 Ω close to the frequency where B_a cancels C_T. Thence, there are a few design and substrate material parameters that can be used to control the impedance matching. The design parameters can be limited by the size of the substrate and the fabrication, *i.e.* the number of unit cells cannot be too many and the electrode overlap cannot be too large. A material with a higher electromechanical coupling and a higher effective dielectric constant requires fewer unit cells, such as lithium niobate in comparison to gallium arsenide.

For a fixed number of unit cells the bandwidth can be approximated with $0.9f_0/N_p$ [2]. Accordingly, the bandwidth of the double electrode IDT in Figure 3.3 is 60 MHz, but the transducer can emit and pick-up signal outside this band. In addition, the SAW emission and pick-up is slightly wider in frequency than both the acoustic reflection (parameter S_{11}) and the electric reflection (Figure 3.3).

In conclusion, to optimize an IDT the electrode configuration and the impedance matching should be considered. The IDT should be designed such that the bandwidth is sufficient for the given experiment. Therefore, the number of unit cells can be balanced with the choice of the piezoelectric substrate for optimal electric/SAW conversion. Nevertheless, symmetric IDTs are limited by the theoretical minimum insertion loss of -3 dB which should be considered when designing the experiment.

3.4 Delay line: propagation between two interdigitated transducers

Since interdigitated transducers are both emitters and receivers of SAWs, they are commonly configured in a delay line. The name comes from the use of delay lines in electric circuits, where they delay the signal the amount of time it takes the five order of magnitude slower SAW to propagate. A delay line has two interdigitated transducers separated a certain distance L on the piezoelectric substrate. If we assume that port 1 of both interdigitated transducers face into the delay line, *i.e.* towards each other, the electric signal is converted into SAWs via the scattering element S_{31}. The SAWs propagate through the delay line to the interdigitated transducer on the other side, where they are partly converted back to electric signal via S'_{13} and partly acoustically reflected back into the delay line via S'_{11}. (S denotes the scattering matrix of one interdigitated transducer and S' denotes the other.)

The response of the delay line can be measured via the electric port of each interdigitated transducer. For two identical interdigitated transducers, the matrix elements of S and S' are identical. Since multiple transitions interfere, the measured electric reflection follows

$$r = S_{33} + \sum_{n_t=1}^{\infty} S_{13}^2 S_{11}^{2n_t-1} e^{-j2n_t kL} = S_{33} + S_{13}^2 \frac{S_{11} e^{-j2kL}}{1 - S_{11}^2 e^{-j2kL}} \tag{3.12}$$

where kL is the phase the SAW picks up every time it propagates the delay line, n_t is the number of transits and the scattering elements are found from Eq. (3.7). The main electric reflection includes no SAW transits and follows S_{33}. For a multiple transiting SAW the measured transmission follows

$$t = \sum_{n_t=1}^{\infty} S_{13}^2 S_{11}^{2(n_t-1)} e^{-j(2n_t-1)kL} = S_{13}^2 \frac{e^{-jkL}}{1 - S_{11}^2 e^{-j2kL}}, \tag{3.13}$$

The main transmission of the delay line is the first transit, *i.e.* when the SAWs propagate once through the delay line and $n_t = 1$.

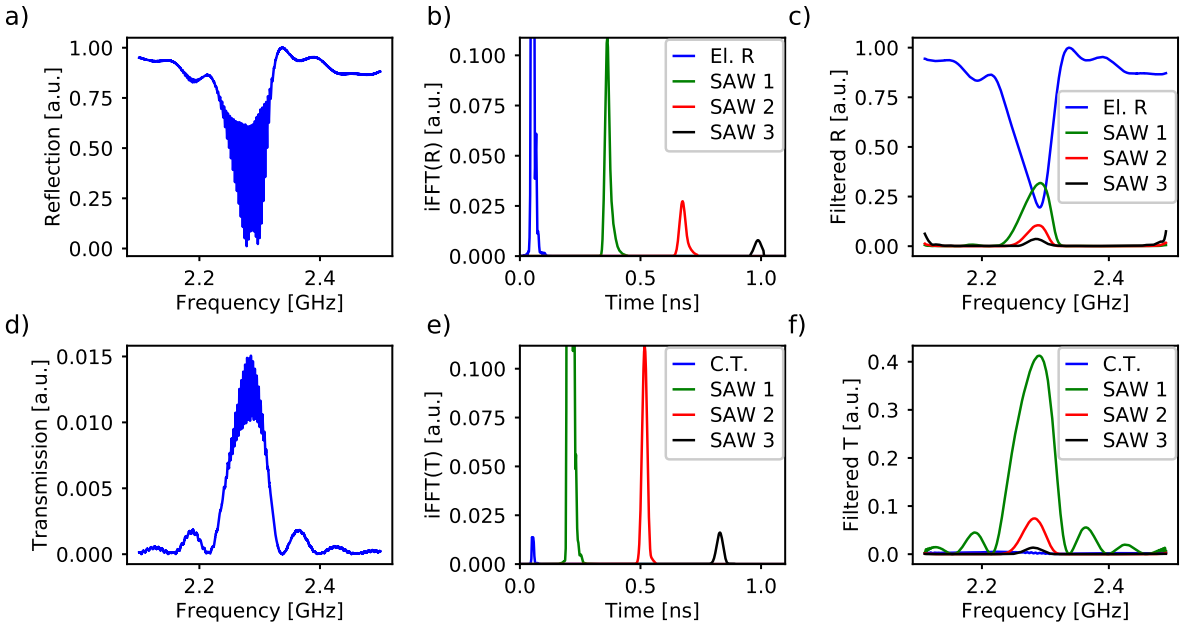

Figure 3.4: Measured a) transmission and d) reflection in the frequency domain of a delay line with two identical double electrode IDTs (IDT_1 in the appended Paper III). The inverse Fourier transform of b) the transmission and e) the reflection into the time domain show peaks separated in time. The separation in time correspond to the time delay between the electric signals and SAWs transiting the delay line a certain number of times. Filtering certain peaks and Fourier transforming back to the frequency domain, certain parts of the c) the transmission and f) the reflection can be obtained.

3.4.1 Inverse Fourier filtering

Usually only the main acoustic reflection and main transmission is of interest. Thus, it is useful to filter out the interference from multiple transiting SAWs and this can be done using inverse Fourier filtering, which will be described in this section.

A signal can be converted from its original domain, which commonly is time, to a representation in the frequency domain. This decomposition can be done using the Fourier transform and the inverse (from frequency to time) can be done using the inverse Fourier transform. Performing linear operations in the time domain have corresponding operations in the frequency domain, which might be easier to perform. Thus, it is sometimes preferable to Fourier transform the signal from the time domain to the frequency domain, and perform the operations in the frequency domain. After the desired operations are performed, the result can be inverse Fourier transformed back to the time domain.

The procedure of inverse Fourier filtering is shown in Figure 3.4 for a simultaneous measurement of reflection and transmission in the frequency domain of a delay line with two identical double electrode IDTs (IDT_1 in the appended Paper III). The measured reflection and transmission show interference effects (ripples) due to multiple transiting SAWs (Figure 3.4a) and d)) and these appear as separate peaks in the inverse Fourier transform into time (Figure 3.4b) and e)). In Figure 3.4b) the peaks correspond to

the electric reflection (S_{33}, blue) and SAWs transiting the delay line back and forth one (green), two (red) or three times (black). Similarly the peaks in Figure 3.4e) correspond to the electric crosstalk between the IDTs (blue), and SAWs transiting the delay line back and forth one (green), two (red) or three times (black). The magnitude of the peaks (normalized to the highest peak) represents the amount of that part of the signal present in the original signal. By choosing certain peaks and Fourier filtering back to the frequency domain, the information of that part of the signal can be obtained (see Figure 3.4c) and f)). For instance, the ripples in the reflection in Figure 3.4a) are removed from the electric reflection in Figure 3.4c), by filtering out the multiple transiting SAWs. Similarly, the ripples in the transmission in Figure 3.4d) are removed from the main transmission in Figure 3.4f), by filtering out the electric crosstalk and SAWs transiting the delay line more than once.

3.5 Floating electrode unidirectional transducer

When SAWs are used to carry quantum information, it is important to have low losses and efficient electric/SAW conversion. The conversion in the IDTs in Section 3.3 is symmetric for both acoustic ports, and hence 50 % of the acoustic power is lost in the wrong direction. In this section, we focus on directing the SAWs into one desired port to improve the electric/SAW conversion.

Unlike the symmetric IDT, a unidirectional transducer (UDT) [3, 111] can be optimized to release most of its SAW energy in one preferred direction. This can be done by maximizing the scattering element S_{13} while minimizing S_{23} in Eq. (3.7) in Section 3.2.1. UDTs have previously been studied for classical applications, such as low-loss SAW filters at room temperature [2, 3]. Since they have complicated structures, a substantial effort has been made in engineering low loss UDTs at gigahertz frequencies [112]. Various types of UDTs have been tested for different piezoelectric substrates. On strong piezoelectric materials, such as lithium niobate, the preferred UDT types utilize piezoelectric reflections, because these reflections dominate over mechanical reflections.

Here we focus on one type of UDT utilizing piezoelectric reflections [149], which is based on a floating electrode unidirectional transducer (FEUDT) [150] (Figure 3.5). It consists of a periodic structure, where a unit cell has six electrodes with the same width and electrode separation. Each unit cell has one electrode connected to the live upper bus, one electrode connected to the lower grounded bus and four floating electrodes, two of which are connected to each other. The design is such that electric/SAW conversion is optimized for port 1 and minimized for port 2.

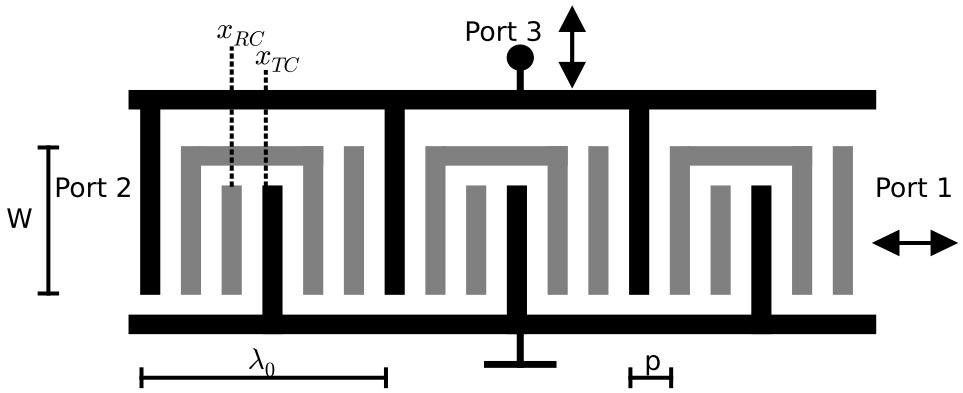

Figure 3.5: A FEUDT with six electrodes in one unit cell. Each unit cell has a transduction center x_{TC} which is separate from its reflection center x_{RC}. The preferred electric/SAW conversion is towards the right [150], in port 1. The upper bus is connected to live electrodes, the lower bus is grounded and two of the floating electrodes (gray) are connected to each other. The length of one unit cell is λ_0 and the overlap of the electrodes is W. All electrodes have the same finger width a, which is equal to the separation between them, and has a pitch $p = 2a$, such that $a = \lambda_0/12$.

The ratio between the power converted to port 1 and 2, defines the directivity of the FEUDT. The directivity of each unit cell can be illustrated by a spatially separated center of transduction x_{TC}, where the SAWs are regarded to be generated, and a center of reflection x_{RC}, where the SAWs are regarded to be reflected. Both centers, shown in Figure 3.5, can be found by the Coupling of Mode theory in the following section. The spatial separation of these centers, results in constructively and destructively interfering SAWs in the direction of port 1 and port 2, respectively.

3.5.1 Coupling of modes

To describe transducers that are more complicated than the double electrode IDT, such as FEUDTs, internal mechanical reflections need to be considered. Here, this is done with the coupling of modes (COM) theory [3, 151–155], which involves coupling between waves propagating in the same or opposite directions and a distributed transduction. This method does not include bulk waves, diffraction nor beam steering. The resistivity of the electrodes and buses are also ignored, which is an accurate assumption for our superconducting circuits. In the derivation of the COM equations, it is also assumed that reflection and transduction of the transducer can be treated separately and then added. The current in the transducer is calculated for a shorted transducer ($V = 0$) for left and right propagating waves, and the contribution from the capacitance when $V \neq 0$ is added to that solution. First COM will be described for a general periodic transducer and then the COM parameters for a FEUDT will be found from a quasi-static approximation.

Following Morgan [3], we consider left propagating waves with amplitude $b(x)$, and right propagating waves with amplitude $c(x)$ (Figure 3.6). Using the wavenumber at

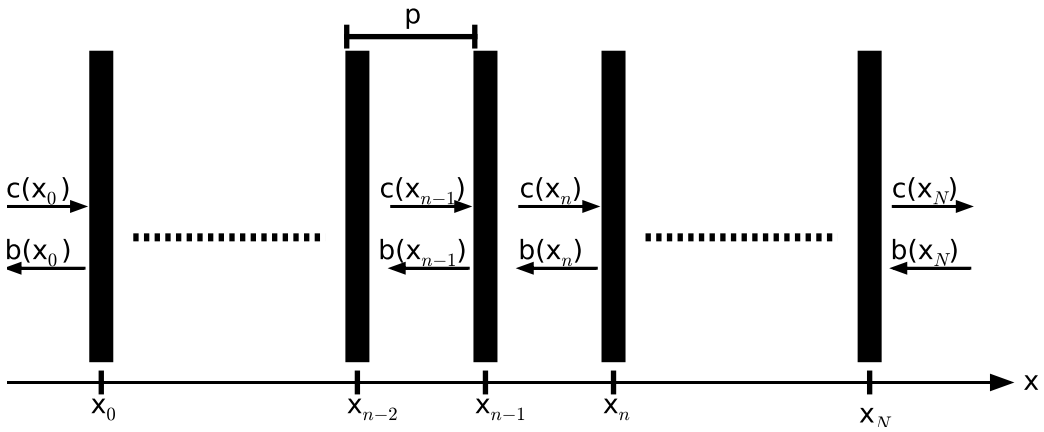

Figure 3.6: SAW amplitudes $b(x)$ and $c(x)$ propagating towards the left and right, respectively, in a transducer with N electrodes.

the center frequency k_0, slowly varying amplitudes can be defined as $B(x) = b(x)e^{-jk_0x}$ and $C(x) = c(x)e^{jk_0x}$ such that the power of the waves are $|B(x)|^2/2$ and $|C(x)|^2/2$. A periodic transducer can then be described with the differential equations:

$$\frac{d}{dx}\begin{pmatrix}C(x)\\B(x)\end{pmatrix} + \begin{pmatrix}j\delta & -\kappa\\ -\kappa^* & -j\delta\end{pmatrix}\begin{pmatrix}C(x)\\B(x)\end{pmatrix} = V\begin{pmatrix}\alpha\\ \alpha^*\end{pmatrix} \tag{3.14a}$$

$$\frac{d}{dx}I(x) = 2\alpha^* C(x) - 2\alpha B(x) + j\omega C_l V, \tag{3.14b}$$

where $\delta \equiv k - k_0$ is the detuning from the wavenumber at the center frequency, κ is a reflection parameter per unit length, α is a transduction parameter per unit length and C_l is the capacitance per unit length. Eq. (3.14a) described the change in a SAW over a unit distance by combining reflected, transmitted and transduced waves. The solution is the sum of the complementary solution for $V = 0$ (shorted IDT), and the particular solution for $V \neq 0$. The matrix has eigenvalues $\pm js$, where $s^2 = \delta^2 - |\kappa|^2$, such that $B(x)$ and $C(x)$ are proportional to e^{jsx}. At frequencies close to the center frequency $|\delta| < |\kappa|$, s is imaginary and the complete solution to Eq. (3.14a) is

$$C(x) = h_1 e^{-jsx} + h_2 e^{jsx} + K_1 V, \tag{3.15a}$$

$$B(x) = h_1 p_1 e^{-jsx} + h_2 p_2 e^{jsx} + K_2 V. \tag{3.15b}$$

h_1 and h_2 are constants dependent on the boundary conditions;

$$p_1 = j(\delta - s)/\kappa \tag{3.16a}$$

$$p_2 = j(\delta + s)/\kappa \tag{3.16b}$$

$$K_1 = (\alpha^*\kappa - j\delta\alpha)/s^2 \tag{3.16c}$$

$$K_2 = (\alpha\kappa^* + j\delta\alpha^*)/s^2. \tag{3.16d}$$

Using the boundary conditions in Eq. (3.16) for the solution in Eq. (3.15), the elements

in the P-matrix in Eq. (3.8) in Section 3.2.1 can be determined to be

$$P_{11} = \frac{-\kappa^* \sin(sN_p\lambda_0)}{s\cos(sN_p\lambda_0) + j\delta\sin(sN_p\lambda_0)} \tag{3.17a}$$

$$P_{12} = P_{21} = \frac{se^{-jk_0N_p\lambda_0}}{s\cos(sN_p\lambda_0) + j\delta\sin(sN_p\lambda_0)} \tag{3.17b}$$

$$P_{22} = \frac{\kappa\sin(sN_p\lambda_0)e^{-2jk_0N_p\lambda_0}}{s\cos(sN_p\lambda_0) + j\delta\sin(sN_p\lambda_0)} \tag{3.17c}$$

$$P_{31} = -2P_{13} = \frac{2\alpha^*\sin(sN_p\lambda_0) - 2sK_2(\cos(sN_p\lambda_0) - 1)}{s\cos(sN_p\lambda_0) + j\delta\sin(sN_p\lambda_0)} \tag{3.17d}$$

$$P_{32} = -2P_{23} = e^{-jk_0N_p\lambda_0}\frac{-2\alpha\sin(sN_p\lambda_0) - 2sK_1(\cos(sN_p\lambda_0) - 1)}{s\cos(sN_p\lambda_0) + j\delta\sin(sN_p\lambda_0)} \tag{3.17e}$$

$$P_{33} = -K_1P_{31} - K_2P_{31}e^{jk_0N_p\lambda_0} + 2(\alpha^*K_1 - \alpha K_2)N_p\lambda_0 + j\omega C_lN_p\lambda_0, \tag{3.17f}$$

where $N_p\lambda_0$ is the length the transducer. The P-matrix can be converted into the S-matrix using Eq. (3.9) in Section 3.2.1, and hence, by determining κ, α and C_l the scattering parameters of the device can be described.

3.5.2 Quasi-static approximation to find COM parameters for a FEUDT

The COM parameters for a FEUDT, can be determined following the quasi-static approximation [152–154]. This is an easier approach than the comprehensive algebraic analysis in Ref. [151]. It is a simplified version of Green's function analysis, where the electrostatic and acoustic contributions are separated. It is assumed that the only waves present are non-leaky waves and that the velocity change caused by the mechanical and electrical loading are negligible. Further, the transducer is initially assumed infinitely periodic with constant electrode width and separation and each unit cell is evaluated separately. Later, this is later extended to a transducer with a finite length neglecting edge-effects.

When a voltage is applied over a FEUDT with the length of one unit cell, a SAW is emitted with a surface potential described in Section 3.3. In that section the superposition of the response from one electrode in Eq. (3.4) was approximated as a constant, but $\mathcal{F}[\rho_f](k)$ varies slowly. However, in the quasi-static approximation $\mathcal{F}[\rho_f](k)$ is used to calculate the COM capacitance, transduction and reflection parameter. For a more detailed description see my Licentiate thesis [156] and for a full derivation see Ref. [154].

The capacitance per unit length can be found from evaluating the voltages and net charges on each live electrode. These calculations are purely electrostatic and the substrate is not required to be piezoelectric. For a FEUDT with six electrodes per unit cell the capacitance per unit length is according to Ref. [154]

$$C_l = \frac{5\epsilon_\infty W}{8\lambda_0}. \tag{3.18}$$

Piezoelectricity is introduced to evaluate the transduction and reflection parameters. The transduction parameter can be found while ignoring reflections. By calculating the

waves that leave each unit cell, a reference point can be found where the waves generated in both directions have the same amplitude and phase. This reference point is called the transduction center (Figure 3.5) and it is used for obtaining the transduction parameter

$$\alpha = j\frac{A_T}{\lambda_0}\sqrt{Y_0}e^{jk_0x_{TC}}, \tag{3.19}$$

where A_T is the effective transduction strength [154].

The reflection parameter is evaluated when all electrodes (including the floating electrodes) are considered shorted. The floating electrodes are allowed to have nonzero voltages while the total net charge on the floating electrodes is zero. The calculations to obtain the voltages and the net charges is similar to the process of finding the capacitance per unit length. With the same argument as for the transduction, a reflection center x_{RC} (Figure 3.5) is found and used for obtaining the reflection parameter

$$\kappa = j\frac{A_R}{\lambda_0}e^{2jk_0x_{RC}} \tag{3.20}$$

where A_R is the effective reflection strength [154].

From the three COM parameters (C_l, α and κ) the full P-matrix can be calculated and hence the S-matrix for the FEUDT with six electrodes in one unit cell. The S-parameters for a FEUDT with 160 unit cells and 46 μm electrode overlap is shown in Figure 3.7. The maximum of S_{13} is -0.5 dB at 2.303 GHz, but at this frequency the ratio of S_{13} and S_{23} (directivity) is only 10 dB while the maximum directivity is 30 dB at 2.309 GHz. Close to the maximum of S_{13}, both S_{11} and S_{33} are low, while S_{22} is high. Reducing the acoustic reflection and maximizing the electric/SAW conversion in a transducer maximizes the performance of the resulting delay line. In this respect, the performance of the FEUDTs surpasses symmetric IDTs (Figure 3.3), for which S_{13} never exceeds -3 dB and the maximum of S_{13} coincides the maximum of S_{11}.

As can be seen in Figure 3.8 the COM model predicts that the directivity increases monotonically with number of unit cells. In order to achieve a directivity above 20 dB and impedance matching to 50 Ω, the FEUDTs require approximately 100 unit cells. In Chapter 5 and the appended Paper III, we will see that this agrees well with our measurements. The directivity is independent of electrode overlap but impedance matching needs an electrode overlap larger than 25 μm.

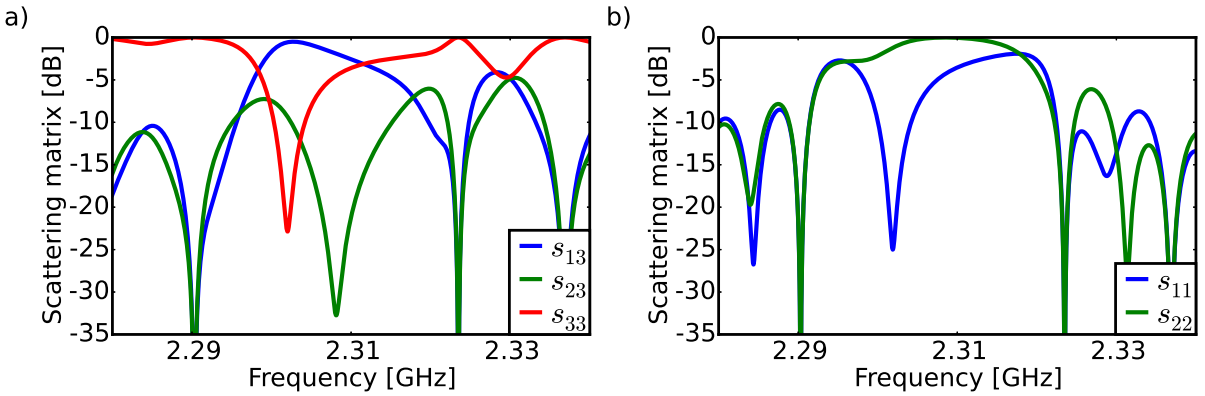

Figure 3.7: a) Scattering elements s_{13} (blue), s_{23} (green) and s_{33} (red) for a FEUDT with 160 unit cells and 46 μm electrode overlap. Both the electric reflection and the maximum directivity are offset the maximum transduction. b) Acoustic reflection scattering elements for both ports, where s_{22} (blue) is higher than s_{11} (green) and the dip in s_{11} coincides with the reflection dip in s_{33}.

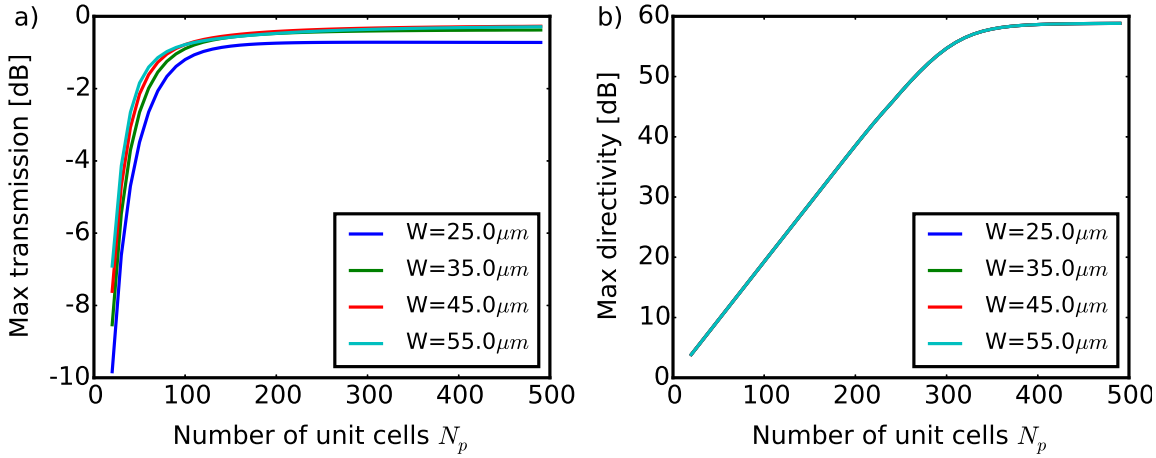

Figure 3.8: a) Maximum transmission versus number of unit cells N_p for a FEUDTs with different electrode overlaps W. At least 100 unit cells are needed to impedance match to 50 Ω. b) Maximum directivity versus N_p for FEUDTs. For a directivity above 20 dB, more than 100 unit cells are needed. The directivity does not depend on W.

3.6 Artificial atom coupled to surface acoustic waves

SAWs were treated purely classically in the previous sections. In this section, we discuss how SAWs are interacting with a superconducting artificial atom (described in Chapter 2.2) and the interaction will be treated semi-classically following the appended Papers I and II.

An artificial atom has discrete energy states spaced non-equidistantly. They are commonly used in superconducting circuits to explore fundamental phenomena in quantum physics [8, 125]. In these circuits, the transition frequencies between the energy states in the artificial atoms are typically designed to be in the microwave range. In the appended Papers I and II, the artificial atom in the superconducting circuit is not only interacting with electromagnetic microwaves but is even more strongly coupled to propagating SAWs.

To design an artificial atom to couple to SAWs, the similarities between the IDT electrode structure and the shunt capacitance used in transmons [37] can be exploited. In this thesis we will use the term QDT (qubit coupled IDT) to describe the IDT used as the capacitive part of the transmon. In the transmon (described in Chapter 2.2.2), the large capacitance shunts a Superconducting Quantum Interference Device (SQUID) described in Chapter 2.1.3. This SQUID is a superconducting loop interrupted with two weak barriers, which separates the loop into two islands. One island is connected to an electrode on the top bus of the QDT and the other island is connected to the bottom grounded bus (Figure 3.9a).

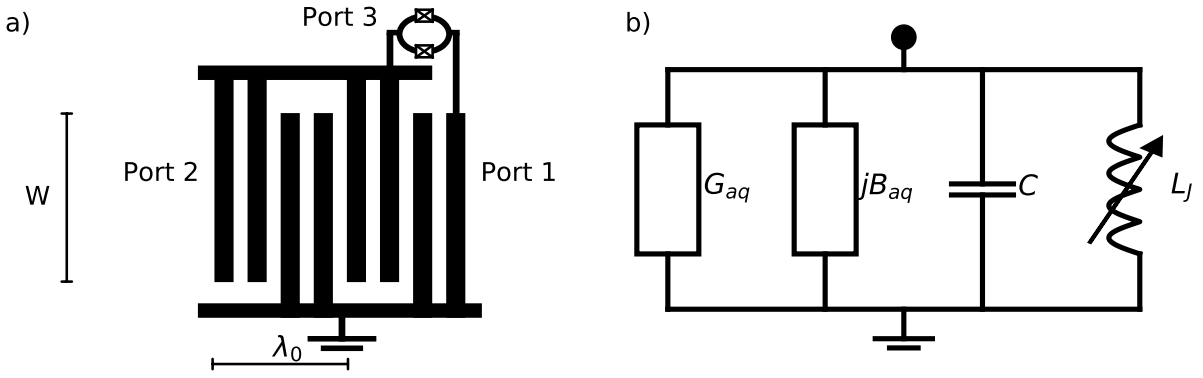

Figure 3.9: a) A transmon coupled to SAW through a double electrode IDT as its shunt capacitance. The top bus of the QDT is connected to one of the islands in the SQUID and the bottom grounded bus is connected to the other island. b) Circuit model of an artificial atom coupled to SAWs. The SQUID is treated as a tunable nonlinear inductor in parallel to the equivalent circuit of the QDT in Figure 3.3b.

The artificial atom is treated as a two-level system, which is valid for energies low enough to never excite the artificial atom beyond the first excited energy state. At these levels, the artificial atom can be called a quantum-bit (qubit) coupling to SAWs.

The equivalent circuit of the transmon can be obtained treating the SQUID as a tunable inductor and adding it in parallel to the equivalent circuit of the QDT described in Section 3.3.1. The equivalent circuit of the transmon, illustrated in Figure 3.9b, has

a total admittance of $Y_{\mathrm{Q}}(\omega) = G_{aq} + jB_{aq} + j\omega C + 1/(j\omega L_J)$, where L_J is the tunable inductance described in Eq. (2.28). G_{aq} and B_{aq} describe the QDT structure and C is the total capacitance of the transmon. They can be calculated according to Eq. (3.10).

As described in Chapter 2.2.2, the transmon transition frequencies $f_{m+1,m}(\Phi_{\mathrm{ext}})$ are given by Eq. (2.38) where the Josephson energy is given by Eq. (2.27) and the charging energy is described in Chapter 2.2.1 with the capacitance set by the QDT. In addition, the transmon coupled to SAWs has an acoustic resonance frequency; the center frequency of the QDT, f_{QDT} (see Chapter 3.2). While $f_{m+1,m}(\Phi_{\mathrm{ext}})$ can be tuned by adjusting $L_J(\Phi_{\mathrm{ext}})$, f_{QDT} is defined by design of the QDT electrode structure. Consequently the external magnetic flux can be used to tune the transition frequencies of the transmon in and out of resonance with the center frequency of the QDT, and hence change how the transmon to interacts with SAWs.

There are three main characteristics that are important to consider for the transmon design: the anharmonicity, the coupling strength to the SAW and the coupling bandwidth. The anharmonicity is a measure of the nonlinearity of the artificial atom and describes how much the transition frequencies from the higher levels deviates from the fundamental resonance frequency. Generally the anharmonicity for transmons is close to $-E_C$ (see Eq. (2.37)), but when it is coupled to SAW it is also affected by a Lamb shift of the size of $-B_{aq}(\omega)/(2\pi C)$ originating from the QDT. For a drive close to the center frequency of the QDT, the Lamb shift is very small since B_a is close to zero (see Eq. (3.10)). This Lamb shift is briefly discussed in the supplementary material of the appended Paper I and in the appended Paper II, and is further explained in Refs. [96, 147].

The anharmonicity needs to be bigger than the relaxation rate to facilitate treatment of the transmon as a two-level system. The relaxation rate is the rate at which energy stored in the transmon converts into SAWs by relaxation, dissipating power into the real part of the admittance. It is set by the QDT's coupling strength to SAWs and can be expressed as

$$\Gamma_{\mathrm{ac}}(\omega) = \frac{G_a(\omega)}{2C_T}, \tag{3.21}$$

with G_a and C_T from Eq. (3.10a,c). The maximum coupling for a certain energy transition of the transmon (for instance the 0-1 energy transition) occurs at coinciding acoustic and electric resonance. Then $\omega_{\mathrm{QDT}} = \omega_{10} = 2\pi/\sqrt{L_J C_T}$, where

$$\Gamma_{\mathrm{ac}} = \frac{G_{a0}}{2C_T} \approx 0.5 \cdot \omega_{\mathrm{QDT}} K^2 N_p \tag{3.22}$$

for a transmon with a double electrode QDT. The coupling bandwidth of the QDT can be approximated as $0.9 f_{\mathrm{QDT}}/N_P$ (same as for the double electrode IDT in Chapter 3.3.1). If the coupling bandwidth is broad, the transmon can be excited using signals further away from the center frequency. If the coupling bandwidth is narrow, the signals have to be closer to resonance with the center frequency of the QDT to excite the transmon. Note that the coupling is proportional to N_p, while the anharmonicity and the coupling bandwidth are inversely proportional to N_p. This needs to be considered when a transmon is designed for SAW experiments, such as in the appended Paper I.

3.6.1 Interaction with a propagating SAW field

A transmon coupling to a propagating SAW field can be described in a similar way as in Chapter 2.3.3. We assume that the transmon can be treated as a two-level system (qubit) since the anharmonicity is sufficient and the frequency ($f_p = 2\pi\omega_p$) of the interacting field is close to the transition frequency ($f_{10} = 2\pi\omega_{10}$) between the two lowest energy levels of the transmon. However, now the interacting field is a propagating SAW field produced by applying a voltage over a classical IDT (described in Chapter 3.3) close to the IDT's center frequency and the transmission line corresponds to the surface of the piezoelectric substrate.

By assuming that the propagating SAW field is reflected in a similar way as the electromagnetic field in Chapter 2.3.3, the voltage reflection and transmission coefficients of the qubit are obtained from Eq. (2.63) and Eq. (2.65), respectively. The relaxation rate from state $|1\rangle$ to $|0\rangle$ of the qubit $\Gamma_{10} \approx \Gamma_{ac}(\omega)$. The frequency dependence of the acoustic relaxation rate follows Eq. (3.21) and the 0-1 decoherence rate $\gamma_{10} = \Gamma_{10}/2 + \Gamma_\phi$ for Γ_ϕ as the 0-1 pure dephasing rate, which is described in Chapter 2.3.3.

Both the reflection and transmission coefficients depend on the average number of incoming phonons, which is more difficult to calculate than the average number of incoming photons. The average number of incoming phonons (or photons) is proportional to the power of the incoming field. The incoming SAW field is emitted by an IDT and unless the electric/SAW conversion can be measured or calculated it is difficult to determine how much of the power of the applied voltage is converted into SAW power and how much of this reaches the transmon. Thus, the average number of phonons reaching the transmon cannot easily be determined and $\Omega_p = k\sqrt{P}$ is used in Eq. (2.63) and Eq. (2.65) with k as a proportional parameter to be fitted.

The reflected SAW field is detected by the classical IDT used to produce the incoming SAW field and the transmitted SAW field can be detected by adding another classical IDT on the opposite side of the transmon, see Figure 1a in the appended Paper IV. Assuming that the two classical IDTs are identical, the reflection and transmission measured at the IDTs are described by

$$r = S_{33} + S_{13}^2 S_{q11} e^{-j2kL} + \mathcal{O} \tag{3.23a}$$

$$t = S_{13}^2 S_{q12} e^{-jkL} + \mathcal{O}, \tag{3.23b}$$

where S_{q11} is the reflected SAW field off the qubit described in Eq. (2.63) and S_{q12} is the transmitted SAW field off the qubit described in Eq. (2.65). The phase kL that the SAWs pick up while propagating the distance L between the qubit and an IDT is mentioned in Chapter 3.4 and the scattering elements S_{33} and S_{13} are found in Eq. (3.7). The electrical reflection (S_{33}) and multiple SAW transits ($\mathcal{O}$) can be filtered out if the distance between the two IDTs and the qubit is sufficiently large and if the bandwidth of the IDTs is wide enough, as described in Chapter 3.4.1.

The qubit can also be excited electrically by using a capacitively coupled gate. Since the qubit is designed to couple to SAWs, it will emit SAWs when relaxing if it is tuned on resonance with ω_{QDT}. This emission can be measured using an IDT at a distance L

from the qubit and it can be expressed as

$$t_E = S_{q31} S_{13} e^{-jkL}, \tag{3.24}$$

where S_{q31} is the acoustic scattering element for emission from an electrically excited qubit. The scattering elements of the qubit are power dependent and decrease for increasing excitation power, thus the expressions the following are only valid for low enough powers such that the artificial atom is far from saturation.

Sometimes it is not possible to filter multiple transits out, for instance if a single electrode IDT is used to measure the emission off the qubit. Then its narrow bandwidth, due to internal mechanical reflections, limits the frequency over which the measurement can be performed. Let us assume one single electrode IDT at a distance L from the qubit and that we apply a signal to emit SAWs with the IDT. Then the multiple transits in Eq. (3.23a) cannot be filtered out and the measured reflection at the IDT is

$$r = S_{33} + \frac{S_{13}^2}{S_{11}} \sum_{n_t=1}^{\infty} \left(S_{11} S_{q11} e^{-j2kL} \right)^{n_t} = S_{33} + \frac{S_{13}^2 S_{q11} e^{-j2kL}}{1 - S_{11} S_{q11} e^{-j2kL}}, \tag{3.25}$$

where the summation is evaluated using the geometric series. Similarly, we can assume that the qubit is electrically excited via the capacitively coupled gate. Then the signal measured at the IDT is described by

$$t_E = \frac{S_{q31} S_{13} e^{-kL}}{1 - S_{11} S_{q11} e^{-j2kL}}. \tag{3.26}$$

A derivation of S_{q11} and S_{q31} can be found in the supplementary material of appended Paper I for the coinciding acoustic and electric angular resonance frequency of the qubit $\omega_{\mathrm{QDT}} = \omega_{10}$. To approximate S_{q11} from Eq. (2.63) using multiple SAW transits, we look at the system when the qubit is excited by the IDT. The number of phonons converted per second in the IDT from electrical power is $N_{\mathrm{in}} = P_{\mathrm{in}} |S_{13}|^2 / (hf)$ and the squared Rabi frequency $\Omega^2 = 4 N_{in} \Gamma_{ac}$. Since part of the phonons can be reflected by the qubit, they can transit between the qubit and the IDT multiple times and the total number of phonons reaching the qubit is approximately

$$N_{\mathrm{in,IDT}} \approx \frac{P_{\mathrm{in}}}{\hbar\omega} \left| S_{13} \sum_{n_t=0}^{\infty} (S_{11} S_{q11} e^{2jkL})^{n_t} \right|^2 = \frac{P_{\mathrm{in}}}{\hbar\omega} \left| \frac{S_{13}}{1 - S_{11} S_{q11} \exp(2jkL)} \right|^2. \tag{3.27}$$

To approximate S_{q31}, the qubit is assumed driven via the electric gate and the squared Rabi frequency $\Omega^2 = 4 N_{in} \Gamma_{el}$ with the electric coupling rate Γ_{el} between the qubit and the gate. The total number of phonons and photons reaching the qubit is approximately

$$N_{\mathrm{in,q}} \approx \frac{P_{\mathrm{in}}}{\hbar\omega} \left(1 + \left| S_{q13} S_{11} \sum_{n_t=0}^{\infty} (S_{11} S_{q11} e^{2jkL})^{n_t} \right|^2 \right) = \frac{P_{\mathrm{in}}}{\hbar\omega} \left(1 + \left| \frac{S_{q13} S_{11}}{1 - S_{11} S_{q11} \exp(2jkL)} \right|^2 \right). \tag{3.28}$$

The Rabi frequency and number of incoming quanta is inserted into Eq. (2.63) for either case (drive through IDT or gate), using $\Gamma_{10} = \Gamma_{\mathrm{ac}} + \Gamma_{\mathrm{el}}$ to obtain the scattering parameters for the qubit when multiple transits cannot be filtered out.

Chapter 4

Experimental techniques

In order to perform the experiments, nanofabrication and precise measurements were done. In the first section of this chapter, the key processes used in the fabrication of the samples are described. The second section describes the measurement techniques, where the samples are cooled down to cryogenic temperatures in a dilution cryostat and measured at gigahertz frequencies.

4.1 Sample fabrication

All devices presented in this thesis were fabricated in the class 10-100 area of the MC2 Nanofabrication Laboratory at Chalmers University of Technology. They were SAW devices designed with IDTs (see Chapter 3.3) or FEUDTs (see Chapter 3.5.2) and an artificial atom (see Chapter 3.6) placed on a piezoelectric substrate. The piezoelectric substrate was either gallium arsenide (GaAs-(100)-[011]) or black lithium niobate ($LiNbO_3$-YZ). An example of a device can be seen in Figure 4.1a). Regardless of the transducer type used, single or double electrode IDTs, FEUDTs or QDTs embedded in artificial atoms (Chapter 3), they were made with 27 nm thick aluminum, capped with 3 nm palladium (see blue overlay in Figure 4.1a)) and connected to 85 nm think gold ground planes and electrodes (see brown overlay in Figure 4.1a)). The gold ground planes had a sticking layer of 5 nm titanium and were capped with a 10 nm layer of palladium for better contact. This resulted in a total pad thickness of 100 nm. The QDTs were in addition connected to aluminum SQUIDs (see Figure 4.1b)), which were deposited in a separate fabrication step using two-angle evaporation (see green overlay in Figure 4.1a)) and connected via the palladium layer on the transducers.

The fabrication techniques used are described briefly below, for more details the fabrication recipes can be found in Appendix A.

4.1.1 Photolithography for microscale features

In order to save processing time, photolithography was used to define features bigger than approximately 1 μm, which in our devices were contact pads, ground planes and alignment marks for later fabrication steps.

Prior to the photolithography, the cleaned substrate was coated with a bilayer of a lift-off resist and a positive photoresist. The two layers of resist had different properties and purposes; the top layer was used for patterning since it acquires sharp edges with high

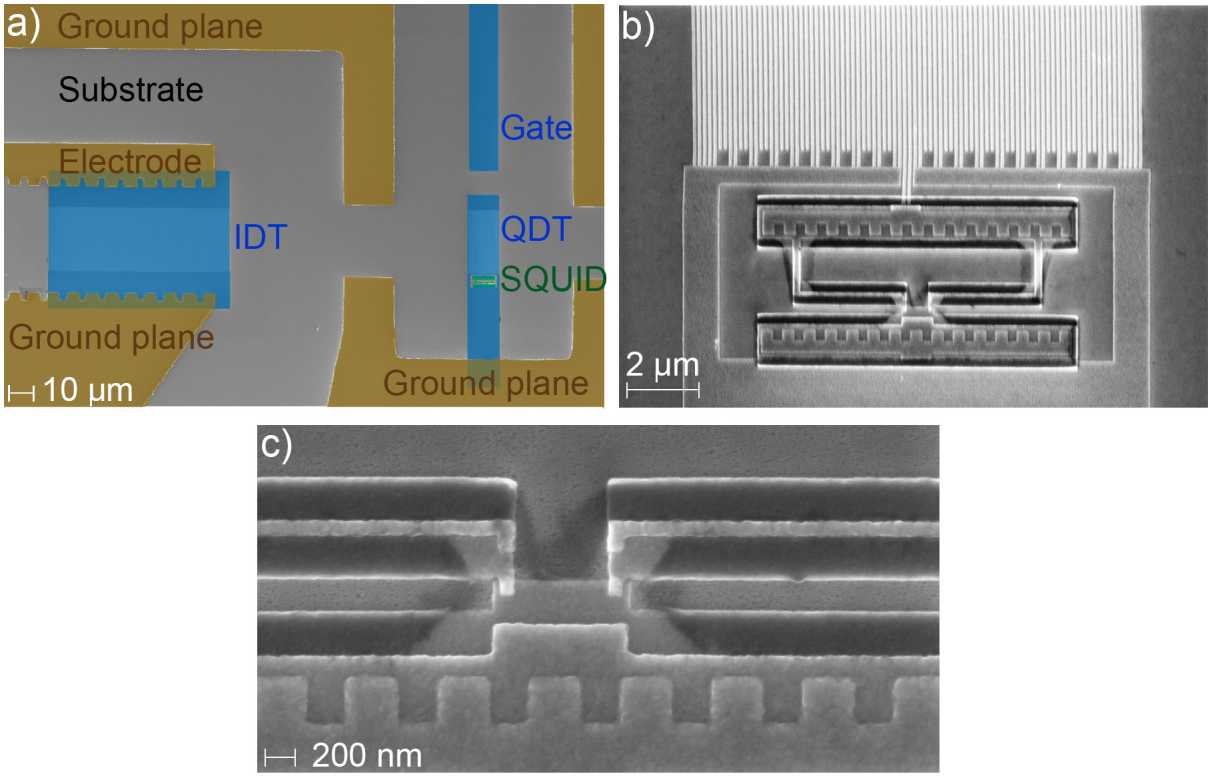

Figure 4.1: a) Image of part of a device using scanning electron microscopy with a magnification of 1500 times. The brown overlay highlights the gold ground planes and electrodes. The blue overlay highlights the aluminum transducers and connections and the green overlay highlights the SQUID. b) Image of the SQUID, using scanning electron microscopy with 22 000 times magnification. The top island of the SQUID is connected via two QDT electrodes to the top bus bar of the QDT and the bottom island is connected to ground. The ground surrounds the SQUID and also serves as the grounded bottom bus bar of the QDT. c) Image of two Josephson junctions in a SQUID and the connection of the SQUID to the ground plane. The image is taken using 79 000 times magnification with scanning electron microscopy.

resolution, while the bottom layer improved the lift-off because it dissolves isotropically forming an undercut.

The photolithography was performed by first aligning the coated substrate carefully with a chromium pattered photomask and then exposing it to ultraviolet light through the photomask. The exposed coated substrate was immersed into a hydroxide solution for development. During the development, the exposed resist was dissolved while the resist that had been protected from the exposure by the photomask was left on the substrate. In this way, the negative pattern of the photomask was transferred onto the resist on the substrate.

After the development, the organic residues from the exposed resist were ashed away in an oxygen plasma. The desired metal was then deposited on the pattered substrate in an electron-beam evaporator with high vacuum. Finally, the remaining resist was dissolved in a solvent, which lifted-off the metal on top of the resist and left the patterned metal.

For a better flexibility of the pattern, contact pads and ground planes were in some cases written with a LASER writer instead of photolithography. In this process, a LASER scans the resist-coated substrate in a similar way to the electron-beam that will be described in the following section.

4.1.2 Electron-beam lithography for micro- and nanoscale features

The smaller features of the devices, such as transducers and SQUIDs (Chapter 3.6), required higher resolution than possible with LASER and photolithography, necessitating the use of electron-beam lithography. In electron-beam lithography, a focused beam of electrons scans the substrate coated with electron-sensitive resist according to a programmable pattern. Since no mask is needed, the design is more flexible but the patterning is much slower. Otherwise, the electron-beam lithography steps are similar to the photolithography steps.

There are some difficulties associated with electron-beam lithography, including proximity and charging errors. The proximity effect limits the achievable resolution and is common when exposing narrow and dense patterns such as the transducers. The effect occurs when electrons scatter from the exposed areas to regions in the proximity and partially expose the unwanted areas. However, the proximity effect can be compensated for by calculating the dose profile for the substrate, divide the pattern into a mesh grid and distribute the doses according to the profile. This was done using the software BEAMER^{TM}.

Charging errors are minor on conducting or semi-insulating substrates such as gallium arsenide, but are usual on insulating substrates such as lithium niobate. On insulating substrates, electrons are not conducted away when the electron-beam scans the substrate. This leads to build up charge repelling beam electrons from the region, which can result in a small offset and a distorted pattern. Therefore, a thin conducting resist layer was used on top of the electron-sensitive resists on the lithium niobate substrates.

4.1.3 Two-angle evaporation for superconducting quantum interference devices

Some of the devices, those containing artificial atoms, went through additional fabrication steps where the QDT was connected to a SQUID (see Figure 4.1b)). The SQUID was made using electron-beam lithography to create a suspended resist (Dolan) bridge and a technique called two-angle evaporation (shadow evaporation) [157].

This technique was used after all other structures such as ground planes and transducers had been made, and the sample had been coated once again with electron-beam resist, patterned by electron-beam lithography and developed. The sample was mounted onto a tilting stage in an electron-beam evaporator. First, the stage was tilted to a fixed angle at which the bottom aluminum layer was evaporated. Second, the aluminum-covered substrate was exposed to pure oxygen gas at a regulated pressure for a certain amount of time, which formed a thin insulating barrier of amorphous aluminum oxide. Finally, after the oxygen was pumped out, the top aluminum electrode was deposited at the opposite angle. The metal was lifted-off, and the desired pattern was left on the substrate as described in the previous sections.

The thicknesses of the deposited aluminum were chosen such that the top layer was thicker and overlapped the bottom layer with the insulating barrier in between. In addition, one aluminum layer contacted the grounded part of the transducer and the other layer contacted the live part (see Figure 4.1b,c) and Figure 5.1b in Chapter 5.1) such that the SQUID was coupled in parallel with the transducer. This connection was possible using the thin palladium layer on top of the aluminum electrodes in the QDT, which prevented the formation of aluminum oxide.

4.2 Cryogenic measurements

The aluminum IDTs, FEUDTs and artificial atoms were superconducting below approximately 1.4 K, but they were cooled down even further for the experiments. When conducting experiments at the quantum level, it is necessary to cool down to cryogenic temperatures and operate at microwave frequencies such that $k_B T \ll hf$. Therefore the sample in the appended Paper I and II, which was measured at a base temperature of 20 mK in a wet dilution cryostat, was operated at frequency of 4.8 GHz. The FEUDT structure in the appended Paper III was more complicated and needed more electrodes within one period, which reduced the size of the electrode width and made the fabrication a lot more problematic. The problem was somewhat reduced by operating at 2.3 GHz. For those measurements, we used a dry dilution cryostat to cool down to 10 mK. The same dry dilution cryostat was used for measurements performed in Paper IV and V.

4.2.1 Cooling techniques

The cooling process in both the wet and the dry dilution cryostat takes place in a mixing chamber and is based on the phase separation occurring when a mixture of helium-3 (^{3}He) and helium-4 (^{4}He) is cooled down to temperatures below 0.8 K. The two phases have different concentrations of ^{3}He; a ^{3}He rich phase (concentrated phase) and a ^{3}He poor phase (diluted phase). Since ^{3}He is lighter than ^{4}He, the concentrated phase accumulates on top of the diluted phase. When ^{3}He transits from the concentrated phase to the diluted phase across the phase boundary, heat is absorbed and this provides cooling of the mixing chamber.

As long as the concentration balance of ^{3}He in the two phases is in non-equilibrium, the ^{3}He transits from the concentrated phase to the dilute phase and provides cooling. This non-equilibrium is driven by pumping ^{3}He out of the dilute phase by distillation in the still, which is connected to the diluted phase in the mixing chamber. The still is heated and the ^{3}He evaporates from the still whereas very little ^{4}He is evaporated. This is due to the much larger vapor pressure of ^{3}He than ^{4}He at the still temperature (0.7 - 0.8 K).

The ^{3}He in the concentrated phase needs to be replaced continuously. This is done by pumping out the evaporated ^{3}He from the still and returning it to the mixing chamber via a set of heat exchangers. At the still, a flow impedance ensures a high enough ^{3}He pressure for condensing. The cooling of the ^{3}He gas is done with different techniques in the wet and the dry dilution cryostat.

In the wet dilution cryostat, the dilution unit is isolated from a surrounding ^{4}He bath by an inner vacuum chamber (IVC). The surrounding ^{4}He bath is used to cool the ^{3}He before it is re-condensed in a closed volume in the 1 K-pot. The boiling point of ^{4}He is around 4 K at atmosphere and around 1.5 K when it is pumped, giving the 1 K-pot its name. The cooling power of the 1 K-pot is controlled by evaporative cooling of the ^{4}He bath funneled in from the ^{4}He bath. The flow into the 1 K-pot is adjusted by a needle valve and the evaporative cooling is achieved by pumping the ^{4}He.

After the liquid ^{3}He has been cooled by either one of the two techniques (this or the one described below), the liquid ^{3}He is further cooled by heat exchangers at the different temperature stages, before it reaches the concentrated phase in the mixing chamber.

In a dry dilution cryostat, the cooling of the ^{3}He gas is instead done with a pulse-tube cryocooler. It consists of several parts, three heat exchangers, a re-generator, a thermally isolated tube (pulse tube), a flow resistance and a buffer tank. A rotating valve oscillates the pressure at the warm side of the re-generator by connecting the system alternatingly to the high- or low-pressure side of a compressor. As a result, gas enters the system via the heat exchangers and moves inside the re-generator and pulse tube, before it is released again with a different temperature. When the gas moves inside the pulse tube, its temperature is changed by changing the pressure. One of the heat exchangers (connecting the re-generator to the pulse tube) is positioned at low temperature, where it absorbs heat from the gas and this performs cooling. A more detailed description on how a pulse tube cryocoler operates is described in Ref. [158].

4.2.2 Measurement set-up

Before the nanofabricated samples were cooled down, they were mounted and wire-bonded in a homemade sample box with SMA connectors (see Figure 4.2a). The sample boxes were attached to a superconducting magnetic coil (see Figure 4.2b), which was connected to superconducting wires using indium and mounted at the mixing chamber stage (see Figure 4.2c).

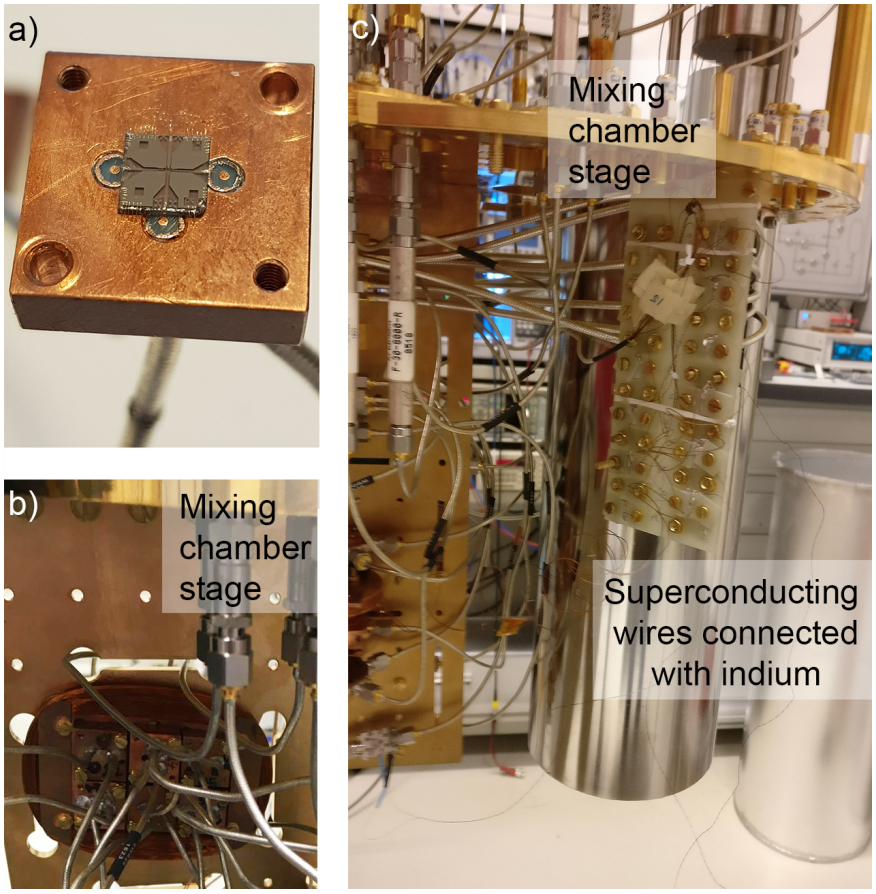

Figure 4.2: a) Sample box with a mounted and wire-bonded device. The ground planes were wire-boned to the box, while each IDT and the gate was wire-boned to the center pin of a SMA cable. One side of the transmon was wire-boned to the box for grounding. b) Six sample boxes attached to the superconducting magnetic coil, which was mounted at the mixing chamber stage. Credit for original photo: Ben Schneider c) The superconducting magnetic coil was connected to superconducting wires using indium. Credit for original photo: Andreas Bengtsson

The mixing chamber stage was kept at a temperature of either 20 mK in the wet dilution cryostat or 10 mK in the dry dilution cryostat. The set-ups in both cryostats were very similar and a typical set-up (for the dry dilution cryostat) is shown in Figure 4.3. In this set-up two types of measurements were possible; reflection (via blue and green lines) and transmission (via red and green lines).

The samples were measured via coaxial lines, which require careful design to not conduct blackbody radiation from higher temperature stages to the samples. Therefore, the coaxial lines have poor thermal conductivity and both the outer and inner conductors are thermalized at each temperature stage with an attenuator to reduce the noise temperature.

In the reflection measurements the microwave signal was sent via an ”input” line (blue in Figure 4.3), reflected off the sample back to the same circulator, where the

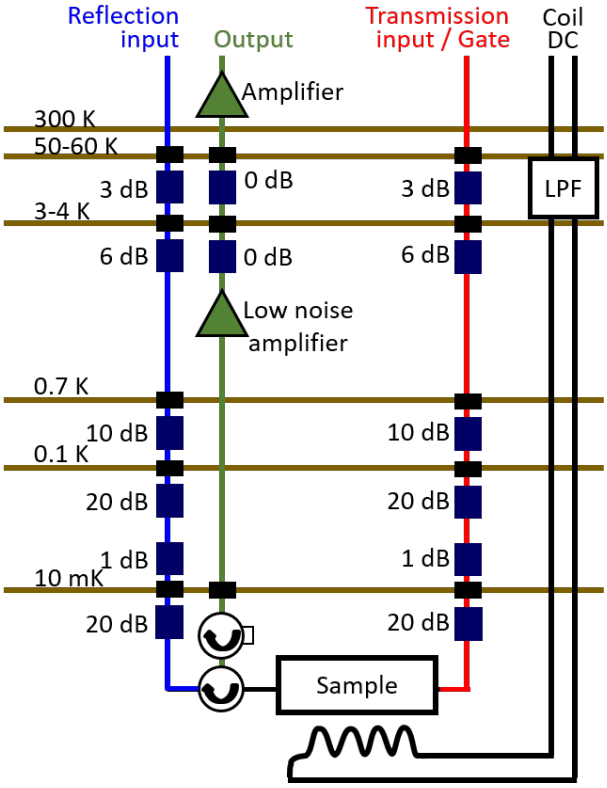

Figure 4.3: Measurement set-up enabling reflection and transmission measurements. Microwave signals were sent down an "reflection input" (blue) or a "transmission input/gate" (red) coaxial line, attenuated at every temperature stage before it reached the sample. The signal response of the sample passed two circulators (one working as an isolator) to the "output" line (green), where it was amplified first with a cryogenic low noise amplifier and then at room temperature before reaching the measurement equipment.

incoming and outgoing signals were separated. The outgoing signal went in the "output" line (green) passed an isolator (actually a circulator working as an isolator) before it was amplified with a cryogenic low noise amplifier positioned at 3-4 K. This circulator was terminated with 50 Ω and worked as an isolator in order to absorb radiation noise coming down from the amplifier line. The amplified signal was further amplified at room temperature before it was measured.

In appended Paper I and II, the "gate" line (red in Figure 4.3) was used to excite the qubit electrically. When the excited qubit relaxed, the emitted SAW propagated across the substrate and could be detected by the IDT. At the IDT it was converted back to electric signal, amplified and measured via the "output" line.

The "transmission input" line (red in Figure 4.3) was used for transmission measurements of the delay lines in the appended Paper III. An electric signal sent via the transmission line to one of the IDTs or FEUDTs, where it was converted to SAWs. The SAWs propagated through the delay line and were detected by the other IDT or FEUDT, where they were converted back to electric signal, amplified and measured via the output line (green).

In the appended Papers IV and V three sets of input/output connections via circulators (previously described as the reflection input and output lines) were used; two connected to an IDT on each side of the sample and one connected to a gate. Each input line was filtered with a high pass filter of 1.9 GHz and a low pass filter of 3 GHz and each output line was filtered with a high pass filter of 1.6 GHz and a low pass filter of 3 GHz to remove noise outside the measurement frequency band.

Most importantly, this setup made simultaneous reflection and transmission measurements possible. A signal could be inputted to one of the IDTs and reflection measured at this IDT while transmission was measured at the other IDT at the same time. This set-up further enabled reflection to be measured at both sides and transmission to be measured in both directions. In addition, the input/output lines connected to the gate were used to address the qubit electrically. This type of measurement made it possible to measure the qubit outside the narrow bandwidth of the IDTs, which enabled detection of the maximum transition frequency of the qubit.

Chapter 5

Results

In this Chapter, the results of the appended papers are introduced. The interaction between SAWs and an artificial atom demonstrated in the appended Papers I and II is presented, motivating the need to improve the conversion between electric microwave signals and SAWs for future quantum SAW experiments. The improvement of the electric/SAW conversion using unidirectional transducers in the appended Paper III is also discussed.

The interaction between an artificial atom and SAWs is further investigated, depicting the appended Papers IV and V. Electromagnetically induced transparency is shown in the appended Paper V using the SAW field as probe and an electromagnetic field as control. Using Autler-Townes splitting, the possibility to utilize the artificial atom as a router of propagating phonons is demonstrated in the appended Paper IV.

5.1 Surface acoustic waves interacting with an artificial atom

An artificial atom coupling to SAWs was demonstrated for the first time in the appended Paper I. The theory and fabrication for the experiment is described more in depth in the appended Paper II, which is a book chapter that also covers theoretical and experimental work for SAW resonators at the quantum level. The SAW resonator work [86, 87] was done by the Leek Lab at the University of Oxford and will not be presented here.

The sample used in the appended Papers I and II (Figure 5.1) was measured at a temperature of 20 mK. It has a single electrode IDT separated 100 μm apart from the artificial atom on the (100) surface of a polished gallium arsenide substrate with propagation along the [011] direction of the crystal. The sender/receiver IDT has 125 unit cells of single electrodes, a center frequency of 4.8066 GHz and an emission bandwidth of about 1 MHz. The artificial atom is of the transmon type [37] described in Chapter 2.2.2 and 3.6. It uses a SQUID with a shunt capacitance made of a double electrode QDT (Qubit coupled IDT) structure with 20 unit cells, which enables the artificial atom to interact with SAWs. The top bus of the electrode structure is connected to one side of the SQUID and the bottom bus is connected to the other island and to ground (Figure 5.1b). The artificial atom has a maximum Josephson energy of 22.2 GHz, and a charging energy and anharmonicity of 220 MHz. The QDT has a center frequency equal to that of the IDT and a bandwidth of 250 MHz. Its coupling to SAWs (acoustic coupling) $\Gamma_{\mathrm{ac}}/2\pi$ is 38 MHz, while the transmon's coupling to the electric gate is 0.75 MHz. The pure

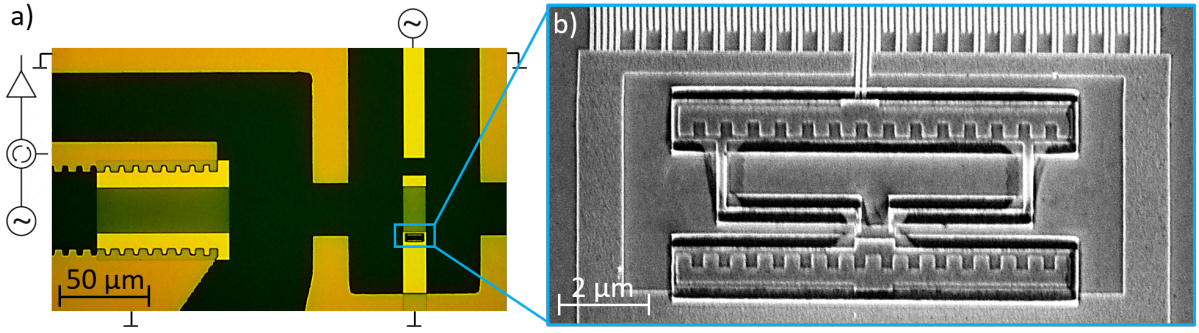

Figure 5.1: a) Optical micrograph of the sample discussed in the appended Paper I and II. Electric signals were sent to or picked up by the single electrode IDT, shown to the left with its upper and lower bus in lighter yellow and its electrodes in blue. The IDT converted the signals into SAWs that propagated on the surface of the GaAs substrate (black) to the SAW artificial atom, shown to the right. The artificial atom could also be excited electrically with a gate, coming in from the top. b) Electron micrograph of the SQUID and its connection to the transducer, which formed the artificial atom coupled to SAWs.

dephasing was estimated to be less than 10 % of the acoustic coupling. The acoustic coupling of the artificial atom is almost six times smaller than its anharmonicity, which made it possible to selectively address energy transitions both acoustically and electrically. Thus, it appeared as a qubit.

The qubit was measured in three ways using the set-up described in Chapter 4: 1) via SAW reflection of the qubit using the IDT for emission and pick-up, 2) via SAW detection with the IDT after electric excitation of the qubit through the gate and 3) via two-tone spectroscopy. In the two-tone spectroscopy, the acoustic reflection was measured with the IDT while the qubit was irradiated with microwaves through the gate. Characterizing the qubit in those three ways, its quantum interaction with SAW and its primary relaxation into SAWs could be demonstrated.

The quantum interaction was highlighted by several different features. The first transition frequency of the qubit could be periodically tuned in and out of resonance with the IDT by changing the magnetic flux through the SQUID loop. This is shown in Figure 2b in the appended Paper I and Figure 11 in the appended Paper II. On resonance, the SAW beam emitted by the IDT was reflected back towards the IDT by the qubit. When the qubit was off resonance, the SAW beam passed the qubit without being reflected.

Furthermore, the reflected SAW power from the qubit was nonlinear in the excitation power (Figure 2f in the appended Paper I). When the incoming power, $P_{in}/(hf) \ll \Gamma_{ac}$, the qubit reflected the SAWs coming from the IDT. As the power increased, the first excited state of the qubit became more populated and the reflection coefficient of the qubit decreased. At high powers, $P_{in}/(hf) \gg \Gamma_{ac}$, the reflection coefficient tended to zero.

This type of saturation behavior was also found when the qubit was excited with an electromagnetic signal applied to the capacitively coupled gate and when it relaxed, it emitted SAWs that could be detected by IDT. The power dependence of the qubit

transduction (blue dots) can be seen in Figure 5.2a, where the qubit transduction decreased nonlinearly with increasing power sent to the gate. At low powers, the power dependence of both the qubit reflection and transduction agreed with the quantum model taking the two lowest energy levels into account (red line in Figure 5.2a) described by Eq. (3.26) in Chapter 3.6. This model also reproduced the reflected SAWs at higher input power, however at these powers the transduction deviated from the model. The deviation was captured by including six energy levels into the quantum model (green line in Figure 5.2) [96, 147].

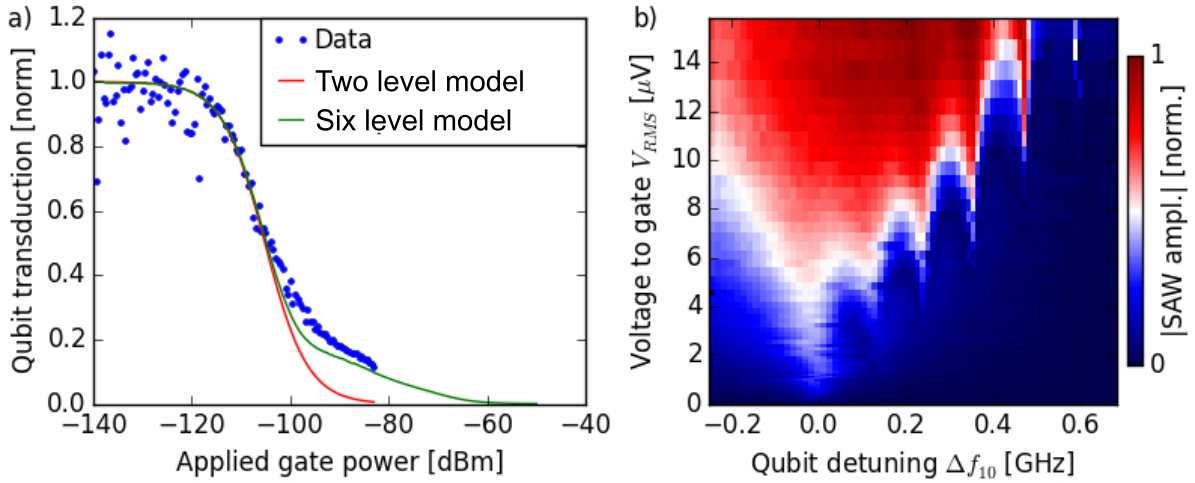

Figure 5.2: a) Qubit transduction from exciting it with the gate and detecting the emitted SAWs with the IDT versus applied power to the gate. The rate the qubit emits phonons is limited by Γ_{ac} and when the power to the gate $P_{\mathrm{gate}}/(hf) \gg \Gamma_{\mathrm{ac}}$ the transduction tends to zero. b) Transduction from the gate to the IDT versus applied power and qubit detuning. At higher power, more than one photon from the gate could excited higher energy states at detuned frequencies. Here six transitions are apparent.

The SAW emission from the qubit was also detected while detuning the resonance frequency of the qubit by applying a magnetic flux though the SQUID loop. At low powers, the qubit could only be excited at its 0-1 resonance frequency. However, at higher power, several photons from the gate could together excite more energy states at detuned frequencies. This is shown in Figure 5.2b, where up to six transitions are visible. The transitions appear when the transition frequencies coincide with the driving frequency, and arise from the same type of physics as when the qubit was excited with SAWs from the IDT. The appearance of higher order energy transitions agree with the full quantum model, and this is shown in Figure 3 in the appended Paper I for the first three energy transitions.

All of the above features show that the first energy transition could be addressed separately from transitions to higher energy states, meaning that the qubit could be treated as a two-level system. In addition, the acoustic coupling rate agreed with the quantum model estimate in Eq. (3.22) in Chapter 3.6 (also in the supplementary material of the appended Paper I and in the appended Paper II). This highlights the quantum interaction between the qubit and SAWs, together with two-tone spectroscopy further

explored in the appended Paper I. However, it is also important to demonstrate that the interaction is indeed acoustic. Therefore, measurements in the time domain were conducted.

Since the gate had a large bandwidth, it could be used to excite the qubit with both short (25 ns in Figure 12 in the appended Paper II) and longer (1 μs in Figure 4 in the appended Paper I) pulses at electric and acoustic resonance. An immediate electric crosstalk signal was measured at the IDT, due to capacitive coupling between the gate and the IDT. 40 ns later, the SAWs emitted by the qubit reached the IDT. This agreed well with the propagation distance and the SAW speed. The emitted SAWs were not only picked up by the IDT, but also reflected back towards the qubit, where the SAWs were reflected again. This echo signal traveled three times the distance of the first SAW signal and was picked up by the IDT 80 ns later. For short pulses, three echoes spaced 80 ns apart could be observed. When longer pulses were used, the SAWs could either be in phase with the electric crosstalk or out of phase. This led to an 80 ns long stepwise increase or decrease of the measured signal. The measurements in the time domain prove that the qubit primarily relaxes by emitting SAW phonons. As mentioned earlier the coupling to the gate was much smaller.

5.1.1 Loss estimation of the transducer

The data from the three types of measurements were fitted using both the full quantum model [96, 147] summarized in the appended Paper II and the quantum model in Chapter 3.6. These fits together with SAW reflection measurement when the qubit was detuned (Figure 2a in Paper I), gave the scattering parameters in Table S1 in the supplementary material of appended Paper I. The electric reflection parameter S_{33}[†] was estimated to 0.51 in amplitude units at the IDT center frequency, from direct measurements (using the same notation as in Chapter 3.2.1). This means that 26 % of the input power was electrically reflected by the IDT.

For the remaining scattering parameters, we assume that the acoustic ports of the IDT are symmetric. Then the electric/SAW conversion parameters $S_{13} = S_{23}$ and the acoustic reflection parameters $S_{11} = S_{22}$ were estimated to a value of 0.28 and 0.55 in amplitude units, respectively. Accordingly, 8 % of the electric signal was converted into SAW in the desired direction and 30 % of the incoming SAW was acoustically reflected by the IDT. Thus, the scattering matrix in Eq. (3.7) in Chapter 3.2.1 (see Figure 5.3) was calculated to

$$S = \begin{pmatrix} 30 & S_{12} & 8 \\ S_{21} & 30 & 8 \\ 8 & 8 & 26 \end{pmatrix} * 0.01, \tag{5.1}$$

where the element $S_{12} = S_{21}$ was not determined. The calculated sum over the last row in Eq. (5.1)

$$S_{13}^2 + S_{23}^2 + S_{33}^2 = 0.42 \tag{5.2}$$

[†]Different notation in the appended Paper I, where port 1 is the electric port, 2 is the acoustic port facing into the delay line and 3 is the other acoustic port *i.e.* $S_{11} = S_{33}$ here.

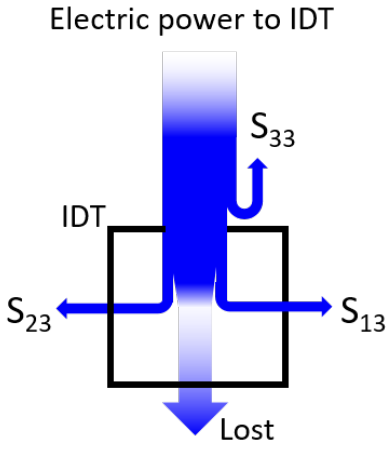

Figure 5.3: Illustration of loss in the single electrode IDT used in the appended Papers I and II. The electric power applied over the IDT is partly electrically reflected (S_{33}) and partly converted to SAW via S_{13} and S_{23}. The power that is not converted to SAW nor electrically reflected is assumed lost.

in squared amplitude units. If the power would be conserved, the sum of the squared elements in each row of the scattering matrix is unity. This means that 58 % of the power sent to the IDT was lost.

Both the high losses and the low bandwidth (1 MHz) are to some extent due to the substrate material. Gallium arsenide is a weak piezoelectric substrate, which has a low electric/SAW conversion and requires many unit cells to impedance match to outer electronics (usually with an impedance of 50 Ω). The high number of unit cells reduces the bandwidth of the IDT. An additional drawback of the IDT used in the appended Papers I and II, is that it is a single electrode IDT. Single electrode IDTs suffer from internal mechanical reflections, which narrows the bandwidth further. The low electric/SAW conversion is obvious from the measurements, where only 8 % was converted in the desired direction. This is a problem when propagating SAWs are used for quantum experiments. To facilitate quantum SAW experiments, the electric/SAW conversion should be improved.

The conversion can be improved by changing the substrate to a stronger piezoelectric material, such as lithium niobate. This also reduces the number of unit cells needed for the impedance matching, and a double electrode IDT can be used which has a higher bandwidth. However, all symmetric IDTs lose 50 % of the power theoretically, because the signal is converted into both acoustic ports and only one port aims into the device (towards the transmon). Therefore, it is interesting to investigate transducers that are not emitting SAWs symmetrically.

5.2 Improved conversion between electric signals and surface acoustic waves

In appended Paper I and II only 8 % of the SAWs was detected by the pick-up transducer. In order to increase the electric/SAW conversion, we investigated both unidirectional transducers and IDTs on a stronger piezoelectric material in the appended Paper III. The improved conversion efficiency by using a unidirectional transducer is the focus of this section.

All samples in the appended Paper III are delay lines on black YZ lithium niobate ($LiNbO_3$), which has an about 70 times stronger electromechanical coupling coefficient than the gallium arsenide substrate used in the appended Paper I and II. The delay lines were measured at 2.3 GHz and 10 mK, and the results are summarized in Table 1 in the appended Paper III. The delay lines consist of two transducers separated with an edge-to-edge distance L of 500 μm (Figure 5.4a). The transducers are either unidirectional transducers (UDTs) or double electrode interdigital transducers (IDTs). The UDTs have 110 (samples FEUDT_1-2) or 160 unit cells (samples FEUDT_3-4) in order to obtain optimized directivity and impedance match to 50 Ω, while the IDTs (Figure 5.4b) have 36 unit cells (samples IDT_1-3). Both transducer types have an electrode overlap W of 35 or 46 μm.

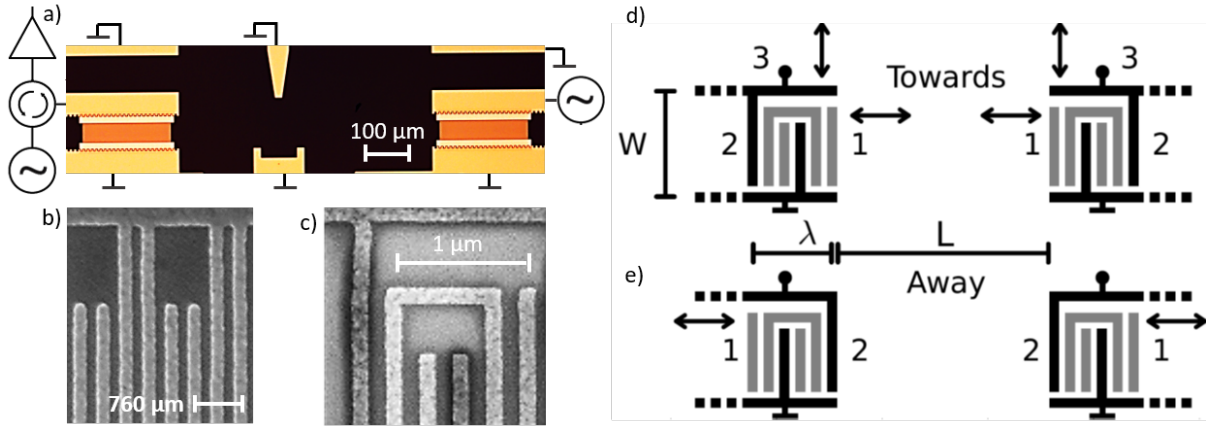

Figure 5.4: a) Optical micrograph of a delay line. Both transducers are either double electrode IDTs or FEUDTs. b) Electron micrograph of the top part of an IDT, where each unit cell has two electrodes connected to the live upper bus and two electrodes connected to the grounded bottom bus. c) Electron micrograph of the top part of one unit cell of a FEUDT [150]. Note that the floating electrodes are brighter due to charging effects. The preferred electric/SAW conversion is towards the right, in port 1. d) A Towards delay line, where port 1 faces inwards and e) an Away delay line, where port 1 faces out from the device. One unit cell is illustrated, where the upper bus is connected to live electrodes, the lower bus is grounded and two of the floating electrodes (gray) are connected.

The UDT design was selected from preliminary measurements of various types of UDTs at 860 MHz and room temperature [149]. It is based on a floating electrode unidirectional transducer (FEUDT) with six electrodes in one unit cell [150], seen in Figure 5.4c and described in Chapter 3.5.2. The design is such that electric/SAW conversion is optimized for port 1 and minimized for port 2 (Figure 5.4d). For optimal transmission, the FEUDTs were placed with port 1 facing into the delay line, *i.e.* port 1 of the two FEUDTs were towards each other. This type of delay line is described as "Towards". In order to compare the transmission through port 1 with port 2, we also measured "Away" delay lines (Figure 5.4e) where port 1 of the FEUDTs were facing out from the device.

The inverse Fourier filtered transmission and reflection (see Chapter 3.4.1) agreed well with the models, see Figure 3 in the appended Paper III. The FEUDT delay lines were in excellent agreement with the COM theory in Chapter 3.5.1, and the IDT delay lines agreed well with the simple SAW circuit model described in Chapter 3.3.1. All Towards delay lines showed higher transmission than the IDT delay lines (Table 1 in the appended Paper III). For instance, FEUDT_3-4 had on average 4.7 dB higher transmission than the IDT delay lines. Furthermore, all Towards delay lines exceeded the theoretical -6 dB minimum insertion loss limiting delay lines with standard symmetric IDTs. The transmission through the IDT delay lines was only -1.6±0.2 dB lower than their -6 dB theoretical limit. This implies that most of the total loss in the IDT delay lines was caused by the IDT's symmetric bi-directionality and only a small part was due to other loss mechanisms.

The directionality of the FEUDTs was measured by comparing the transmission through the Towards and the Away delay lines. A difference of 44 dB was observed (Table 1 in the appended Paper III), which means a directivity of 22 dB per FEUDT and that 99.4 % of the power goes in the desired direction.

Part of the power was not converted back to electric signal, but was acoustically reflected back into the delay line by the transducer. These echo transits were Fourier filtered and fitted with the same model used for the main transmission and reflection, considering multiple acoustic reflections and a longer propagation distance as in Eq. (3.13) and (3.12) in Chapter 3.4. The agreement between the fits (dashed lines) and the first three transits (solid lines) in one FEUDT and one IDT delay line is shown in Figure 5.5a,b, where the first transit is the main transmission. After every transit less power was picked up, partly because it was converted into electric power and partly because it was attenuated every time the SAW transited the delay line. Furthermore, the directivity of the FEUDT *i.e.* the ratio of the transited SAWs in the Towards and Away delay lines decreased for every transit (Figure 5.5c). This can be explained using the scattering parameters shown in Figure 3.7 in Chapter 3.5.1, where the acoustic reflection at port 2 is higher than at port 1 and hence a larger part of the SAWs are transiting multiple times in the "Away" delay lines.

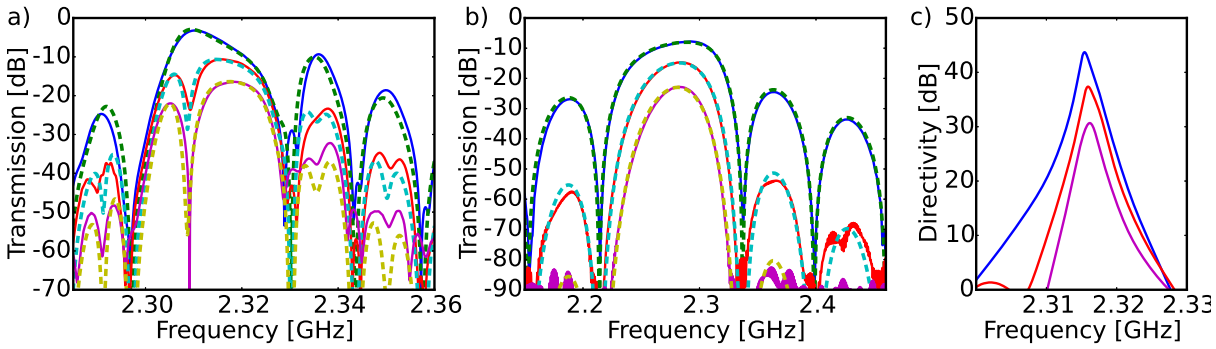

Figure 5.5: Multiple transits in a) sample FEUDT_3 Towards delay line fitted with the COM model and b) sample IDT_5 fitted with the SAW circuit model. The data is shown in solid lines and the fits as dashed lines. The main transmission is the highest in magnitude and each subsequent transit is smaller. All transits are fitted with the same center frequency, but with different attenuation. c) Directivity of sample FEUDT_2: the ratio between the SAW transits in the Towards and Away delay lines.

Table 5.1: The loss in maximum transmission (*Max T*) is higher than the total loss (γ_{tot}) due to directive loss (γ_{D}) and propagation loss. The propagation loss was estimated from loss due to viscous damping (γ_{vis}), beam steering (γ_{bs}) and diffraction (γ_{diff}) over the propagation distance $L + N_p\lambda$. γ_{ue} is the loss that cannot be explained by γ_{D} nor γ_{prop}.

Delay lines			$L + N_p\lambda$	*Max T*	Estimated loss [dB]					
Type	N_p	W[μm]	[μm]	[dB]	γ_{D}	γ_{vis}	γ_{bs}	γ_{diff}	γ_{tot}	γ_{ue}
FEUDT_1	110	35	665	-4.2	-0.06	-0.17	-0.37	-0.61	-1.2	-3.0
FEUDT_2	110	46	665	-3.7	-0.06	-0.17	-0.28	-0.77	-1.3	-2.4
FEUDT_3	160	46	740	-3.2	-0.06	-0.19	-0.31	-0.77	-1.3	-1.9
FEUDT_4	160	46	740	-2.8	-0.06	-0.19	-0.31	-0.77	-1.3	-1.5
IDT_1	36	35	554	-7.8	-6	-0.14	-0.31	-0.61	-7.1	-0.7
IDT_2	36	35	554	-7.7	-6	-0.14	-0.31	-0.61	-7.1	-0.6
IDT_3	36	46	554	-7.5	-6	-0.14	-0.23	-0.77	-7.1	-0.4

5.2.1 Loss estimation of delay lines

In total, -3.5±0.7 dB was lost during the main transmission in the Towards delay lines and -7.6±0.2 dB in the IDT delay lines, shown in Table 5.1. Most of this loss can be explained by the loss from conversion into the wrong acoustic port (directive loss) and propagation loss. The directive loss (γ_{D} in Table 5.1) is the dominating loss in the IDT delay lines and can account for -6 dB, but it can only account for -0.06 dB in the Towards delay lines.

The propagation loss is expected to be similar in FEUDT and IDT delay lines, since all samples were fabricated simultaneously on the same wafer with a fixed transducer orientation and edge-to-edge transducer separation. However, the SAWs travel further underneath the transducers and the distance between the center of the transducer ($L + N_p\lambda$) is a better reference length. This distance is used to estimate the propagation loss (γ_{prop}), which may include beam steering, diffraction and viscous damping [109, 110].

The loss due to beam steering (γ_{bs} in Table 5.1) was estimated from the time the SAWs have to propagate in order to lose -3 dB [110],

$$B_{\text{-3dB}}[dB/s] = \frac{(1-1/\sqrt{2})W}{f\lambda_0 \tan(0.1|\delta\psi/\delta\theta|)}. \tag{5.3}$$

for an alignment error of 0.1° and frequency f. For our system, we get $B_{\text{-3dB}} \approx 2$ μs by using the slope of the power flow angle $|\delta\psi/\delta\theta| = -1.083$ for $LiNbO_3$ [109]. Assuming the SAWs travel the distance $L + N_p\lambda$, the loss due to beam steering is estimated to about -0.3 dB.

The loss due to viscous damping was estimated from the attenuation coefficient, given by

$$\gamma_{\text{att}}[dB/\mu s] = \gamma_{\text{air}}(P)\frac{f}{10^9} + \gamma_{\text{vis}}(T)\left(\frac{f}{10^9}\right)^2 \tag{5.4}$$

in air at room temperature [3]. The first term is due to air loading and the second is due to viscous damping in the substrate. Here, only the second term is important because the experiments were performed in vacuum and gas loading can be ignored. The calculated loss due to viscous damping was a bit more than -0.1 dB, using a viscous damping factor of 0.88 dB/(μs GHz^2) for $LiNbO_3$ at room temperature [110].

The diffraction loss (γ_{diff}) was linearly extrapolated from the results in Ref. [159]. It was estimated to around -0.7 dB, which indicates that it dominates the propagation loss.

The total estimation of the propagation loss is around -1.2±0.1 dB for all delay lines. Consequently, the propagation and directive loss cannot fully account for all loss in the delay lines, leaving an unexplained loss (γ_{ue} in Table 5.1) of -2.2±0.8 dB in the FEUDT Towards delay lines and -0.5±0.2 dB in the IDT delay lines. This loss is higher in the FEUDTs, probably because they have more unit cells. The loss per unit cell, -0.007±0.003 dB, is the same for both types of transducers.

The unexplained loss can be due to transducer imperfections and conversion into acoustic bulk waves. The loss due to transducer imperfections is much bigger at room temperature, when the resistance of the transducers is finite. In experiments with superconducting niobium FEUDTs at 3.5 K, the electrode resistance has been shown to have much bigger effect on the insertion loss than other loss mechanism [114]. Since our transducers were superconducting, this loss should be negligible.

Both the transducer imperfections and the conversion into bulk waves, affect the SAW every time it interacts with the transducer. In order to address the unexplained loss, we expand the three port scattering matrix in Eq. (3.7) in Chapter 3.2.1 to a four port scattering matrix

$$\begin{pmatrix} \phi_{out}^+ \\ \phi_{out}^- \\ V^- \\ \phi_{\text{Loss}} \end{pmatrix} = \begin{pmatrix} S_{11}S_{12}S_{13}S_{14} \\ S_{21}S_{22}S_{23}S_{24} \\ S_{31}S_{32}S_{33}S_{34} \\ S_{41}S_{42}S_{43}S_{44} \end{pmatrix} \begin{pmatrix} \phi_{in}^- \\ \phi_{in}^+ \\ V^+ \\ 0 \end{pmatrix}, \tag{5.5}$$

where the fourth port describes the loss in the transducer, *i.e.* S_{41} is the loss during the acoustic reflection and S_{43} is the loss during the electric to SAW conversion. Both

S_{43} and S_{41} contribute to the unexplained loss ($\gamma_{\text{u.e.}}$). A schematic image over where the losses occur when two transducers are placed in a delay line is shown on Figure 5.6. The main transmission through the delay line suffers from electric reflection (S_{33}) before the electric signal is converted into SAWs. During the conversion, the power is lost to SAWs propagating in the undesired direction ($S_{32} = 2\gamma_{\text{D}}$ from Table 5.1) and to conversion loss (S_{43}). The SAWs that propagate in the desired direction lose some power during the propagation (γ_{prop}) before they reach the other transducer. At the other transducer most of the power is converted to electric signal (S_{31}), but a part is acoustically reflected (S_{11}), a small part is transmitted through the transducer (S_{21}) and some is lost (S_{41}). The acoustically reflected SAWs transit the delay line multiple times and every time γ_{prop} increases with the number of transits and S_{41} increases with the number of interactions with the transducers.

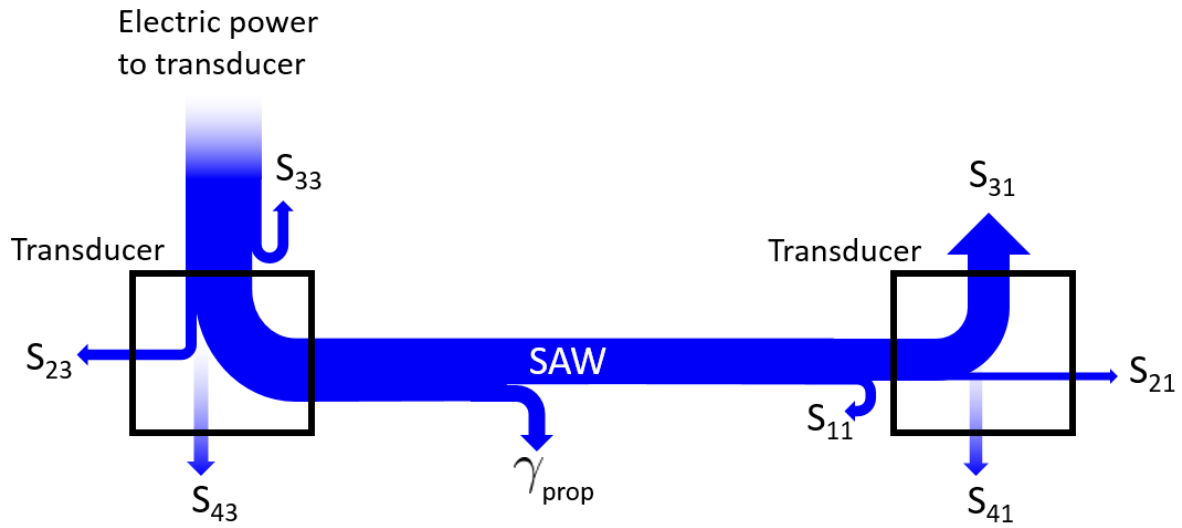

Figure 5.6: Illustration of loss in a delay line with two FEUDTs. For IDTs, S_{23} is of the same size as the signal through the delay line. When an electric signal is sent to a transducer, part of the signal is electrically reflected (S_{33}) and part of the signal is converted to SAWs both in the direction through the delay line, and in the undesired direction (S_{23}). A fraction of the signal is lost during the conversion (S_{43}). The SAW propagating through the delay line loses part of the power (γ_{prop}) before it reaches the other transducer. At the other transducer, the SAW is acoustically reflected (S_{11}), acoustically transmitted (S_{12}) and converted to electric signal (S_{31}). During this, part of the signal is lost (S_{41}). Both S_{43} and S_{41} contribute to the unexplained loss (γ_{ue}), while γ_{prop} can be theoretically estimated.

The loss during the main and multiple transits can be fitted (Figure 5.5) and the fitted attenuation increases for every transit. This increase is linear in dB, which can be seen in Figure 5.7 where it is fitted to the line

$$y(n_t) = (\gamma_{\text{prop}} + S_{41})n_t + S_{43} \tag{5.6}$$

for n_t number of transits. The y-intercept (S_{43}) implies the loss during the conversion from electric signal to SAWs. The slope of the lines ($\gamma_{\text{prop}} + S_{41}$) indicates the sum of the

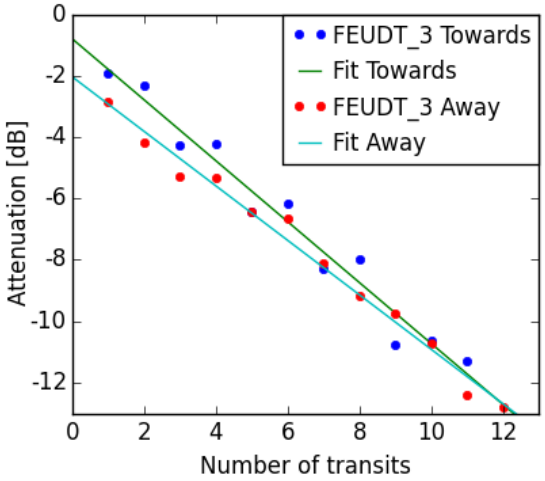

Figure 5.7: Attenuation of each transit in sample FEUDT_3 from COM fittings versus the number of times the SAW has transited the delay line. The attenuation of each delay line was linearly fitted on a logarithmic y-scale.

	Delay lines Type	Slope [dB]	y-intercept [dB]	$y(1)$ [dB]
Towards	FEUDT_1	-0.97	-1.3	-2.2
	FEUDT_2	-0.73	-1.9	-2.6
	FEUDT_3	-0.99	-0.81	-1.8
	FEUDT_4	-1.0	-1.2	-2.2
Away	FEUDT_1	-1.0	-2.3	-3.3
	FEUDT_2	-0.84	-2.2	-3.1
	FEUDT_3	-0.89	-2.0	-2.9
	IDT_1	-1.3	-0.59	-1.9
	IDT_2	-1.3	-0.36	-1.6
	IDT_3	-1.4	0.31	-1.1

Table 5.2: Result of linear fits to the attenuation versus transit. The slope describes $\gamma_{\text{prop}}+S_{41}$, while the y-intercept implies the loss S_{43}. The value of the linear fit at the first transit $y(1)$, estimates the loss for the main transmission.

propagation loss during one transit (γ_{prop}) and the loss during one acoustic reflection (S_{41}). The propagation loss is the total estimated loss due to diffraction, beam steering and viscous damping. The scattering elements S_{33}, S_{23}, S_{31}, S_{11} and S_{21} does not contribute here, because they are already included in both the SAW circuit model and the COM model for fitting the transits. The result of the linear fits is shown in Table 5.2 for all delay lines.

The slope of $y(n_t)$ therefore gives $\gamma_{\text{prop}} + S_{41} \approx -0.9 \pm 0.1$ dB for all FEUDT delay lines, which is close to the estimated propagation loss. The similar value of around -1.3 dB for the IDT delay lines is also close to the estimated propagation loss, implying a very small or no loss during the acoustic reflection. The y-intercept gives $S_{43} \approx -1.5 \pm 0.7$ dB for FEUDT delay lines, whereas it is approximately -0.4 dB for IDT delay lines.

To sum up the losses, the biggest loss in the IDT delay lines is the directive loss, as theoretically predicted, and the remaining loss is mainly propagation loss. For the FEUDTs, the directive loss is minimal in the Towards delay lines, and the transmission is high. Part of the loss in the transmission through the FEUDT delay line is lost during the propagation and this loss is dominated by diffraction loss, which can be improved with a bigger electrode overlap. However, the other part of the loss in the transmission through all types of delay lines cannot be attributed to propagation loss. This loss occurs every time the SAW interacts with the transducer, and scales with the number of unit cells with the same amount for both transducer types. A possible source of this loss is conversion into bulk waves.

The estimated propagation loss on $LiNbO_3$ is comparable to similar estimations for GaAs, which was the substrate used in the appended Papers I and II. For a 500 μm long delay line on GaAs the loss due to viscous damping would be around -0.2 dB, using Eq. (5.4) with a viscous damping factor of 0.9 dB/μs at room temperature [160]. Furthermore, the loss due to beam steering can be estimated to a bit less than -0.2 dB in the same way

as for $LiNbO_3$ with a power flow angle of -0.537 for GaAs [110]. The diffraction could be estimated to -0.5 dB using a parabolic approximation [110]. In total, the propagation loss for the same type of delay lines on $LiNbO_3$ and on GaAs would be similar, but the loss during electric/SAW conversion is bigger on GaAs because it is a much weaker piezoelectric material.

5.2.2 Possibilities for quantum experiments

The electric/SAW conversion efficiency was improved by the use of the stronger piezoelectric substrate and by using FEUDTs in the Towards configuration instead of symmetric double electrode IDTs. Their 4.7 dB higher transmission than the IDT delay lines is due to the 22 dB directivity of each FEUDT. However, the directivity was achieved with a certain number of unit cells, which results in a narrower bandwidth (Table 1 in the appended Paper III). This is useful for on-chip filtering but can be a limitation in quantum SAW experiments.

In quantum SAW experiments, such as in the appended Paper I and II, the qubit couples to SAW phonons using a transducer. This coupling is given by Eq. (3.22) in Chapter 3.6. Since the number of unit cells of the qubit transducer has to be at least one, the minimum acoustic coupling is approximately 100 MHz for a qubit on $LiNbO_3$ at 2.3 GHz. If the qubit coupling is bigger than the bandwidth of the pick-up transducer, the qubit phonon emission will not activate all unit cells in the pick-up transducer. Thus, there is a trade-off between bandwidth and directivity that needs to be optimized for a given experiment.

The minimum coupling of a qubit on $LiNbO_3$ is larger than the bandwidth of both the FEUDTs and the IDTs in the appended Paper III, as it was for the SAW device in the appended Papers I and II. In some quantum experiments, it could be desirable to have a larger bandwidth of the pick-up transducer than the qubit coupling and at the same time use the efficient electric/SAW conversion of the FEUDTs. Then the qubit coupling needs to be decreased. This can be done by addressing the qubit transducer away from its center frequency on one of the side lobes [96, 147] or by inserting an insulating layer between the qubit and the $LiNbO_3$ substrate [3].

Another solution to this trade-off between sufficient coupling versus anharmonicity of the transmon and conversion efficiency of the IDTs, is to use a weak piezoelectric substrate for optimal transmon parameters while either using a matching network for the IDTs or to accept the mismatched impedance. In the latter case, the required bandwidth sets the N_p and the measurement requires better amplification at low temperature (preferably parametric amplifiers) and/or more averaging while measuring. This solution is used (without parametric amplifiers) in the appended Papers IV and V described in the next section.

5.3 Scattering properties of an artificial atom interacting with SAWs

In order to investigate both reflection and transmission of an artificial atom interacting with SAWs, the artificial atom can be placed between two IDTs. This was done in the appended Papers IV and V, where a transmon qubit coupled to SAWs was positioned asymmetrically between two IDTs on GaAs (see Figure 1a in the appended Paper IV) instead of next to one IDT as in the appended Paper I and II. Another difference is that the IDTs, with a center frequency $f_I = 2.2641$ GHz, were designed to have a larger bandwidth at the expense of impedance matching. With 150 double electrodes instead of the 450 needed for optimal conversion efficiency and impedance matching to 50 Ω, the IDTs had a bandwidth of 14 MHz. The QDT has 25 double electrodes, a bandwidth of 80 MHz and the center frequency $f_Q = f_I$. The QDT and the SQUID forming the artificial atom of the transmon type yielded a maximum Josephson energy of 10.7 GHz, a charging energy of 129 MHz and a maximum transition frequency f_{01} between the two lowest energy levels of 3.19 GHz. Its maximum coupling to SAWs occurred at $f_{01} = f_Q$ and was 21 MHz.

To be in the quantum regime, $k_B T \ll \hbar\omega$, the experiment was conducted at a temperature of 12 mK in a set-up described in Chapter 4 and shown in Figure 1b in the appended Paper IV. Each IDT and the gate were connected to both an input line and an output line via two circulators and filters. This enabled simultaneous reflection and transmission measurements. It also enabled gate measurements, where the gate was used to excite the transmon electrically and the emitted SAWs were measured at the two IDTs or the electric reflection was measured at the gate. Using the gate, a larger frequency span could be probed since the measurements are limited by the smallest bandwidth, which for the gate measurements is the bandwidth of the circulators and this is much wider than the bandwidth of the IDTs. Consequently, the gate measurement was used to characterize the transmon and the IDTs were used to show that the transmon primarily relaxed into SAWs when f_{01} was tuned near f_Q.

The detuning $f_{01} - f_Q$ could be controlled in two ways; either by using an external coil to produce a magnetic flux to tune the energy levels of the transmon over a wide range or by applying a microwave tone to the gate at f_{12} to drive the transmon such that the energy levels $|1\rangle$ and $|2\rangle$ are Rabi dressed creating an Autler-Townes splitting. The latter is described in Chapter 2.4.1 and can be seen in Figure 1d in the appended Paper IV. In contrast to tuning the transmon with the external magnetic coil, the latter type of control can be done very fast. Its detuning is limited, but sufficiently large to decouple the transmission from the SAWs.

The strong control at f_{12} causes an Autler-Townes splitting, shown in Figure 3a in the appended Paper IV. This Figure illustrates two-tone spectroscopy, where a weak continuous SAW signal is sent as a probe from IDT A at f_{01} at the same time as the control signal is applied to the gate. Transmission is measured at IDT B while the transmon is tuned with the external magnetic coil and the power of the control is increased. For no or weak control power, the propagating SAWs are transmitted when the transmon's

f_{01} is detuned. However, the transmission is blocked by the transmon when f_{01} is on resonance with the frequency of the SAWs. For substantial control power the Autler-Townes splitting of the energy levels $|1\rangle$ and $|2\rangle$ resulted in two transition frequencies different from f_{01} and hence the transmon no longer blocked the SAWs at zero detuning but at these two other frequencies. As the power of the control was increased, the splitting gradually increased. At even higher control powers, several other features appear and these are due to the combination of the increased Autler-Townes splitting and flux detuning. These features can be seen in Figure 5.8, where both reflection and transmission is shown.

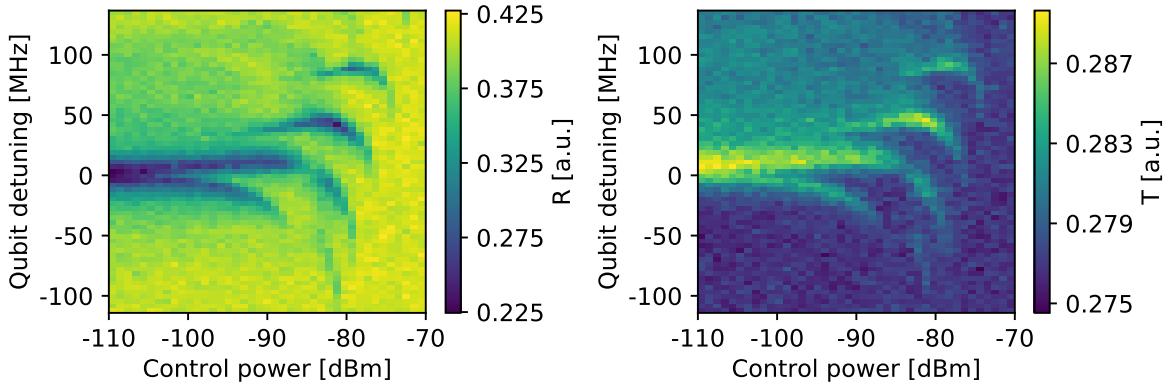

Figure 5.8: Acoustic a) reflection and b) transmission of weak SAWs at the center frequency measured simultaneously while increasing the power of the control signal at f_{12} (sent via the gate) and sweeping the external magnetic coil to change the transition frequencies of the transmon. At lower control powers both reflection and transmission shows an increasing Autler-Townes splitting as in Figure 3a in the appended Paper IV, but at higher control powers (above -95 dBm) more areas that are transparent appear.

The detuning using the Autler-Townes splitting was compared to the detuning using the magnetic coil in Figure 2b in the appended Paper IV. For both ways of detuning the transmon, SAWs were launched from IDT A and the SAWs reflected by transmon (R, triangles) were measured at IDT A at the same time as the transmittance (T, circles) was measured at IDT B (see Figure 1a in the appended Paper IV). When the transmon was detuned from the frequency of the SAWs, the SAWs were transmitted without interacting with the transmon. On resonance, the transmon interacted with the SAWs and partly reflected the SAWs, which gave rise to a reduction in transmittance. This is results in the dip in transmittance at zero detuning in Figure 2a in the appended Paper IV, where the detuning is done using the magnetic coil. For increasing power applied to IDT A, the transmon was gradually saturated and the transmittance approached unity while the reflection approached zero. Both ways to detune the transmon show similar results and these were fitted to the reflectance ($R = |r|^2$) and transmittance ($T = |t|^2$) as a function of incoming SAW power P (described in Eq. (2.63) and (2.65) in Chapter 2.3.3) using $k = \Omega_p/\sqrt{P}$ and pure dephasing Γ_Φ as the only fit parameters. The fits are in good agreements with the acoustic coupling of 21 MHz and gives an estimated pure dephasing of 8 MHz. The pure dephasing limits the extinction in transmission at low SAW powers

to 80 %, which is observed as the deviation from zero in transmission and the deviation from 100 % in reflection at low powers.

The pure dephasing was much less in an early measurement of the same sample as in the appended Papers IV and V. This is presented in Figure 5.9, where the extinction in transmission is 96 % and the fit to both reflection and transmission gives a pure dephasing of 2.6 MHz which less than 13 % of the acoustic coupling of 19 MHz. The difference between the early result and the later results can be understood since it is about half a year between the measurements. During this time the sample was recycled several times to switch other set-ups nearby and as a consequence the magnetic environment was changed. In addition, the sample aged and the normal resistance of the Josephson junctions was slightly changed. These early results show that transmons on GaAs can be designed to achieve sufficiently high extinction in transmission, which is promising for fast control of propagating SAWs in the quantum regime.

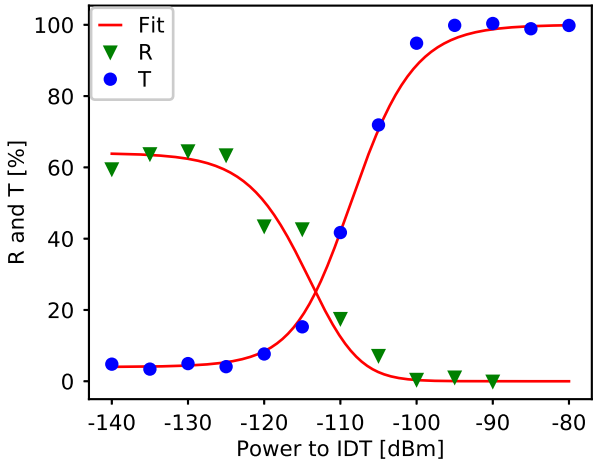

Figure 5.9: Observation of 96 % extinction in transmission (blue dots) of the same sample as in the appended Papers IV and V. The fit (red line) to the transmission is used to normalize the reflection (green triangles) versus power applied to IDT A and gives in a pure dephasing of less than 13 % of the acoustic coupling $\Gamma_{ac} = 19$ MHz.

5.3.1 Fast control of propagating SAWs

For fast control of propagating SAWs, the applied control at the gate was pulsed producing an Autler-Townes splitting while the pulse was turned ON. As previously, SAWs propagating from IDT A were used as probe and the reflected SAWs were measured at IDT A at the same time as the transmitted SAWs were measured at IDT B. The magnetic coil was fixed to keep the transmon f_{01} on resonance with the propagating SAWs. When the pulse was OFF, the SAWs were mostly reflected by the transmon. Turning the pulse ON, the transmon was no longer on resonance with the SAWs and the SAWs were transmitted without interacting with the transmon. This can be seen in Figure 3a in the appended Paper IV for simultaneous reflection (green) and transmission (blue) measured

when a 400 ns pulse was applied to the gate as the control. This experiment demonstrates the proof of principle of a phonon router, where phonons (propagating SAWs) were directed by the transmon either towards IDT A by turning the control pulse ON or towards IDT B by turning the control pulse OFF. The rise time of the router was about 40 ns and the fall time was 160 ns. The rise time was limited by the bandwidth of the IDTs, while the fall time was longer due to multiple transits between IDT B and the transmon. It was also possible to route SAWs using shorter control pulses, shown in Figure 3c in the appended Paper IV. Shorter control pulses than 60 ns resulted in a decreasing amplitude of the measured transmitted SAW field due to the bandwidth of the IDTs.

Hitherto, continuous propagating SAW fields have been controlled. For more advanced in-flight manipulation of SAWs, it will also be important to route SAW pulses and this possibility is shown for simultaneous reflection and transmission measurement in Figure 4 in the appended Paper IV. A 100 ns SAW pulse was generated at IDT A and routed using the external coil to tune the transmon f_{01} in and out of resonance with the frequency of the SAW pulse. When the transmon was detuned (green) the SAW pulse was transmitted without interacting with the transmon. On resonance, it was mostly reflected, but a small part was transmitted even at low powers of the SAW pulse. The imperfect routing of the SAW pulse in this experiment is mainly due to incoherent scattering, which is caused by pure dephasing. However, even in absence of pure dephasing, the performance of the router would still be limited by the relaxation time of the transmon (determined by the inverse of the coupling to SAWs) since full reflection can only be reached for pulse lengths longer than the relaxation time.

5.3.2 Electromagnetically induced transparency using SAWs

Previously we discussed the Autler-Townes splitting where the strong oscillating control field changed the level structure of the transmon and therefore the reflected and transmitted field changed. For lower powers of the control field, another effect called Electromagnetically Induced Transparency (EIT) was observed in the appended Paper V using the same sample and the same type of measurements as in the appended Paper IV.

EIT is described in Chapter 2.4.1 and is in contrast to Autler-Townes splitting, based on interference effects between the transitions of the three lowest energy levels in the transmon [136, 141, 161]. These interference effects are possible in our sample because of the transmon's strong frequency dependence of the coupling strength to SAWs, see Figure 5.10 (blue line). When the transition frequency between the two lowest energy levels of the transmon, f_{01} (red), is on resonance with the center frequency f_Q of the QDT structure, this transition of the transmon couples the strongest to SAWs. Due to the negative anharmonicity approximately equal to the charging energy of 129 MHz, the transition frequency between state $|1\rangle$ and $|2\rangle$, f_{12}, is at a much weaker coupling point (green). Thus, $\Gamma_{10} \gg \Gamma_{21}$ where Γ_{ij} denotes the relaxation rate from the state i to state j (expressed in Eq. (3.22) in Chapter 3.6). The direct transition between the second excited state and the ground state is suppressed by parity conservation, and hence relaxation from the second excited state to the ground state will be via relaxation to the

first excited state. In Figure 5.10 the 80 MHz bandwidth of the QDT is marked with a light blue area.

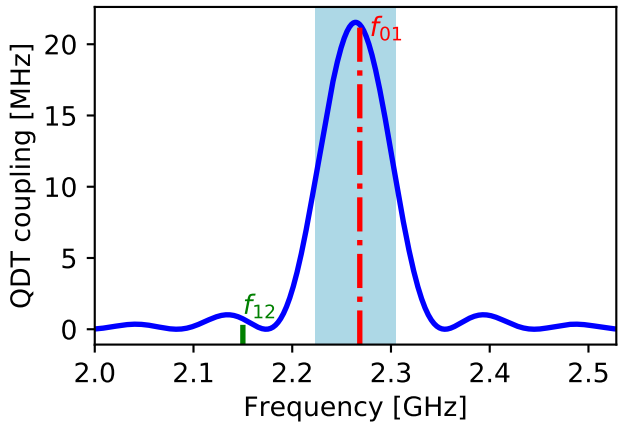

Figure 5.10: Acoustic coupling of the QDT structure (blue) has a maximum at f_Q. When f_{01} (red) is close to f_Q, f_{12} is at frequency where the QDT has a much weaker acoustic coupling. The light blue area marks the bandwidth of the QDT.

Traditionally for measurements of EIT, the probe is swept in frequency. However, in our system the probe is limited by the narrow bandwidth of the IDTs. Thus, we instead used another scheme where the frequency f_C and amplitude of the control field was swept while the frequency of the probing SAWs was fixed to $f_p = f_{01}$. The control field was applied, as previously, via the gate, only limited in the bandwidth by the circulators. For low or no control power, the SAWs were reflected by the transmon as shown in Figure 2a in the appended Paper V. As the power of the control was increased, a dip in reflection appeared for $f_C \approx f_{12} \approx 2.15$ GHz. This dip in reflection is due to EIT, and it is shown in Figure 2b in the appended Paper V. Figure 2b is a cross-section of Figure 2a (red line) at the applied control power to the gate at room temperature of -53 dBm corresponding to 6.1 MHz.

The conditions for realizing EIT are determined by the decoherence rates γ_{10} and γ_{20}, which were extracted from two different types of measurements. The decoherence rate γ_{10} was obtained from analyzing the linewidth of the dip in SAW reflection that appears without any applied control and by only sweeping the external magnetic coil such that f_{10} was tuned in and out of resonance with $f_Q = f_I$. It was found to be 21 MHz and relates through $\gamma_{10} = \Gamma_{10}/2 + \Gamma_\phi$, which is different from $\gamma_{10} \approx 18.5$ found from the relaxation rate $\Gamma_{01} = 21$ MHz and the pure dephasing $\Gamma_\phi \approx 8$ MHz in the appended Paper IV. The different values can be due to aging of the sample and different environment at different cool downs, previously shown in Figure 5.9.

Using the obtained γ_{10}, γ_{20} could be found from analyzing the linewidth of the dip at several applied control powers below the black line in Figure 2a in the appended Paper V. The analysis of the linewidth for different control powers applied at room temperature shows that the linewidth is linearly proportional to the control power, $\gamma_{EIT} = \gamma_{20} + \Omega_C^2/\gamma_{10}$, see black data points Figure 3 in the appended Paper V. The red data points

in Figure 3 shows Ω_C, which is the Rabi frequency given by the control power. From the linear fit of γ_{EIT} (black line), γ_{20} is the y-intercept and was extracted to a value of 4.9±0.14 MHz. Thus, $\gamma_{10} > \gamma_{20}$. Ω_C as the function of applied control power was extracted from the slope of the linear fit.

To discern EIT from Autler-Townes splitting under the given experimental conditions, the theoretical criterion developed in Ref. [136] and described in Chapter 2.4 was used for quantitative distinction. In our system this criterion is equivalent to $\Omega_C < \gamma_{10} - \gamma_{20}$ for $\gamma_{10} > \gamma_{20}$. From the obtained γ_{10} and γ_{20}, the threshold for Ω_C is estimated to 16 MHz corresponding to a control power of -45 dBm applied to the gate at room temperature and -105 dBm applied to the gate at low temperature (see set-up in Figure 1b in the appended Paper IV).

Around the threshold, a crossover from EIT to Autler-Townes splitting takes place. The crossover is indicated with a black line in Figure 2a in the appended Paper V. The EIT regime is below this line and the Autler-Townes regime is above it. Above the threshold, in the Autler-Townes regime, the reflection coefficient can be described as two Lorenztians at two different frequencies. The power used for Autler-Townes splitting the transmon in the appended Paper IV is -20 dBm applied at room temperature corresponding to $\Omega_C = 300$ MHz. This is much larger than the anharmonicity and hence many transitions coexist complicating the response as seen in Figure 5.8.

Below the threshold, the reflection coefficient in Eq. 2.74 can be described as two Lorentzians with different signs, centered at the same frequency, which is the criteria for EIT.

In Figure 1c in the appended Paper V, transmission is shown for three different control powers; one in the Autler-Townes regime (red), one at the crossover (green) and one in the EIT regime (blue). The transmission was measured while an external magnetic flux was swept and both the probe and control frequency were kept constant. However, sweeping the external magnetic flux tunes both f_{01} and f_{12} and consequently both $\partial\omega_p$ and $\partial\omega_c$ were swept simultaneously (see Figure 1c in the appended Paper V).

The results are fitted to

$$t = 1 - \frac{\Gamma_{10}}{2(\gamma_{10} - i\partial\omega_p) + \frac{\Omega_c^2/2}{\gamma_{20} - i(2\partial\omega_p + \delta)}}. \tag{5.7}$$

using γ_{20} and δ as the only fit parameters. This equation is obtained from Eq. (2.75) in Chapter 2.4, assuming a constant transmon anharmonicity during the external magnetic coil sweep, and this is accurate to the first order. Here δ was introduced to account for the slight asymmetry of the line shape in Figure 4 in the appended Paper V. If the probe and control frequency is perfectly aligned with the anharmonicity, $\delta = 0$. Otherwise δ describes the residual control detuning when $\delta_p = 0$ such that $\partial\omega_c = \partial\omega_p + \delta$. From the fits, a δ of 4 MHz was obtained and γ_{20} was extracted to a value of 4.5 ± 0.6 MHz. The obtained γ_{20} is close to the 4.9 ± 0.14 MHz obtained from the reflection measurement.

Chapter 6

Summary and outlook

In this thesis, we have studied propagating surface acoustic waves (SAWs) with the aim for quantum applications. In order to conduct experiments at the quantum level, the systems were cooled down to cryogenic temperatures and operated at microwave frequencies. All devices were placed on a piezoelectric material, either gallium arsenide or lithium niobate. The SAWs were generated and detected with periodic superconducting electrode structures forming interdigital transducers (IDTs). We demonstrated how such superconducting transducers can be unidirectional with high conversion efficiency and large directivity. We also demonstrate how SAWs can interact with an artificial atom in the quantum regime and how this can be used for applications or for studying physical phenomena.

In the appended **Paper I**, we demonstrated the coupling between an artificial atom and SAWs for the first time. The first energy transition of the artificial atom could be addressed selectively and it could be tuned with magnetic flux. The acoustic reflection was measured and found to have a nonlinear power dependence. Transitions between higher energy levels were detected at elevated powers, and in addition, the relaxation of the artificial atom was proven to be dominated by emission of SAWs. These features highlights that the artificial atom coupled primarily to SAWs is of non-classical nature, which was suggested in Refs. [162, 163].

The theory, fabrication and future developments for the experiment was expanded on in the appended **Paper II**, which is a chapter of the book *Superconducting Devices in Quantum Optics* [164]. Part of the theory summarizes a quantum model of the artificial atom coupling to a bosonic field at several separated points [96, 147]. The book chapter also includes theoretical and experimental work for SAW resonators at the quantum level, which is work done by the Leek Lab at the University of Oxford [86, 87].

The results in the appended Papers I and II produce findings parallel to those in quantum optics and are therefore perhaps best described as a new branch in quantum acoustics; circuit quantum acoustodynamics. Circuit quantum acoustodynamics has a promising future to explore new regimes not easily obtained in its optical analogue. Many possible future developments were covered in the appended Paper II, where the slow speed of the SAWs and the coupling strength between SAWs and artificial atoms are the main features.

The first future direction mentioned in the appended Paper II is in-flight manipulation of quantum information. The proof of principle for this was showed in the appended **Paper IV**, where an artificial atom was used to direct propagating SAWs in the quantum regime, in two directions. Depending on if the artificial atom was tuned on resonance with

the propagating SAWs, they were either reflected or transmitted. An 80 % extinction was observed in the transmitted field and the router had a rise time of 40 ns. The extinction of the transmitted SAW field in our device is lower than the extinction of the transmitted electromagnetic field observed in the single photon router in Ref. [138]. The lower extinction in the transmitted SAW field is due to pure dephasing. In an earlier measurement of the same sample, the magnetic environment was different and the observed extinction of the transmitted SAW field was 96 %. This is comparable to results achieved using electromagnetic fields [103, 137, 138]. Although the concept of the router in the appended Paper IV showed a four times slower rise time than the router in Ref. [138], the slow propagation speed of the SAWs might be more important for certain operations.

A future development of the system in the appended Paper IV is to use two artificial atoms with separate tunabilities. Then a SAW pulse could be trapped between the two artificial atoms. For instance in the following way; the first artificial atom is detuned such that the SAW pulse is transmitted towards the second artificial atom, where it is reflected. Before it returns to the first artificial atom, this artificial atom is tuned into resonance with the SAWs and the SAW pulse is trapped. Then the SAW pulse could controllably be let out through either the first artificial atom or the second artificial atom. Since the SAWs propagate slowly in comparison to electromagnetic waves, there is ample time to tune the artificial atoms. Moreover, the spatial extent of a SAW phonon is much smaller than the spatial extent of a microwave photon and the size of a typical device.

Since the artificial atoms in our devices couple to the slowly propagating SAWs using transducers, the artificial atom naturally has the size of several wavelengths. In this sense, the artificial atom is large in comparison to the SAW field and it has no longer a point like interaction. A quantum theory for huge atoms can be found in Ref. [96] and a description of it can be found in the appended Paper II. This theory was further developed in Ref. [9] predicting non-exponential decay of giant atoms, which was experimentally verified in Ref. [99]. The experiment and approach in Ref. [99] was one of the future directions mentioned in the appended Paper II. Expanding on the theory of giant atoms coupled to SAWs, Ref. [98] theoretically describes a system where multiple giant atoms are nested inside each other and performs differently depending on how they are nested. Another interesting development, utilizing the spatial extension of these types of artificial atoms and the slow propagation of the SAWs, is to tune the artificial atom while the SAWs propagates through it.

The fast control of the artificial atom interacting with SAWs in the appended Paper IV was performed using Autler-Townes splitting of the first excited state. Using the same device, Electromagnetically Induced Transparency (EIT) of the SAW field was demonstrated in the appended **Paper V**. To distinguish EIT from Autler-Townes splitting, the criterion in Ref. [136] was used to find the threshold between the two regimes. Both EIT and Autler-Townes regimes were shown as well as the crossover between them. Although EIT has been observed in atomic three-level systems [139, 140], it has been troublesome to properly show EIT in circuit quantum electrodynamic systems. This is due to the difficulty in producing metastable states in these systems and what was thought to be observations of EIT [137, 138], were in fact observations of Autler-Townes splitting [136].

The first proper demonstration of EIT in circuit electrodynamics was done by creating an effective three-level system by combining an artificial atom and a three-dimensional cavity system [141]. An analogue to induced transparency in optomechanical devices has been demonstrated where light beams interact with a mechanical resonator using radiation pressure coupling [142, 143].

Our system in the appended Paper V is in contrast to the other circuit electrodynamic systems, an open quantum system where the possibility to observe EIT is due to the artificial atom's highly frequency dependent coupling to SAWs. The highly frequency dependent coupling can easily be used to suppress certain energy transitions and enhance another by tuning the transition frequencies of the artificial atom relative to the center frequency of the transducer coupling the artificial atom to SAWs. This should be possible to use to create population inversion and single atom SAW lasing (similar to a LASER [21] but with SAW instead of light), which are future directions mentioned in the appended Paper II.

Strong coupling between artificial atoms and SAWs has been demonstrated in both open systems, such as in the appended Paper I, and in cavity systems, such as Ref. [80–82, 84]. In Ref. [84], the strong coupling was used to create non-classical states and in Ref. [165], it has been used for quantum state transfer.

Reaching ultra-strong coupling is of great interest in many fields [166], and is one of the future directions mentioned in the appended Paper II. However, reaching the ultrastrong coupling regime also complicates the ability to address certain transitions in the artificial atom separately and many theoretical models describing quantum physics in superconducting circuits rely on weak coupling approximations, for instance the theory described in Chapter 2.3 in this thesis. These approximations cannot be used for systems in the strong or ultrastrong coupling regime. Since the ultra-strong coupling regime is reachable with SAW coupled artificial atoms, a theory for such a system has been developed in Ref. [116] (see also Papers outside the scope of this thesis). This theory focuses on the role of the IDT structure, which is a part of the artificial atom and enables its coupling to SAWs. As a result of the large spatial extension of the IDT and slow propagation of the SAWs, a strongly SAW coupled artificial atom can be regarded as an atom-cavity-bath system, where the IDT acts as a cavity for the atom instead of an antenna and the artificial atom forms its own cavity. The dynamics of the atom-cavity-bath system is similar to other quantum systems with large time delays, such as the giant atom previously discussed in this chapter.

The last future direction to mention from the appended Paper II is coupling SAWs to optical photons, which was later theoretically described in Ref. [92]. Since the frequency of the SAWs used in all appended Papers have been in the gigahertz range, the wavelength of the SAWs are comparable to those of optical photons. This means that the frequency of the SAWs is comparable to frequencies used in circuit quantum electrodynamics and the wavelength is comparable to optical photons with a five order of magnitude higher frequency. In addition to similar frequencies, many piezoelectric substrates used for SAWs are transparent at optical frequencies and are used in optical applications. With proper conversion methods, it should be possible to couple our systems based on SAWs to optical photons, which propagate in optical fibers and preferred for transportation of quantum

information over long distances.

The appended Papers I and II showed that SAWs can interact in the quantum regime and the appended Papers IV and V further demonstrated how this interaction can be controlled. The ability to control SAWs in the quantum regime suggest that SAWs can be coupled to other quantum systems and that different quantum systems can be coupled via SAWs, for instance to systems utilizing optical photons as described in the previous paragraph. Many of these quantum systems are covered in *The 2019 surface acoustic waves roadmap* [66], which also describes advances in SAW technology ranging from investigations of fundamental quantum effects to applications in life science. Although this thesis focuses on quantum effects, it is possible that advances in different areas can be utilized or connect technologies in other field. The work in this thesis is in a way interdisciplinary, where we combine advances in fields such as superconducting circuit quantum electrodynamics and classical SAW technology.

One future possibility of particular interest for this thesis is how to generate and detect a single quantum of propagating sound (phonon). Such quantum states have been demonstrated in a SAW resonator [84] and a bulk acoustic wave resonator [88]. However, in both these systems, a phonon is localized in a mode of the resonator and not a propagating phonon. The detection of a single propagating phonon and such other future quantum SAW experiments requires highly efficient electric/SAW conversion, which we have sought to address by reducing the primary source of loss in superconducting transducers.

An improved conversion between electric signals and SAWs was found in the appended **Paper III**, where the SAW beam propagated between two floating electrode unidirectional transducers (FEUDTs) [112] in a delay line geometry placed on the strong piezoelectric material lithium niobate. The FEUDTs directed 99.4 % of power into the delay line, which means that less than a percent of power was lost in the undesired direction. This should be compared to the minimum theoretical loss of 50 % for a symmetric IDT. The improved conversion efficiency is useful for studying quantum physics with SAWs, but there is a trade-off between bandwidth and directivity that needs to be optimized for a given experiment. A later work presents similar results using a distributed acoustic reflective transducer (DART), also aiming for usage of quantum SAW devices [115]. Both DARTs and FEUDTs have been investigated in various configurations for classical SAW devices, indicating that they have advantages on different types of substrates [3].

In addition to the reported directivity and improved conversion efficiency, appended Paper III and Chapter 5.2.1 in this thesis also covers a detailed investigation of losses. By systematically studying these loss mechanisms, the losses can be minimized. Low loss is desirable in any kind of quantum information application [66], such as generating and detecting single phonons or processing quantum information.

It should be possible to generate single phonons by exciting an artificial atom and letting it relax by emitting a SAW phonon in a Fock state. In order to prove the quantumness of the emitted sound, one would need to measure its second order correlation function or the Wigner function of the propagation field. To measure the second order correlation function, the bandwidth of the detecting transducer should be larger than

the coupling of the artificial atom generating the phonon. The minimum coupling of an artificial atom on lithium niobate can be estimated to about 100 MHz and this is larger than the bandwidth of the FEUDTs. Either the coupling of the artificial atom needs to be decreased or the number of unit cells of the pick-up transducer needs to be reduced at the cost of directivity and electric/SAW conversion. To keep the high electric/SAW conversion efficiency, the coupling of the artificial atom can be decreased by addressing its shunting transducer away from the center frequency at one of the side lobes of the response function [96, 147]. Alternatively, one could place the artificial atom on a weaker piezoelectric substrate (as in the appended Papers I and II) or insert an insulating layer between the artificial atom and the piezoelectric substrate [3]. The reduction of coupling can be relaxed if the detecting transducers have less number of unit cells and instead the signal can be amplified with parametric amplifiers [167]. This combination could make a single SAW quantum distinguishable taking us towards measurements of quantum sound.

Appendix A

Cleanroom process

All samples were fabricated in the MC2 Nanofabrication Laboratory following the cleanroom process presented in this Appendix. The recipe includes the specific details for fabrication of delay lines and artificial atoms on $LiNbO_3$, but is similar for GaAs substrates. For GaAs the exposure time in the photolithography, the dose in the LASER writing and the electron-beam lithography and the development times are different, and the GaAs wafer was cleaved instead of diced.

1. Cleaning the wafer

1165 Remover	$60 - 70$°C, 10 min
Ultrasonic bath	100%, 1 min
IPA bath	Circulation 2 min
QDR bath	Rinse and blow dry with N_2

2. Photolithography to define alignment and chip marks

Stripping plasma	250 W, 40 sccm O_2, 10 min
Pre-bake in oven	170°C, 2 min
Spin lift-off resist LOR3B	6000 rpm, 1 min, $t_{acc} = 2$ s ($t \approx 300$ nm)
Softbake in oven	170°C, 10 min
Spin photoresist S1813	4000 rpm, 1 min, $t_{acc} = 2$ s ($t \approx 1.3$ μm)
Softbake on hotplate	110°C, 2 min
Expose pattern	MA6 mask aligner, Low-vac mode, $P_{vac} = 0.4$ bar, 6 W/cm^2, $t_{exp} = 10$ s
Develop in MF319	90 s
QDR bath	Rinse and blow dry with N_2

3. Electron beam evaporation of metals in Lesker PVD225

Ashing in O_2-plasma	50 W, 10 s
E-beam evaporation	$P_{ch} \leq 10^{-7}$mbar Sticking layer (Ti), 5 nm , 0.1 nm/s Contact layer (Au), 85 nm, 0.1-0.2 nm/s Stopping layer (Pd), 10 nm, 0.1 nm/s
Lift-off in 1165 Remover	$60 - 70$°C, overnight
IPA bath	2 min
QDR bath	Rinse and blow dry with N_2

4. Dicing of wafer into quarters from backside

Pre-bake in oven	110°C, 2 min
Spin protective resist S1813	4000 rpm, 1 min, $t_{acc} = 2$ s ($t \approx 1.3$ μm)
Softbake on hotplate	110°C, 2 min
Align to photolithography marks	with backside alignment
Cuts through substrate (backside)	Dice the wafer into quartes
Strip resist in 1165 Remover	$60 - 70$°C, 10 min, sonicate 3 min
	Rinse in IPA and blow dry with N_2 ($\times$ 2 times)

5. Electron beam lithography for transducers

Ashing in O_2-plasma	50 W, 10 s
Pre-bake on hotplate	170°C, 3 min
Spin lift-off resist MMA/cop EL2	2000 rpm, $t_{acc} = 2$ s for 1 min ($t \approx 36$ nm)
Softbake on hotplate	170°C, 5 min
Spin e-beam resist ZEP 520A(1:2) in Anisol	3000 rpm, $t_{acc} = 2$ s, 1 min ($t \approx 80$ nm)
Softbake on hotplate	170°C, 5 min
Spin E-spacer 300Z	2000 rpm $t_{acc} = 5$ s, 1 min
Softbake on hotplate	130°C, 2 min
Expose JEOL JBX-9300FS	100kV, 2nA,
	Nominal dose: 152 μC/cm^2 $LiNbO_3$,
	44 proximity corrected doses.
Remove E-spacer	QDR, blow dry with N_2
Develop top resist	N-Amyl-Acetate, 60 sec
	Blow dry with N_2
Develop bottom resist	MIKBK:IPA 1:1, 30 sec
	Blow dry with N_2

6. Electron beam evaporation of metals in Lesker PVD225

Ashing in O_2-plasma	50 W, 10 s
E-beam evaporation	$P_{ch} \leq 10^{-7}$mbar
	Contact layer (Al), 27 nm, 0.1 nm/s
	Stopping layer (Pd), 3 nm, 0.1 nm/s
Lift-off in 1165 Remover	$60 - 70$°C, overnight
IPA bath	2 min
H_2O bath	Rinse and blow dry with N_2

7. LASER writer for contact pads and ground planes

Stripping plasma	250 W, 40 sccm O_2, 1 min
Pre-bake on hotplate	170°C, 3 min
Spin protective resist MMA/cop EL2	2000 rpm, $t_{acc} = 2$ s for 1 min (t $\approx$ 36 nm)
Softbake on hotplate	170°C, 5 min
Spin lift-off resist LOR3A	6000 rpm, 1 min, $t_{acc} = 2$ s (t $\approx$ 250 nm)
Softbake on hotplate	170°C, 5 min
Spin photoresist S1813	4000 rpm, 1 min, $t_{acc} = 2$ s (t $\approx$ 1.3 μm)
Softbake on hotplate	110°C, 2 min
Expose	
Develop	MF319, 75 sec
	Rinse and blow dry with N_2
Remove copolymer	H_2O:IPA 1:4, 30 sec
	Rinse and blow dry with N_2
	Dip in new H_2O:IPA 1:4
	Rinse and blow dry with N_2

8. Electron beam evaporation of metals in Lesker PVD225

Ashing in O_2-plasma	50 W, 10 s
E-beam evaporation	$P_{ch} \leq 10^{-7}$mbar
	Sticking layer (Ti), 5 nm , 0.1 nm/s
	Contact layer (Au), 85 nm, 0.1-0.2 nm/s
	Stopping layer (Pd), 10 nm, 0.1 nm/s
Lift-off in 1165 Remover	$60 - 70$°C, overnight
IPA bath	2 min
	Rinse in IPA, water and blow dry with N_2

9. Electron beam lithography to define SQUIDs

Ozone	10 min
Pre-bake on hotplate	180°C, 3 min
Spin lift-off resist MMA EL10	2000 rpm, $t_{acc} = 2$ s for 1 min (t $\approx$ 500 nm)
Softbake on hotplate	180°C, 5 min
Spin e-beam resist AR-P6200.13 1:2 in Anisol	2000 rpm, $t_{acc} = 2$ s, 1 min (t $\approx$ 100 nm)
Softbake on hotplate	180°C, 5 min
Spin E-spacer 300Z	2000 rpm $t_{acc} = 5$ s, 1 min
Softbake on hotplate	130°C, 2 min
Expose JEOL JBX-9300FS	100kV, 2nA,
	Nominal dose: 240 μC/cm^2 $LiNbO_3$,
	11 proximity corrected doses.
Remove E-spacer	QDR, blow dry with N_2

10a. Dicing of wafer from backside for devices with SQUIDs

Align to marks	with backside alignment
Cuts through substrate (backside)	Dice the quarters into chips

10b. Dicing of wafer from backside for devices without SQUIDs

Pre-bake in oven	110°C, 2 min
Spin protective resist S1813	4000 rpm, 1 min, $t_{acc} = 2$ s ($t \approx 1.3$ μm)
Softbake on hotplate	110°C, 2 min
Align to marks	with backside alignment
Cuts through substrate (backside)	Dice the quarters into chips
Strip resist in 1165 Remover	$60 - 70$°C, $t \approx 10$ min
	Rinse in IPA, water and blow dry with N_2 ($\times$ 2 times)

11. Two-angle evaporation of SQUIDs in Plassys

Develop top resist	n-amyl acetate, 90 s
Develop bottom resist	H_2O:IPA 1:4, 6 min
Ashing in oxygen plasma	50 W, 10 s
Electron beam evaporation	$P_{ch} \leq 2 \times 10^{-7}$ mbar
Bottom layer of Al	40 nm, 5Å/s, $\alpha = 15°$
Dynamic oxidation	$P_{ox} = 0,17$ mbar, $t_{ox} = 10$ min
Top layer of Al	60 nm, 5Å/s, $\alpha = -15°$
Lift-off in 1165 Remover	$60 - 70$°C, overnight
	Rinse in IPA, water and blow dry with N_2

Acknowledgments

I would like to start with expressing my gratitude towards my main supervisor professor Per Delsing for giving me the opportunity to carry out my doctoral studies in his group.

Next, I thank Thomas Aref who not only supervised me in the measurement laboratory but also took the time to give me scientific feedback and support in writing during my first three years of PhD-studies. These years would have been much harder and less fun without his scientific contribution, assistance and guidance.

I also thank all co-authors for our contributed parts to the appended Papers and the Paper outside the scope of this thesis.

This work was supported by The Swedish Research Council and The Knut and Alice Wallenberg foundation. The samples were made at the Nanofabrication Laboratory at Chalmers University of Technology.

I am very grateful for the support from the Nanofabrication Laboratory personnel and from my colleagues and friends Susannah Carlsson and Joel Lindkvist.

Last but not the least, to my family and friends, thank you for endless support.

Maria Ekström

Göteborg, 2020

Bibliography

[1] T. Rossing. *Springer Handbook of Acoustics*. Springer, Stanford, CA, 94305, USA, second edition, 01 2014.

[2] S. Datta. *Surface Acoustic Wave Devices*. Prentice-Hall, Englewood Cliffs, NJ, 1986.

[3] D. Morgan. *Surface Acoustic Wave Filters*. Academic Press, Amsterdam, second edition, 2007.

[4] R. M. White and F. W. Voltmer. Direct piezoelectric coupling to surface elastic waves. *Appl. Phys. Lett.*, 7:314, 1965.

[5] D.M. Pozar. *Microwave engineering; 3rd ed.* Wiley, Hoboken, NJ, 2005.

[6] D.F. Walls and G.J. Milburn. *Quantum Optics*. Springer-Verlag Berlin Heidelberg, Berlin, Germany, second edition, 2008.

[7] C. Gerry and P. Knight. *Introductory Quantum Optics*. Cambridge University Press, 2004.

[8] R. J. Schoelkopf and S. M. Girvin. Wiring up quantum systems. *Nature*, 451:664, 2008.

[9] X. Gu, A. Frisk Kockum, A. Miranowicz, Y.-x. Liu, and F. Nori. Microwave photonics with superconducting quantum circuits. *Phys. Rep.*, 718-719:1–102, 2017.

[10] R.G. Hulet, E.S. Hilfer, and D. Kleppner. Inhibited spontaneous emission by a rydberg atom. *Phys. Rev. Lett.*, 55:2137–2140, 1985.

[11] F. De Martini, G. Innocenti, G. R. Jacobovitz, and P. Mataloni. Anomalous spontaneous emission time in a microscopic optical cavity. *Phys. Rev. Lett.*, 59:2955–2958, 1987.

[12] W. Jhe, A. Anderson, E. A. Hinds, D. Meschede, L. Moi, and S. Haroche. Suppression of spontaneous decay at optical frequencies: Test of vacuum-field anisotropy in confined space. *Phys. Rev. Lett.*, 58:666–669, 1987.

[13] A. Wallraff, D. I. Schuster, A. Blais, L. Frunzio, R.-S. Huang, J. Majer, S. Kumar, S. M. Girvin, and R. J. Schoelkopf. Strong coupling of a single photon to a superconducting qubit using circuit quantum electrodynamics. *Nature*, 431:162, 2004.

[14] A. Blais, R.-S. Huang, A. Wallraff, S.M. Girvin, and R.J. Schoelkopf. Cavity quantum electrodynamics for superconducting electrical circuits: An architecture for quantum computation. *Phys. Rev. A*, 69:062320, 2004.

[15] R Miller, T E Northup, K M Birnbaum, A Boca, A D Boozer, and H J Kimble. Trapped atoms in cavity QED: coupling quantized light and matter. *J. Phys. B.*, 38:S551, 2005.

[16] S. Haroche and D. Kleppner. Cavity quantum electrodynamics. *Phys. Today*, 42:24, 1989.

[17] E. T. Jaynes and F. W. Cummings. Comparison of quantum and semiclassical radiation theories with application to the beam maser. *Proceedings of the IEEE*, 51:89–109, 1963.

[18] R. J. Thompson, G. Rempe, and H. J. Kimble. Observation of normal-mode splitting for an atom in an optical cavity. *Phys. Rev. Lett.*, 68:1132–1135, 1992.

[19] C. J. Hood, M. S. Chapman, T. W. Lynn, and H. J. Kimble. Real-time cavity QED with single atoms. *Phys. Rev. Lett.*, 80:4157–4160, 1998.

[20] M. Brune, F. Schmidt-Kaler, A. Maali, J. Dreyer, E. Hagley, J. M. Raimond, and S. Haroche. Quantum Rabi oscillation: A direct test of field quantization in a cavity. *Phys. Rev. Lett.*, 76:1800–1803, 1996.

[21] M. Bertolotti. *The History of the Laser*. IOP Publishing Ltd, 2005.

[22] T.W. Hänsch and A.L. Schawlow. Cooling of gases by laser radiation. *Optics Communications*, 13:68 – 69, 1975.

[23] D.J. Wineland and W.M. Itano. Laser cooling. *Phys. Today*, 40:34, 1975.

[24] D.N. Klyshko, A.N. Penin, and B.F. Polkovnikov. Parametric luminescence and light scattering by polaritons. *JETP Lett.*, 9:40, 1969.

[25] D.C. Burnham and D.L. Weinberg. Observation of simultaneity in parametric production of optical photon pairs. *Phys. Rev. Lett.*, 25:84–87, 1970.

[26] C. Monroe, D. M. Meekhof, B. E. King, W. M. Itano, and D. J. Wineland. Demonstration of a fundamental quantum logic gate. *Phys. Rev. Lett.*, 75:4714–4717, 1995.

[27] F. Schmidt-Kaler, H. Häffner, M. Riebe, S. Gulde, G.P.T. Lancaster, T. Deuschle, C. Becher, C.F. Roos, J. Eschner, and R. Blatt. Demonstration of a fundamental quantum logic gate. *Nature*, 422:408, 2003.

[28] The Royal Swedish Academy of Sciences. The Nobel prize in physics 2012 - advanced information, 2012. `www.nobelprize.org/nobel_prizes/physics/laureates/2012/advanced.html` (Visited 2016-11-11).

[29] D. J. Wineland. Nobel lecture: Superposition, entanglement, and raising schrödinger's cat. *Rev. Mod. Phys.*, 85:1103, 2013.

[30] S. Haroche. Nobel lecture: Controlling photons in a box and exploring the quantum to classical boundary. *Rev. Mod. Phys.*, 85:1083, 2013.

[31] C. Guerlin, J. Bernu, S. Deléglise, C. Sayrin, S. Gleyzes, S. Kuhr, M. Brune, J.-M. Raimond, and S. Haroche. Progressive field-state collapse and quantum non-demolition photon counting. *Nature*, 448:889, 2007.

[32] R. Hanson, L. P. Kouwenhoven, J. R. Petta, S. Tarucha, and L. M. K. Vandersypen. Spins in few-electron quantum dots. *Rev. Mod. Phys.*, 79:1217, 2007.

[33] M. V. G. Dutt, L. Childress, L. Jiang, E. Togan, J. Maze, F. Jelezko, A. S. Zibrov, P. R. Hemmer, and M. D. Lukin. Quantum register based on individual electronic and nuclear spin qubits in diamond. *Science*, 316:1312, 2007.

[34] H. de Riedmatten, M. Afzelius, M. U. Staudt, C. Simon, and N. Gisin. A solid-state light-matter interface at the single-photon level. *Nature*, 456:773, 2008.

[35] V. Bouchiat, D. Vion, P. Joyez, D. Esteve, and M. Devoret. Quantum coherence with a single cooper pair. *Phys. Scr.*, 1998:165, 1998.

[36] Y. Nakamura, Yu A. Pashkin, and J. S. Tsai. Coherent control of macroscopic quantum states in a single-cooper-pair box. *Nature*, 398:786–788, 1999.

[37] J. Koch, T. M. Yu, J. Gambetta, A. A. Houck, D. I. Schuster, J. Majer, A. Blais, M. H. Devoret, S. M. Girvin, and R. J. Schoelkopf. Charge-insensitive qubit design derived from the cooper pair box. *Phys. Rev. A*, 76:042319, 2007.

[38] C.H. van der Wal, A. C. J. ter Haar, F. K. Wilhelm, R. N. Schouten, C. J. P. M. Harmans, T. P. Orlando, S. Lloyd, and J. E. Mooij. Quantum superposition of macroscopic persistent-current states. *Science*, 290:773–777, 2000.

[39] J.R. Friedman, V. Patel, W. Chen, S.K. Tolpygo, and J.E. Lukens. Quantum superposition of distinct macroscopic states. *Nature*, 406:43–6, 2000.

[40] J.M. Martinis, S. Nam, J. Aumentado, and C. Urbina. Rabi oscillations in a large Josephson-junction qubit. *Phys. Rev. Lett.*, 89:117901, 2002.

[41] J. D. Teufel, T. Donner, M. A. Castellanos-Beltran, J. W. Harlow, and K. W. Lehnert. Nanomechanical motion measured with an imprecision below that at the standard quantum limit. *Nat. Nanotech.*, 4:820, 2009.

[42] M. D. LaHaye, J. Suh, P. M. Echternach, K. C. Schwab, and M. L. Roukes. Nanomechanical measurements of a superconducting qubit. *Nature*, 459:960, 2009.

[43] A.D. OĆonnell, M. Hofheinz, M. Ansmann, R. Bialczak, M. Lenander, E. Lucero, M. Neeley, D. Sank, H. Wang, M. Weides, J. Wenner, J. Martinis, and A. Cleland. Quantum ground state and single-phonon control of a mechanical resonator. *Nature*, 464:697–703, 2010.

[44] J. M. Pirkkalainen, S. U. Cho, J. Li, G. S. Paraoanu, P. J. Hakonen, and M. A. Sillanpää. Hybrid circuit cavity quantum electrodynamics with a micromechanical resonator. *Nature*, 494:211, 2013.

[45] A. Dorsel, J. D. McCullen, P. Meystre, E. Vignes, and H. Walther. Optical bistability and mirror confinement induced by radiation pressure. *Phys. Rev. Lett.*, 51:1550–1553, 1983.

[46] M. Aspelmeyer, T.J. Kippenberg, and F. Marquardt. Cavity optomechanics. *Rev. Mod. Phys.*, 86:1391–1452, 2014.

[47] V.B. Braginskii and A.B. Manukin. Ponderomotive effects of electromagnetic radiation. *Sov. Phys. JETP*, 25:653, 1966.

[48] V.B. Braginskii, A.B. Manukin, and M. Y. Tikhonov. Investigation of dissipative ponderomotive effects of electromagnetic radiation. *Sov. Phys. JETP*, 31:829, 1970.

[49] O. Arcizet, V. Jacques, A. Siria, P. Poncharal, P. Vincent, and S. Seidelin. A single nitrogen-vacancy defect coupled to a nanomechanical oscillator. *Nat. Phys.*, pages 879–883, 2011.

[50] S. Kolkowitz, A.C.B. Jayich, Q.P. Unterreithmeier, S.D. Bennett, P. Rabl, J. G. E. Harris, and M.D. Lukin. Coherent sensing of a mechanical resonator with a single-spin qubit. *Science*, 335:1603–1606, 2012.

[51] K.W. Lee, D. Lee, P. Ovartchaiyapong, J. Minguzzi, Jero R. Maze, and Ania C. Bleszynski Jayich. Strain coupling of a mechanical resonator to a single quantum emitter in diamond. *Phys. Rev. Applied*, 6:034005, 2016.

[52] I. Yeo, P.-L. de Assis, A. Gloppe, E. Dupont-Ferrier, P. Verlot, N. Malik, E. Dupuy, J. Claudon, J.-M. Gérard, A. Auffèves, G. Nogues, S. Seidelin, J.-P. Poizat, O. Arcizet, and M. Richard. Strain-mediated coupling in a quantum dot-mechanical oscillator hybrid system. *Nature Nanotech.*, 9:106–110, 2014.

[53] J. Jost, J. Home, J. Amini, D. Hanneke, R. Ozeri, C. Langer, J. Bollinger, D. Leibfried, and D. Wineland. Entangled mechanical oscillators. *Nature*, 459:683–5, 2009.

[54] K. C. Lee, M. R. Sprague, B. J. Sussman, J. Nunn, N. K. Langford, X.-M. Jin, T. Champion, P. Michelberger, K. F. Reim, D. England, D. Jaksch, and I. A. Walmsley. Entangling macroscopic diamonds at room temperature. *Science*, 334:1253–1256, 2011.

[55] C. Ockeloen-Korppi, E. Damskägg, J.-M Pirkkalainen, M. Asjad, A. Clerk, F. Massel, M. Woolley, and M. Sillanpää. Stabilized entanglement of massive mechanical oscillators. *Nature*, 556:478–482, 2018.

[56] T. A. Palomaki, J. D. Teufel, R. W. Simmonds, and K. W. Lehnert. Entangling mechanical motion with microwave fields. *Science*, 342:710–713, 2013.

[57] R. Riedinger, A. Wallucks, I. Marinkovic, C. Löschnauer, M. Aspelmeyer, S. Hong, and S. Gröblacher. Remote quantum entanglement between two micromechanical oscillators. *Nature*, 556:473–477, 2018.

[58] H.J. Kimble. The quantum internet. *Nature*, 453:1023–30, 2008.

[59] Z. Huang, K. Cui, G. Bai, X. Feng, F. Liu, W. Zhang, and Y. Huang. High-mechanical-frequency characteristics of optomechanical crystal cavity with coupling waveguide. *Sci Rep*, 6:34160, 2016.

[60] F. Guo et al. Controlling cell-cell interactions using surface acoustic waves. *Proc. Nat. Acad. Sci.*, 112:43–48, 2015.

[61] M. Stamp, A. Jötten, P. Kudella, D. Breyer, F. Strobl, T. Geislinger, A. Wixforth, and C. Westerhausen. Exploring the limits of cell adhesion under shear stress within physiological conditions and beyond on a chip. *Diagnostics*, 6:38, 2016.

[62] A. Wixforth. Acoustically driven planar microfluidics. *Superlattices Microstruct.*, 33:389–396, 2003.

[63] T. Franke, S. Braunmüller, L. Schmid, A. Wixforth, and D. A. Weitz. Surface acoustic wave actuated cell sorting (sawacs). *Lab Chip*, 10:789–794, 2010.

[64] C Caliendo and M Hamidullah. Guided acoustic wave sensors for liquid environments. *J. Phys. D: Appl. Phys.*, 52:153001, 2019.

[65] B. Paschke, A. Wixforth, D. Denysenko, and D. Volkmer. Fast surface acoustic wave-based sensors to investigate the kinetics of gas uptake in ultra-microporous frameworks. *ACS Sensors*, 2:740–747, 2017.

[66] P. Delsing et al. The 2019 surface acoustic waves roadmap. *J. Phys. D: Appl. Phys.*, 52(35), 2019.

[67] C. H. W. Barnes, J. M. Shilton, and A. M. Robinson. Quantum computation using electrons trapped by surface acoustic waves. *Phys. Rev. B*, 62:8410–8419, 2000.

[68] H.J. Krenner, S. Stufler, M. Sabathil, E.C. Clark, P. Ester, M. Bichler, G. Abstreiter, J.J. Finley, and A. Zrenner. Recent advances in exciton-based quantum information processing in quantum dot nanostructures. *New J. Phys.*, 7:184–184, 2005.

[69] J. Rudolph, R. Hey, and P. V. Santos. Long-range exciton transport by dynamic strain fields in a GaAs quantum well. *Phys. Rev. Lett.*, 99:047602, 2007.

[70] P. Lidon, L. Villa, N. Taberlet, and S. Manneville. Measurement of the acoustic radiation force on a sphere embedded in a soft solid. *Appl. Phys. Lett.*, 110:044103, 2017.

[71] L. Bandhu and G. Nash. Controlling the properties of surface acoustic waves using graphene. *Nano Res.*, 9:685–691, 2016.

[72] J. Liang, B. Liu, H. Zhang, M. Zhang, D. Zhang, and W. Pang. Monolithic acoustic graphene transistors based on lithium niobate thin film. *J. Phys. D: Appl. Phys.*, 51:204001, 2018.

[73] W. J. M. Naber, T. Fujisawa, H. W. Liu, and W. G. van der Wiel. Surface-acoustic-wave-induced transport in a double quantum dot. *Phys. Rev. Lett.*, 96:136807, 2006.

[74] E. A. Cerda-Méndez, D. N. Krizhanovskii, M. Wouters, R. Bradley, K. Biermann, K. Guda, R. Hey, P. V. Santos, D. Sarkar, and M. S. Skolnick. Polariton condensation in dynamic acoustic lattices. *Phys. Rev. Lett.*, 105:116402, 2010.

[75] S. Hermelin, S. Takada, M. Yamamoto, S. Tarucha, A. D. Wieck, L. Saminadayar, C. Bäuerle, and T. Meunier. Quantum physics: Single electrons take the bus. *Nature*, 477:435, 2011.

[76] R. P. G. McNeil, M. Kataoka, C. J. B. Ford, C. H. W. Barnes, D. Anderson, G. A. C. Jones, I. Farrer, and D. A. Ritchie. On-demand single-electron transfer between distant quantum dots. *Nature*, 477:439, 2011.

[77] J. Stotz, R. Hey, P. Santos, and K. Ploog. Coherent spin transport through dynamic quantum dots. *Nature materials*, 4:585–8, 2005.

[78] B. Bertrand, S. Hermelin, S. Takada, M. Yamamoto, S. Tarucha, A. Ludwig, A. Wieck, and C. Bäuerle. Fast spin information transfer between distant quantum dots using individual electrons. *Nature nanotech.*, 11:672–676, 2016.

[79] T.-K. Hsiao, A. Rubino, Y. Chung, S.-K. Son, H. Hou, J. Pedrós, A. Nasir, G. Éthier-Majcher, M. Stanley, R. Phillips, T. Mitchell, J. Griffiths, I. Farrer, D. Ritchie, and C. Ford. Single-photon emission from single-electron transport in a SAW-driven lateral light-emitting diode. *Nature Communications*, 11:917, 2020.

[80] R. Manenti, A. Frisk Kockum, A. Patterson, T. Behrle, J. Rahamim, G. Tancredi, F. Nori, and P. J. Leek. *Nat. Commun.*, 8:975, 2017.

[81] A. Noguchi, R. Yamazaki, Y. Tabuchi, and Y. Nakamura. *Phys. Rev. Lett.*, 119:180505, 2017.

[82] B.A. Moores, L.R. Sletten, J.J. Viennot, and K. W. Lehnert. Cavity quantum acoustic device in the multimode strong coupling regime. *Phys. Rev. Lett.*, 120:227701, 2018.

[83] A.N. Bolgar, J.I. Zotova, D.D. Kirichenko, I.S. Besedin, A.V. Semenov, R.S. Shaikhaidarov, and O.V. Astafiev. Quantum regime of a two-dimensional phonon cavity. *Phys. Rev. Lett.*, 120:223603, 2018.

[84] K. Satzinger, Y. Zhong, H-S Chang, G. Peairs, A. Bienfait, M.-H. Chou, A. Cleland, C. Conner, E. Dumur, J. Grebel, I. Gutierrez, B. November, R. Povey, S. Whiteley, D. Awschalom, D. Schuster, and A. Cleland. Quantum control of surface acoustic wave phonons. *Nature*, 563:661–665, 2018.

[85] L. R. Sletten, B. A. Moores, J. J. Viennot, and K. W. Lehnert. Resolving phonon fock states in a multimode cavity with a double-slit qubit. *Phys. Rev. X*, 9:021056, 2019.

[86] R. Manenti, M. J. Peterer, A. Nersisyan, E. B. Magnusson, A. Patterson, and P. J. Leek. Surface acoustic wave resonators in the quantum regime. *Phys. Rev. B*, 93:041411, 2016.

[87] E. B. Magnusson, B. H. Williams, R. Manenti, M.S. Nam, A. Nersisyan, M.J Peterer, A. Ardavan, and P. J. Leek. Surface acoustic wave devices on bulk ZnO at low temperature. *App. Phys. Lett.*, 106:063509, 2015.

[88] Yiwen Chu, Prashanta Kharel, William H. Renninger, Luke D. Burkhart, Luigi Frunzio, Peter T. Rakich, and Robert J. Schoelkopf. Quantum acoustics with superconducting qubits. *Science*, 358:199–202, 2017.

[89] S. Whiteley, G. Wolfowicz, C. Anderson, A. Bourassa, H. Ma, M. Ye, G. Koolstra, K. Satzinger, M. Holt, F. J. Heremans, A. Cleland, D. Schuster, G. Galli, and D. Awschalom. Spin-phonon interactions in silicon carbide addressed by gaussian acoustics. *Nat. Phys.*, 15:490 – 495, 2019.

[90] J. Bochmann, A. Vainsencher, D. Awschalom, and A. Cleland. Nanomechanical coupling between microwave and optical photons. *Nat. Phys.*, 9:712–716, 09 2013.

[91] K.C. Balram, M. Davanco, J. Song, and K. Srinivasan. Coherent coupling between radio frequency, optical, and acoustic waves in piezo-optomechanical circuits. *Nature Photonics*, 10:346–352, 2016.

[92] V. S. Shumeiko. Quantum acousto-optic transducer for superconducting qubits. *Phys. Rev. A*, 93:023838, 2016.

[93] I. Buluta, S. Ashhab, and F. Nori. Natural and artificial atoms for quantum computation. *Rep. Prog. Phys.*, 74:104401, 2011.

[94] Y. Colombe, T. Steinmetz, G. Dubois, F. Linke, D. Hunger, and J. Reichel. Strong atom-field coupling for bose-einstein condensates in an optical cavity on a chip. *Nature*, 450:272, 2007.

[95] M. J. A. Schuetz, E. M. Kessler, G. Giedke, L. M. K. Vandersypen, M. D. Lukin, and J. I. Cirac. Universal quantum transducers based on surface acoustic waves. *Phys. Rev. X*, 5:031031, Sep 2015.

[96] A. Frisk Kockum, P. Delsing, and G. Johansson. Designing frequency-dependent relaxation rates and lamb shifts for a giant artificial atom. *Phys. Rev. A*, 90:013837, 2014.

[97] L. Guo, A. Grimsmo, A. Frisk Kockum, M. Pletyukhov, and G. Johansson. Giant acoustic atom: A single quantum system with a deterministic time delay. *Phys. Rev. A*, 95:053821, 2017.

[98] A. Frisk Kockum, G. Johansson, and F. Nori. Decoherence-free interaction between giant atoms in waveguide quantum electrodynamics. *Phys. Rev. Lett.*, 120:140404, Apr 2018.

[99] G. Andersson, B. Suri, L. Guo, T. Aref, and P. Delsing. Non-exponential decay of a giant artificial atom. *Nat. Phys.*, 15:1123–1127, 2016.

[100] R. H. Hadfield. Single-photon detectors for optical quantum information applications. *Nat. Photon.*, 3:696, 2009.

[101] M. D. Eisaman, J. Fan, A. Migdall, and S. V. Polyakov. Invited review article: Single-photon sources and detectors. *Rev. Sci. Instrum.*, 82:071101, 2011.

[102] A. A. Houck, D. I. Schuster, J. M. Gambetta, J. A. Schreier, B. R. Johnson, J. M. Chow, L. Frunzio, J. Majer, M. H. Devoret, S. M. Girvin, and R. J. Schoelkopf. Generating single microwave photons in a circuit. *Nature*, 449:328, 2007.

[103] O. Astafiev, A. M. Zagoskin, A. A. Abdumalikov, Yu. A. Pashkin, T. Yamamoto, K. Inomata, Y. Nakamura, and J. S. Tsai. Resonance fluorescence of a single artificial atom. *Science*, 327:840, 2010.

[104] D. Bozyigit, C. Lang, L. Steffen, J. M. Fink, C. Eichler, M. Baur, R. Bianchetti, P. J. Leek, S. Filipp, M. P. da Silva, A. Blais, and A. Wallraff. Antibunching of microwave-frequency photons observed in correlation measurements using linear detectors. *Nature Phys.*, 7:154, 2011.

[105] C. Lang, D. Bozyigit, C. Eichler, L. Steffen, J. M. Fink, A. A. Abdumalikov, M. Baur, S. Filipp, M. P. da Silva, A. Blais, and A. Wallraff. Observation of resonant photon blockade at microwave frequencies using correlation function measurements. *Phys. Rev. Lett.*, 106:243601, 2011.

[106] I.-C. Hoi, T. Palomaki, J. Lindkvist, G. Johansson, P. Delsing, and C. M. Wilson. Generation of nonclassical microwave states using an artificial atom in 1d open space. *Phys. Rev. Lett.*, 108:263601, 2012.

[107] W. R. Smith, H. M. Gerard, J. H. Collins, T. M. Reeder, and H. J. Shaw. Design of surface wave delay lines with interdigital transducers. *IEEE Trans. Microwave Theory Tech.*, MTT-17:856, 1969.

[108] C. Campbell. *Surface Acoustic Wave Devices and their Signal Processing Applications*. Academic Press, San Diego, 1989.

[109] A. J. Slobodnik Jr., P. H. Carr1, and A. J. Budreau. Microwave frequency acoustic surface-wave loss mechanisms on $LiNbO_3$. *J. of Appl. Phys.*, 41:4380, 1970.

[110] A. J. Slobodnik Jr. *Materials and their influence on performance*, pages 225–303. Springer Berlin Heidelberg, Berlin, Heidelberg, 1978.

[111] J. H. Collins, H. M. Gerard, T. M. Reeder, and H. J. Shaw. Unidirectional surface wave transducer. *Proc. IEEE*, 57:833, 1969.

[112] K. Yamanouchi, C. H. S. Lee, K. Yamamoto, T. Meguro, and H. Odagawa. GHz-range low-loss wide band filters using new floating electrode type unidirectional transducers. *IEEE Ultrasonics Symp.*, 1:139, 1992.

[113] K. Yamanouchi, T. Meguro, Y. Wagatsuma, H. Odagawa, and K. Yamamoto. Nanometer electrode fabrication technology using anodic oxidation resist and application to unidirectional surface acoustic wave transducers. *J. of Appl. Phys.*, 33:3018, 1994.

[114] K. Yamanouchi. Generation, propagation and attenuation of 10 GHz-range SAW in $LiNBO_3$. *IEEE Ultrasonics Symp.*, 1:57, 1998.

[115] È. Dumur, K. J. Satzinger, G. A. Peairs, Ming-Han Chou, A. Bienfait, H.-S. Chang, C. R. Conner, J. Grebel, R. G. Povey, Y. P. Zhong, and A. N. Cleland. Unidirectional distributed acoustic reflection transducers for quantum applications. *Appl. Phys. Lett.*, 114:223501, 2019.

[116] A. Ask, M. Ekström, P. Delsing, and G. Johansson. Cavity-free vacuum-Rabi splitting in circuit quantum acoustodynamics. *Phys. Rev. A*, 99:013840, Jan 2019.

[117] M. Tinkham. *Introduction to Superconductivity.* Dover Publications, New York, second edition, 2004.

[118] Leon N. Cooper. Bound electron pairs in a degenerate fermi gas. *Phys. Rev.*, 104:1189–1190, 1956.

[119] J.J. Sakurai. *Modern Quantum Mechanics (Revised Edition).* Addison-Wesley, Reading, Massachusetts, 1993.

[120] P. Krantz, M. Kjaergaard, F. Yan, T. P. Orlando, S. Gustavsson, and W. D. Oliver. A quantum engineer's guide to superconducting qubits. *Appl. Phys. Rev.*, 6(2):021318, 2019.

[121] B.D. Josephson. Possible new effects in superconductive tunnelling. *Phys. Lett.*, 1:251–253, 1962.

[122] H. Zheng, D. J. Gauthier, and H. U. Baranger. Waveguide QED: Many-body bound-state effects in coherent and fock-state scattering from a two-level system. *Phys. Rev. A*, 82:063816, 2010.

[123] H. Zheng, D. J. Gauthier, and H. U. Baranger. Waveguide-QED-based photonic quantum computation. *Phys. Rev. Lett.*, 111:090502, 2013.

[124] D. Valente, Y. Li, J. P. Poizat, J. M. Gérard, L. C. Kwek, M. F. Santos, and A. Auffèves. Optimal irreversible stimulated emission. *New J. Phys.*, 14:083029, 2012.

[125] I.-C. Hoi, C. M. Wilson, G. Johansson, J. Lindkvist, B. Peropadre, T. Palomaki, and P. Delsing. Microwave quantum optics with an artificial atom in one-dimensional open space. *New J. Phys.*, 15:025011, 2013.

[126] Y. Makhlin, G. Scöhn, and A. Shnirman. Josephson-junction qubits with controlled couplings. *Nature*, 398:305–307, 1999.

[127] M. Büttiker. Zero-current persistent potential drop across small-capacitance Josephson junctions. *Phys. Rev. B*, 36:3548–3555, 1987.

[128] A. Houck, J. Koch, M. Devoret, S. Girvin, and R. Schoelkopf. Life after charge noise: Recent results with transmon qubits. *Quantum Inf. Process.*, 8:105–115, 2009.

[129] G Wendin. Quantum information processing with superconducting circuits: a review. *Rep. Prog. Phys.*, 80:106001, 2017.

[130] B Peropadre, J Lindkvist, I-C Hoi, C M Wilson, J J Garcia-Ripoll, P Delsing, and G Johansson. Scattering of coherent states on a single artificial atom. *New J. Phys.*, 15(3):035009, 2013.

[131] E. Wiegand, B. Rousseaux, and G. Johansson. Semiclassical analysis of dark-state transient dynamics in waveguide circuit QED. *Phys. Rev. A*, 101:033801, 2020.

[132] David M Pozar. *Microwave engineering; 3rd ed.* Wiley, Hoboken, NJ, 2005.

[133] C. W. Gardiner and P. Zoller. *Quantum Noise.* Springer, second edition, 2000.

[134] J. Lindkvist. *Quantum optics and relativistic motion with superconducting circuits.* PhD thesis, Chalmers University of Technology, 2015.

[135] I.-C. Hoi, A. Frisk Kockum, L. Tornberg, A. Pourkabirian, G. Johansson, P. Delsing, and C. Wilson. Probing the quantum vacuum with an artificial atom in front of a mirror. *Nat. Phys.*, 11:1045–1049, 2015.

[136] P.M. Anisimov, J.P. Dowling, and B.C. Sanders. Objectively discerning Autler-Townes splitting from electromagnetically induced transparency. *Phys. Rev. Lett.*, 107:163604, Oct 2011.

[137] A. A. Abdumalikov, O. Astafiev, A. M. Zagoskin, Yu. A. Pashkin, Y. Nakamura, and J. S. Tsai. *Phys. Rev. Lett.*, 104:193601, 2010.

[138] Io-Chun Hoi, C. M. Wilson, Göran Johansson, Tauno Palomaki, Borja Peropadre, and Per Delsing. *Phys. Rev. Lett.*, 107:073601, 2011.

[139] J. Gea-Banacloche, Y. Li, S. Jin, and M. Xiao. Electromagnetically induced transparency in ladder-type inhomogeneously broadened media: Theory and experiment. *Phys. Rev. A*, 51:576–584, 1995.

[140] B. Gouraud, D. Maxein, A. Nicolas, O. Morin, and J. Laurat. Demonstration of a memory for tightly guided light in an optical nanofiber. *Phys. Rev. Lett.*, 114:180503, 2015.

[141] S. Novikov, T. Sweeney, J.E. Robinson, S.P. Premaratne, B. Suri, F.C. Wellstood, and B.S. Palmer. Raman coherence in a circuit quantum electrodynamic lambda system. *Nat. Phys.*, 12:75–79, 2015.

[142] S. Weis, R. Rivière, S. Deléglise, E. Gavartin, O. Arcizet, A. Schliesser, and T.J. Kippenberg. Optomechanically induced transparency. *Science*, 330:1520–1523, 2010.

[143] A.H. Safavi-Naeini, T.P.M. Alegre, J. Chan, M. Eicheneld, M. Winger, Q. Lin, J. T. Hill, D. E. Chang, and O. Painter. Electromagnetically induced transparency and slow light with optomechanics. *Nature*, 472:69–73, 2011.

[144] M. K. Tey, Z. Chen, S. A. Aljunid, B. Chng, F. Huber, G. Maslennikov, and C. Kurtsiefer. *Nature Phys.*, 4:924–927, 2008.

[145] G. Wrigge, I. Gerhardt, J. Hwang, G. Zumofen, and V. Sandoghdar. *Nature Phys.*, 4:60–66, 2008.

[146] L. Rayleigh. On waves propagated along the plane surface of an elastic solid. *Proceedings of the London Mathematical Society*, pages 4–11, 1885.

[147] A. Frisk Kockum. *Quantum optics with artificial atoms*. PhD thesis, Chalmers University of Technology, 2014.

[148] T. W. Bristol, W. R. Jones, P. B. Snow, and W. R. Smith. Applications of double electrodes in acoustic surface wave device design. In *1972 Ultrasonics Symposium*, page 343. IEEE, 1972.

[149] I. Boström, J. Björck, and J. Runeson. Effektiv konvertering av ytakustiska vågor i en riktning. Bachelor's thesis, Chalmers University of Technology, Department of Microtechnology and Nanoscience, 2015.

[150] K. Yamanouchi and H. Furuyashiki. New low-loss SAW filter using internal floating electrode reflection types of single-phase unidirectional transducers. *Electron. Lett.*, 20:989, 1984.

[151] M. Takeuchi and K. Yamanouchi. Coupled mode analysis of SAW floating electrode unidirectional transducers. *IEEE Trans. UFFC*, 40:648, 1993.

[152] D. P. Morgan. Quasi-static analysis of floating-electrode unidirectional SAW transducers (feudts). *IEEE Ultrasonics Symp.*, 48:107, 1999.

[153] D. P. Morgan. Investigation of novel floating-electrode unidirectional SAW transducers. *IEEE Ultrasonics Symp.*, 1:15, 2000.

[154] D. P. Morgan. Quasi-static analysis of floating-electrode unidirectional SAW transducers. *IEEE Trans. UFFC*, page 15, 2001.

[155] M. Takeuchi and K. Yamanouchi. Field analysis of SAW single-phase unidirectional transducers using internal floating electrodes. *IEEE Ultrasonics Symp.*, 15:57, 1988.

[156] M. Ekström. *Towards measuring quantum sound*. Licentiate thesis, Chalmers University of Technology, 2016.

[157] G. J. Dolan. Offset masks for lift-off photoprocessing. *Appl. Phys. Lett.*, 31:337, 1977.

[158] M. Simoen. *Parametric interactions with signals and the vacuum*. PhD thesis, Chalmers University of Technology, Department of Microtechnology and Nanoscience, 2015.

[159] T. Szabo and A. J. Slobodnik Jr. The effect of diffraction on the design of acoustic wave devices. *IEEE Trans. Sonics Ultrason.*, SU-20:240–251, 1973.

[160] W. D. Hunt, R. L. Miller, and B. J. Hunsinger. Slowness surface measurements for zero- and five-degree 100-cut GaAs. *J. Appl. Phys.*, 60:3532, 1986.

[161] M. Fleischhauer, A. Imamoglu, and J.P. Marangos. Electromagnetically induced transparency: Optics in coherent media. *Rev. Mod. Phys.*, 77:633–673, 2005.

[162] M. V. Gustafsson, P.V. Santos, G. Johansson, and P. Delsing. Local probing of propagating acoustic waves in a gigahertz echo chamber. *Nature Phys.*, 8:338, 2012.

[163] M.V. Gustafsson. *Studies of acoustic waves, noise and charge pumping using single-electron devices*. PhD thesis, Chalmers University of Technology, 2012.

[164] H. Robert Hadfield and Göran Johansson, editors. *Superconducting Devices in Quantum Optics*. Springer International Publishing, Cham, 2016.

[165] A. Bienfait, K. J. Satzinger, Y. P. Zhong, H.-S. Chang, M.-H. Chou, C. R. Conner, É. Dumur, J. Grebel, G. A. Peairs, R. G. Povey, and A. N. Cleland. Phonon-mediated quantum state transfer and remote qubit entanglement. *Science*, 364(6438):368–371, 2019.

[166] T. Niemczyk, F. Deppe, H. Huebl, E. Menzel, F. Hocke, M. Schwarz, J. García-Ripoll, D. Zueco, T. Hummer, E. Solano, A. Marx, and R. Gross. Circuit quantum electrodynamics in the ultrastrong-coupling regime. *Nat. Phys.*, 6:772–776, 2010.

[167] P. Krantz. *The Josephson parametric oscillator - From microscopic studies to single-shot qubit readout*. PhD thesis, Chalmers University of Technology, 2016.